

ABSTRACT

LIU, YING. Shape Programming of Polymeric Materials from 2D to 3D. (Under the direction of Dr. Michael D. Dickey and Dr. Jan Genzer).

This Ph.D. dissertation focuses on converting planar two-dimensional (2D) shape programmable polymeric materials into three-dimensional (3D) shapes. The desire to create 3D shapes is based on the general premise that shape defines function in many materials. Working with 2D planar forms is appealing because they are compatible with many planar processes developed for semiconductor processing as well as other patterning techniques including screen printing, roll-to-roll processing, and inkjet printing. Specifically, my work is centered on developing assembly methods leading to generating 3D structures by employing out-of-plane sheet folding and on formation of buckled surface topographies from 2D forms.

We report on a simple approach to realize self-folding of homogeneous pre-strained polymer sheets by employing conventional 2D printing methods. Our approach uses desktop printer to pattern the polymer sheets with ink locally absorbs heat from a uniform light source and act as hinges that convert the 2D sheets into various 3D structures by choosing an appropriate inked pattern, line width, and support temperature. Compared with common design methods for self-folding, which require multistep complex fabrications or pre-programming, our approach is distinguished by its simplicity and use of inexpensive polymer sheets. Experimentally, we study the effect of the hinge width and color on sheet folding. The speed of folding as well as larger folding angles can be achieved by increasing the width of hinges and increasing the support temperature. Computer modeling describes quantitatively the trends observed in experiments.

We study macroscopic thermal shrinkage of the pre-strained polymer sheets as a function of temperature, time, and heating rate to provide information about the temperature required for folding to occur and to comprehend the kinetic of shrinkage of the polymer sheets during folding. A simple geometrical model that incorporates these macroscopic measurements predicts successfully the maximum bending angle as well as the dynamic bending angle for different hinge widths.

We demonstrate self-folding in planar polymer sheets using focused laser light. The laser power, intensity and beam width have been shown to control the folding time and the bending angle. The utilization of laser light is appealing because the approach requires no patterning of pre-defined hinges.

We also document the benefits of using light-emitting diodes (LEDs) as light sources for folding of polymer sheets. Selective wavelengths of the LED sources in conjunction with the color and width of the hinge regions enable us to fine-tune folding pathways within the sheets. We demonstrate that sequential folding (or rolling) can be realized by combining hinges with different degrees of light absorption (adjusted by varying the greyscales or color of hinges). The ability to program self-folding pathways can be potentially utilized in manufacturing grippers and actuators, and can be employed in folding of complex origami structures.

Finally, we study the formation of isotropic buckles on substrates comprising thin films of metal/oxide deposited on top of polymer layers resting on silicone substrates. We explore different approaches towards enhancing the buckle aspect ratio (i.e., amplitude/wavelength ratio) that would lead to enhancement of light harvesting. A new aspect of this work includes the utilization of electric fields to amplify the aspect ratio during

thermal buckle formation. We show that using this method it is possible to generate surfaces that contain at least two different generations of buckles/wrinkles on surfaces with different length scales and aspect ratios.

© Copyright 2013 Ying Liu

All Rights Reserved

Shape Programming of Polymeric Materials from 2D to 3D

by
Ying Liu

A dissertation submitted to the Graduate Faculty of
North Carolina State University
in partial fulfillment of the
requirements for the degree of
Doctor of Philosophy

Chemical Engineering

Raleigh, North Carolina

2013

APPROVED BY:

Jan Genzer
Committee Chair

Michael D. Dickey
Co-Chair

Gregory Parsons

Jon-Paul Maria

Veena Misra

DEDICATION

This dissertation is dedicated to my dearest parents and grandparents for their lifelong encouragement, support, sacrifices and love.

谨以此博士文献给我最亲爱的父母和祖父母，
感谢他们一路走来对我的鼓励，支持，奉献和无私的爱。

BIOGRAPHY

Ying Liu was born in Zhenjiang city, Jiangsu Province, China. After graduating from high school, she moved to Hangzhou city, Zhejiang Province, China to pursue her bachelor degree in Chemical Engineering at Zhejiang University (ZJU). In her junior year, she joined student exchange program in School of Engineering at Hong Kong University of Science and Technology (HKUST) for one-year study in Hong Kong. After completing the bachelor degree in Chemical Engineering in ZJU, she earned her master degree in Chemical Engineering at Iowa State University, Iowa, USA in the field of protein separation. She then moved to Raleigh in North Carolina to pursue her doctoral degree in the department of Chemical and Biomolecular Engineering at North Carolina State University (NCSU), under the guidance of both Prof. Michael D. Dickey and Prof. Jan Genzer. She focused on the study of shape programmable polymeric materials to convert 2D planar forms to 3D shapes.

ACKNOWLEDGMENTS

First, I acknowledge my advisors Prof. Michael D. Dickey and Prof. Jan Genzer. I cannot survive my Ph.D. life without their valuable advice, great discussions, time investment, and encouragement. They are such great mentors who always support and trust in me, always present strong passion and positive thoughts to motivate the research, especially when I have hard time for the project. I also learn to fulfill multitask with effective time management, good cooperation, and strong communication skills from them as professional examples.

Next, I would like to thank Dr. Gregory N. Parsons, Dr. Veena Misra and Dr. Jon-Paul Maria for serving as my Ph.D. committee members and offering me helpful advice and valuable cooperation for projects we worked together.

I am also thankful for everyone that I have worked with and learned from during my Ph.D. research. I deeply thank Brandi Shaw, Julie Boyles, Matthew Miskiewicz, Russell Mailen for their hard work and valuable cooperation for the collaborated research projects of “self-folding of 3D structures”. I appreciate the great discussion with Qingquan Qin, John Durham and Dr. Y. Zhu for the study of mechanical properties of polymers too. Moreover, I deeply thank Dr. Sharvil Desai, Dr. Michelle Casper, Kazi Sadman, Dr. Arif Ömer Gözen for their hard work and valuable contribution on the collaborated research project on the study of buckled surface topography. I also acknowledge Jay Lewis and Ethan Klem for the cooperation to build up organic photovoltaics, as well as Smita for her help and training on the fabrication of organic photovoltaics. I appreciate Dr. Efimenko to share expertise in the knowledge of buckling topography too.

I feel very lucky to have such nice and supportive group members: Rashed, Robin, Berc, Daniel, Mohammed, Collin, Duncan, Gilbert, Julie, Casey, Erich, Xiaojing, Preeti, Rohan, Matt, Phillip, Edwin, Sean, Eric, Moshe, Pandi, who help me in the lab work, train me for the use of the instruments, and provide great suggestion throughout my PhD research.

I would also like to thank Dr. Gregory N. Parsons, Dr. Jon-Paul Maria, Dr. Veena Misra, Dr. Saad Khan, Dr. Wesley Henderson, Dr. Orlin Velez and Dr. Michael Escuti for their generosity to allow me use instruments and software in their labs. I appreciate the help from the staff in the department of Chemical and Biomolecular Engineering too.

I am very grateful for my nice friends to have fun time together, give me passion and positive attitude what can help me overcome hard times. I really enjoyed the leisure and sports time with them.

Finally, I would like to express my deep gratitude to my beloved parents and other family members in China for always believing that I could achieve anything I believed and tried hard, and always showing me the positive attitude for life. The family reunion is always short for me when I had a trip back home in China from US, but all your love around is always endless power source to support me. There is a big thank for you.

Lastly, I acknowledge the funding from National Science Foundation and Department of Energy to support my research.

TABLE OF CONTENTS

LIST OF TABLES.....	ix
LIST OF FIGURES.....	xi
CHAPTER 1 Introduction to Shape Programmable Polymers.....	1
Overview	2
1.1 Why Shape Programming from 2D is Interesting	4
1.2 Strategies of Converting 2D Plane to 3D Structure.....	5
1.2.1 Active Materials for Shape Programming.....	5
1.2.2 Approach to Shape Programming: Self-folding.....	12
1.2.2.1 Designs of 2D Sheets for Self-folding	13
1.2.2.2 Different Stimuli Utilized for Self-folding	16
1.2.2.3 Management of Stress/Strain Gradient to Control Folding Process.....	18
1.3 Strategies of Converting 2D plane to 2D with Surface Topography.....	21
1.3.1 Surface Topography via Buckles Formation.....	22
1.3.1.1 Mechanism for Buckles Formation	24
1.3.1.2 Applications	30
1.3.2 Surface Topography via Shape Memory Effect.....	31
1.3.3 Surface Topography via Polymer Brushes	32
1.4 Summary and Dissertation Outline.....	33
References.....	36
CHAPTER 2 Self-folding of Polymer Sheets Using Local Light Absorption*.....	50
2.1 Introduction.....	51
2.2 Experimental	54
2.3 Results and Discussion.....	55
2.4 Conclusion	65
2.5 Acknowledgements	66
References	67
Supporting Information	71

CHAPTER 3 Modeling Self-Folding Kinetics Using Thermal Shrinkage of Pre-strained Polymer Sheets*	74
3.1 Introduction	75
3.2 Experimental	76
3.3 Results and Discussion	77
3.4 Conclusion	90
3.5 Acknowledgements	92
References	93
Supporting Information	95
CHAPTER 4 3D Folding of Pre-Strained Polymer Sheets via Laser Light	100
4.1 Introduction	101
4.2 Experimental	102
4.3 Results and Discussion	102
4.4 Conclusion	111
4.5 Acknowledgements	111
References	112
Supporting Information	114
CHAPTER 5 Sequential Folding of Polymer Sheets via Color Selection	115
5.1 Introduction	116
5.2 Experimental	117
5.3 Results and Discussion	118
Sequential Folding via Applying Black Ink and Utilizing IR Heat Lamp	118
Sequential Folding via Applying Color Inks and Utilizing LED Lights	123
5.4 Applications of Sequential Folding	131
5.5 Conclusion	132
5.6 Acknowledgements	133
References	134
Supporting Information	135

CHAPTER 6 Formation of Isotropic Buckles on Polystyrene and Enhancement of its Aspect Ratio.....	138
6.1 Buckles based on Polystyrene Laminates	139
6.2 Experimental	140
6.3 Results and Discussion.....	140
6.4 Effort to Enhance Limited Aspect Ratio of Isotropic Buckles	148
6.5 Buckles with Enhanced Aspect Ratio via Electric-field Amplification.....	152
6.5.1 Hypothesis of Electric-field Amplification.....	152
6.5.2 Experimental	154
6.5.3 Results and Discussion.....	156
6.6 Summary.....	159
6.7 Acknowledgements	160
References	161
Supporting Information	164
CHAPTER 7 Summary and Future Outlook.....	166
7.1 Summary.....	167
7.2 Future Outlook.....	170
Appendices.....	174
Appendix A	175
Appendix B	197

LIST OF TABLES

Chapter 1

- Table 1.1** Representative research work on self-folding regarding different stimuli applied.....17
- Table 1.2** The aspect ratio of buckles resulting from different UVO doses. The applied axial strain is 50% for all samples, and the thickness of PDMS is ≈ 1 mm. The power density of UVO is 7.6 mW/cm^226

Chapter 2

- Table S2.1** Folding angles as a function of line width patterned across the narrow dimension of a Shrinky-Dink ($L = 25$ mm, $L' = 10$ mm).....71
- Table S2.2** Folding angles for double-line hinges as a function of line spacing on Shrinky-Dinks (25 mm x 10 mm). Two lines (each with a width of 1 mm) were patterned parallel to each other across the center of the sheet with a space placed between the lines.....71

Chapter 3

- Table S3.1** Parameters of the exponential fitted curves using Equation (3.2): $S = S_{\infty}[1 - e^{-k_t(\tau - \tau_0)}]$, in different isothermal conditions for the isothermal shrinkage of pre-strained sheets.....96
- Table S3.2** Parameters of the exponential fitted curves using Equation (3.4): $S = S_{\infty}[1 - e^{-K(T - T_0)}]$, at different heating rates for the non-isothermal shrinkage of pre-strained PS sheets.....97

Chapter 5

- Table 5.1** Key process parameters important for sequential folding.....127
- Table 5.2** Examples of color selection for sequential folding. 1st hinge represents the hinge which folds first in that case, while 2nd hinge represents the hinge which folds following 1st hinge. Yes or No represents folding or no folding separately.....130
- Table S5.1** Measured power density for different LED lights used for the folding test.....135

Chapter 6

Table S6.1 Spin conditions used to spin-coat PS films in our experiment.....**164**

Appendix A

Table A1 Transmission, sheet resistance and roughness of as-sputtered and commercial ITO.....**180**

Table A2 Short-circuit current densities (J_{sc}), fill factors (FF), open circuit voltages (V_{oc}) and efficiencies of OPV based on P3HT:PCBM blends with and without post-annealing and with different active areas.....**184**

Table A3 Short-circuit current densities (J_{sc}), fill factors (FF), open circuit voltages (V_{oc}) and efficiencies of OPV based on solutions with different concentrations.....**186**

Table A4 Short-circuit current densities, open-circuit voltages, fill factors and efficiencies for devices with different device layouts.....**188**

LIST OF FIGURES

Chapter 1

- Figure 1.1** Cross-sectional illustration of strategies to generate 3D shapes by using shape programmable polymeric materials in two categories: 3D structures by out-of-plane bending or folding, and 2D in-plane form with surface topography.....**3**
- Figure 1.2** (a) A typical piezoelectric materials with the electrodes applied on the top and bottom faces. The dash lines sketch a deformed shape in response to the electric field²⁶; and (b) Schematic of piezoelectric PVDF films used as a pressure sensor due to the deflection.²¹**6**
- Figure 1.3** 3D coil induced by local bending due to ionoprinting of a copper wire on pNaAc gel. A consequent gel gripper is demonstrated to catch and release a small blue cube of PDMS (~1g) in ethanol and water respectively. The scale bar is 10 mm.³⁹**8**
- Figure 1.4** (a) SMA actuators can be folded by applying Joule-heating (red arrows show the heating direction). b) Demonstration of folding a “boat” from a 2D planar composite sheets patterned with SMA hinges which can cause the folding through Joule-heating.¹**9**
- Figure 1.5** Photographs of folded cubes from a pre-programmed 2D SMP sheet.⁵⁴**11**
- Figure 1.6** Schematics of the comparison between self-assembly and self-folding.....**12**
- Figure 1.7** Schematics of different designs on 2D planar template for self-folding in cross-sectional view. (a) heterogeneous “hinge” materials (red) embedded in the bulk materials ; (b) bilayer structure with one responsive layer (red); and (c) pre-programming of homogeneous materials.....**13**
- Figure 1.8.** Schematics of bending of bi-metal strip.¹⁰² E_1 and E_2 are elastic moduli; α_1 and α_2 are thermal expansion coefficients for two layers separately; h_1 and h_2 are film thicknesses; and h is total thickness. P_1 is tensile force for layer 1 and P_2 is compressive force for layer 2.....**18**
- Figure 1.9** a) Schematic of the formation of buckles on an elastic substrate; b) optical microscopy images (top view) of typical unidirectional buckles and c)

	optical microscopy image of isotropic buckles (oriented in random directions). ¹²⁰	23
Figure 1.10	a) Photograph of the custom-designed stretcher. The sample such as a PDMS sheet is sandwiched tightly by screws, the sample is stretched axially (labeled in red) by rotating the shaft (labeled in blue); b) AFM image of unidirectional buckles on stretched PDMS with air plasma treated surface and c) Map scan by profilometry of unidirectional buckles on stretched PDMS with UVO treatment.....	25
Figure 1.11	Hierarchically-buckled topography due to large strain applied to UV/Ozone-treated PDMS. a) Illustration of hierarchically-buckled topography; b) hierarchical profile collected by profilometry and c) wavelengths of multiple generations of buckles as a function of applied strains. ¹¹⁹	26
Figure 1.12	Optical microscopy images of buckles formation when releasing and re-applying strain on an ITO sputtered PDMS sheet. The image was first taken right after ITO sputtering ($\epsilon \approx 10\%$), more images were taken when slowly releasing the strain from 10% to 2%. The film was re-stretched after total release ($\epsilon \approx 0\%$) to $\epsilon \approx 10\%$ and overstretched to $\epsilon \approx 12\%$. The images were taken consecutively (scale bar: 20 μm for all images).....	28
Figure 1.13	(a) Schematic, optical microscopy image and 3D profilometer image of isotropic buckles formed due to spontaneous swelling of a gradient crosslinked UV-curable resin (2-phenoxyethyl acrylate, crosslinker is 1,6-hexanediol diacrylate, photoinitiator is Irgacure 184). ¹³⁰ (b) Optical microscopy images of ordered buckles on Polyacrylamide/NP-TiO ₂ -CTAB PVP hybrid gel before and after water vapor treatment. (CTAB: cetyltrimethylammonium bromide; NP-TiO ₂ : titania nanoparticles). ¹³¹ (c) Schematic of reversible surface buckles of UVO-treated PDMS to oxidize the surface due to the swelling in response to different solvents. ¹³²	30
Figure 1.14.	Surface topography due to shape memory effect in an acrylate-based SMP (cured from methyl methacrylate (MMA), poly(ethylene glycol dimethacrylate) (PEGDMA) as crosslinker and 2,2-dimethoxy-2-phenylacetodphenone (initiator)). Schematics (top) and images (bottom) for different stages: (a) permanent pattern molded by thermally embossing nanoimprint lithography at $\sim 180\text{ }^\circ\text{C}$; (b) 2D planar surface after programming with a flat mold; and (c) recovered surface topography after	

heating at ~ 120 °C. The pattern has a pitch of ~ 800 nm and a height of ~ 180 nm.¹⁴¹32

Chapter 2

Figure 2.1 Schematic of different approaches to self-folding via thermal actuation (a-c are in cross-sectional view). Previous approaches include folding induced by²⁵: a) pre-programming of shape memory polymers; b) responsive hinges (red) composed of materials that differ from the bulk (blue); c) expansion mismatch of multilayer film stacks; and d) Our approach uses a uniform sheet and an even stimulus that is localized by surface patterns: i) A plain Shrinky-Dink; ii) Unidirectional folding via absorption of light by black ink (width, w) patterned on one side of the Shrinky-Dink; and iii) Bidirectional folding due to ink on both sides of the transparent Shrinky-Dink. Due to effective light absorption by the ink, the polymer under the black ink heats up faster than the rest of the polymer. The thicknesses of polymer films and black ink are not drawn to scale.....54

Figure 2.2 Photographs of 3D structures created by self-folding of Shrinky-Dinks patterned with a desktop printer. a) Single line ($w = 1$ mm, $L' = 10$ mm) patterned on the top side of the Shrinky-Dink; b) two lines ($w = 1$ mm, 12 mm spacing, $L' = 10$ mm) patterned on either side of the Shrinky-Dink; c) three lines patterned on alternating sides of the Shrinky-Dink ($w = 1$ mm, 12 mm spacing, $L' = 10$ mm); d) rectangular box (20 mm x 10 mm x 10 mm, $w = 1.5$ mm); e) tetrahedral box ($w = 2.0$ mm); and f) tetrahedral box with adjacent double hinges ($w = 1.0$ mm, inter-hinge spacing 0.3 mm). Both tetrahedrons have a square bottom facet (10 mm x 10 mm) and equilateral triangles on the other facets.....57

Figure 2.3 a) Experimental time needed to initiate folding ($\tau_{\text{folding,exp}}$) as a function of different patterned line widths and support temperatures and b) Time difference between the experiment and simulation ($\tau_{\text{folding,exp}} - \tau_{\text{folding,simul}}$) needed to initiate folding as a function of different patterned line widths and support temperatures. Shrinky-Dinks (25 mm x 10 mm) feature a single line of ink patterned across the center of the sample. The initial support temperatures (T_s) range from 20 to 90 °C and the widths of the lines vary from 0.5 mm to 2.0 mm.....59

- Figure 2.4** Simulated cross-sectional temperature profiles on the top (solid lines) and bottom (dotted lines) sides across the length of Shrinky-Dinks with different line widths ($w = 0.5$ mm and $w = 2.0$ mm) at two different support temperatures ($T_S = 20$ °C and $T_S = 90$ °C). a) $w = 0.5$ mm, $T_S = 20$ °C; b) $w = 2.0$ mm, $T_S = 20$ °C; c) $w = 0.5$ mm, $T_S = 90$ °C; and d) $w = 2.0$ mm, $T_S = 90$ °C. Each profile depicts a snap-shot of the temperature near the patterned line when the top central surface first reaches 120 °C. Times listed in each panel indicate response times for onset of folding as determined from the COMSOL simulation.....**62**
- Figure 2.5** Depiction of a folding / unfolding scenario. A grain of rice (left) can be packaged into a self-folded box (center). Uniformly heating the box above the glass transition temperature causes it to unfold and shrink in plane (right).....**64**
- Figure 2.6.** Demonstration of some origami structures induced by self-folding utilizing our approach. The left column shows 2D flat template patterned with black inks as hinges, and the right column shows 3D shapes self-folded when exposing those templates to light. The hinge width is 1.5 mm in these images.....**64**
- Figure S2.1** Photographs of Shrinky-Dink substrates like those used in this study. (left) A pristine substrate shrinks significantly in plane via uniform heating in the oven at 120 °C. (right) The pristine substrate is slightly hazy prior to shrinking, but transmits light effectively.....**71**
- Figure S2.2** Thermal photograph (left) of a Shrinky-Dink ($L = 25$ mm, $L' = 10$ mm) during the folding process taken using an infrared camera and the corresponding temperature profile defined in the black box (right). It is apparent that the film is beginning to fold in this snap-shot. In this experiment, the substrate started with a support temperature of ≈ 80 °C prior to irradiation. The temperature is plotted as a function of distance along the axis perpendicular to the hinge. The temperature is largest in the middle of the line and reaches ≈ 120 °C when folding first initiates, yet quickly tapers off to the support temperature, which is important for rapid, selective heating of the hinge.....**72**
- Figure S2.3** Photograph of a deformed box that is representative of the deformation that occurs to the panels when a sample is over-exposed to the light.....**72**

- Figure S2.4** Colored maps of the modeled temperature profile in the cross-section of a Shrinky-Dink during the first 4.2 seconds of exposure at $T_S = 20\text{ }^\circ\text{C}$. The heat originates from the top surface, which is the location of the ink. The two vertical dashed lines represents the patterned line width ($w = 1.5\text{ mm}$).....73
- Figure S2.5** Photographs of (a) a 2D Shrinky-Dink (diameter 10 mm) patterned with black toner in the shape of a concentric circle ($w = 1\text{ mm}$, outer diameter 6 mm) and (b) the resulting 3D saddle structure that forms upon exposure to light.....73

Chapter 3

- Figure 3.1** Temperature dependence on the exposure time to a heat lamp for a plain pre-strained PS sheet (open symbols) and a pre-strained PS sheet printed with black ink (solid symbols). Photographs of representative black and plain PS sheets depict the geometry for selected data points. Curled samples are flattened for imaging. The PS sheets (initial dimension 20 mm x 20 mm) rest on a hotplate at $90\text{ }^\circ\text{C}$ during the exposure to IR light.....78
- Figure 3.2** Thermal shrinkage of pre-strained PS sheets (initial dimension 20 mm x 20 mm) as a function of heating time at a constant temperature. The symbols represent the experimental data and the lines are best fit curves using Equation (3.2). The inset magnifies the data from 0 to 50 s.....80
- Figure 3.3** (Left) Ultimate shrinkage (S_∞) of PS sheets as a function of temperature during isothermal heating. The line is the best fit to the experimental data using Equation (3.3). (Right) Dependences of the shrinkage constant (k_t) on temperature during isothermal heating. The values of k_t have been obtained by fitting the data in Figure 2 to Equation (3.2). The slopes give activation energy for thermal shrinkage of PS above and below the critical temperature required for self-folding.....82
- Figure 3.4** (Left) Thermal shrinkage of pre-strained PS sheets (initial dimension 20 mm x 20 mm) as a function of temperature during constant heating rate. A wide range of heating rates is realized by using a hot stage (squares), halogen lamp (circles), and IR lamp (triangles), respectively. The numbers in parentheses denote different heating rates ($^\circ\text{C}/\text{min}$). The lines are best fits to Equation (3.4). (Right) Dependence of T_0 derived from the equation on the heating rates. The line is a guide to the eye.....85

- Figure 3.5** (Left) Side-view schematic of the polymer sheet (blue) and ink (black) depicting the simple geometrical model used to calculate the bending angle. (Right) Bending angles (α_B) as a function of hinge width obtained from experiment (circles) and calculated using the geometric model (squares). Experimental data were collected from pre-strained PS sheets as depicted in top-view schematic (initial dimension 25 mm x 10 mm) with a single line of ink patterned across the center of the sample resting on hotplate at 90 °C and exposed to external IR light at a distance of 5 cm.....**88**
- Figure 3.6** (Left column) Temperature of the inked hinge, T_h (solid squares) measured by IR camera. (Middle column) Thermal shrinkages of the PS sheets on the top surface (solid circles) derived from the temperature temporal profile. (Right column) Experimental bending angle change with time (solid triangles) compared with bending angle calculated based on the thermal shrinkage derived from the temperature temporal profile (open triangles). The different rows correspond to data with different hinge widths, W , equal to (from top to the bottom): 1.0, 1.2, 1.5, and 2.0 mm.....**90**
- Figure S3.1** (Left) Representative in-plane shrinkage of the pre-strained PS sheets in both X and Y directions with time at a constant temperature of 110, 120 and 160 °C. The experiment is operated in a hot stage at constant temperatures. (Right) Representative in-plane shrinkage of the pre-strained PS sheets in both X and Y directions with time at a constant heating under the exposure to IR light (479 °C/min and 142 °C/min) and in the hot stage (20 °C/min). All samples (initial dimension 20 mm x 20 mm) rest on a hotplate at 100 °C or with the initial temperature at 100 °C in the hot stage.....**95**
- Figure S3.2** Thermal shrinkage of the pre-strained PS sheets (initial dimension 20 mm x 20 mm) as a function of temperature during constant heating rate. Experimental shrinkage data are realized by using hot stage (blue), halogen lamp (green), and IR lamp (red), respectively. The numbers in the parentheses denote different heating rates (in °C/min). The lines are best fits to Equation (3.4): $S = S_\infty [1 - e^{-K(T-T_0)}]$**98**
- Figure S3.3** Temperature of ink patterned pre-strained PS sheets as a function of time. Experimental data are realized by using halogen lamp (green) and IR lamp (red). The numbers in the parentheses denote different heating rates (in °C/min), which are realized by varying the distance between the lamp to the

sample. All samples (initial dimension 10 mm x 10 mm) rest on a hotplate at 90 °C during the light exposure.....**98**

Figure S3.4 Bending angles (α_B) as a function of hinge width obtained from experiment (circles) and calculated using the geometrical model (squares). Experiment data were collected from pre-strained PS sheets (initial dimension 10 mm x 25 mm) with a single line of ink patterned across the center of the sample resting on hotplate at 90 °C and exposed to external IR light at various distances (5, 10, and 15 cm).....**99**

Figure S3.5 Thermal shrinkage of black ink patterned pre-strained PS sheets (initial dimension 20 mm x 20 mm) as a function of temperature under the IR lamp exposure at the distance of 5 cm from the sample. The line represents the best fit to Equation (3.4): $S = S_\infty [1 - e^{-K(T-T_0)}]$. $S_\infty \approx 55\%$ is assumed. The samples are rested on the hotplate at 90 °C.....**99**

Chapter 4

Figure 4.1 Photographs of the folding of a pre-strained polymer sheet coated with black ink triggered by IR laser light. The sample is 10 mm x 50 mm and is irradiated with a laser beam that spans the width of the sample and irradiates from the left side of the images. The beam, though not visible to the naked eye, can be clearly seen in the captured images impinging on the sample at times 1 and 2 s. The sample is held in place at the bottom by a clamp supported by a laser table.....**103**

Figure 4.2 Bending angle and onset time of folding as a function of laser incident power or incident intensity when the folding is triggered by IR laser light in a static linear manner. The samples are black ink coated pre-strained polymer sheets (4 mm x 40 mm).....**106**

Figure 4.3 (a) Temperature profiles in 3D from the simulation of COMSOL multiphysics; (b) Cross-sectional schematics of heat loss on the edge of the hinge. W_1 and W_2 are the beam widths, and d is the dimension of the edge for heat loss (outlined by dashed line and noted by yellow arrows); and (c) Onset energy as a function of onset time of folding for various beam widths (legend) and incident intensity (color scheme).....**109**

Figure 4.4 Fitting parameters for the inflection point, I_0 obtained from the bending angle vs. intensity using Equation (4.2).....**110**

Figure S4.1 UV-Vis Spectra of plain pre-strained polymer sheets and black ink printed pre-strained polymer sheets.....**114**

Figure S4.2 The relationship between onset time and total time of folding. (Legend: laser beam width in the unit of microns).....**114**

Chapter 5

Figure 5.1 (Top) Representative photographs of the folding process with different hinge widths (2.0, 1.5 and 1.0 mm from top to bottom) when the samples are rest on the hotplate of 90 °C and under the exposure of IR heat lamp at a distance of 5 cm (power density ~1 W/cm²). The samples (25 mm x 10 mm) feature a single black line hinge across the center of the sample. A printed protractor image is set as the background (Bottom) Bending angles change with different hinge widths (2.0, 1.5 and 1.0 mm) as a function of time.....**119**

Figure 5.2 (a) Optical microscope images of plain polymer sheet and polymer sheet patterned with various greyscale levels, i.e., percentagles of black ink (20%, 40%, 60%, 80%, and 100%) in grayscale. (b) Absorption spectra for the plain pre-strained polymer sheet and the black ink printed sheet with different greyscales ranging from 200 nm to 1100 nm. (c) Relationship of average optical absorption ranging from 400 to 800 nm with the percentage of black ink for the plain polymer sheet and the sheets printed with different greyscales. The dash line (y=x) is a guide to the eye.....**120**

Figure 5.3 (Top) The onset of folding and (Bottom) the bending angle as a function of absorption for the ink hinges with different greyscales (20~100%) and different hinge widths (W = 1 mm and 2 mm). The samples (25 mm x 10 mm) feature a single black line hinge across the center of the sample. The samples are rest on the hotplate of 90 °C and under the exposure of IR heat lamp at a distance of 5 cm.....**121**

Figure 5.4 Photographs for sequential rolling process of pre-strained polymer sheets patterned with descending greyscales by 10% black from 100% black to plain sheet. The sample is 22 mm x 5 mm. Time interval for processes (a)-(c) is one second, and time interval for process (d) is one second except last picture is at 9th second. The samples are rest on the hotplate of 90 °C and under the exposure of IR heat lamp at a distance of 5cm. The samples for processes (b)-(d) were pressed by a glass slide on the left side.....**122**

Figure 5.5	Absorption spectra of color inks printed on plain pre-strained polymer sheet and plain sheet. Dash lines represent the typical wavelengths for blue (470 nm), green (530 nm) and deep-red (660 nm) LEDs as shown in inset photos.....	124
Figure 5.6	(a) Photographs for “sequential folding” by utilizing the hinges in yellow (in response to blue LED) and cyan (in response to deep-red LED). 15W LEDs were used at a distance of 1.5 cm from the sample. (b) Change of bending angle with time for yellow and cyan hinges under the exposure of deep-red and blue LEDs separately.....	125
Figure 5.7	3D plots of onset time (a) and bending angle (b) for folding with optical absorption of inks and light intensity. Data points include the test using samples with different hinges widths (1.0, 1.5, and 2.0 mm) and different LEDs (red LED and blue LED). Onset time (c) and bending angle (d) for folding as a function of power for both red and blue LEDs. Samples (25 x 12 mm) feature a single line of ink patterned across the center of the sample.....	128
Figure 5.8	Color selection guideline for the sequential folding using color hinges. The hinge width is 2.0 mm, and 50 W red and blue LED lights are used set with moderate intensities as described above. The dash line denotes the minimum absorption (> 40%) desired to achieve a good folding.....	130
Figure 5.9	Strategy of sequential folding applied for (a) folding nested boxes with light control; and (b) realizing the unfolding pathway with color hinges patterned on both sides of the polymer sheet. All samples are rested on the hotplate at 90 °C for folding.....	132
Figure S5.1	Optical microscope images of different CMYK inks. From left to right are blue, cyan, green, 40% black, black (top row); and magenta, red, orange and yellow (bottom row). The scale bar is 500 μm.....	135
Figure S5.2	Photographs for “sequential folding” by utilizing the hinges in magenta color (in response to green LED) and cyan (in response to deep-red LED). 15W deep-red LED was used at a distance of 1.5 cm from the sample, and 15W green LED was used at a distance of 0.7 cm from the sample due to the low power density of green LED.....	136

Figure S5.3 Dependence of onset time (left) and bending angle (right) for folding on the key process parameters (i.e., ink absorption and light intensity) for different hinge widths of (a) 1.0 mm (b) 1.5 mm; and (c) 2.0 mm.....**137**

Chapter 6

Figure 6.1 AFM images of isotropic buckles based on ITO (40 nm)/PS (200 nm) bilayer resting on top a silicon substrate. 2D top view (a) and 3D tilt view (b). The wavelength is $\approx 1.76 \mu\text{m}$ and the aspect ratio is ≈ 0.06**141**

Figure 6.2 Investigation of buckle formation on ITO (thickness $\sim 100 \text{ nm}$) coated free-standing PS sheet under optical microscope under (a) 1000X and (b) 200X magnifications.....**142**

Figure 6.3 Optical microscope images of isotropic buckles based on ITO (40 nm)/PS films with different thicknesses of PS (a) 150 nm; (b) 370 nm; (c) 530 nm and (d) 650 nm on a silicon substrate. The ITO thin film was deposited by 20W RF sputtering with 4 mTorr Ar pressure. The sample was heated on the hotstage with the heating rate of $10 \text{ }^\circ\text{C}/\text{min}$ from room temperature to $120 \text{ }^\circ\text{C}$. The scale bar is $100 \mu\text{m}$**144**

Figure 6.4 Real-time investigation of isotropic buckles based on an ITO (50 nm)/PS ($1.5 \mu\text{m}$) bilayer on a silicon substrate. The buckles start to grow around $\sim 106 \text{ }^\circ\text{C}$, and then fully grow on the surface and remain stable the sample is cooled down. ITO thin film was deposited by 20W RF sputtering with 4 mTorr Ar pressure. The sample was heated on the hotstage with the heating rate of $10 \text{ }^\circ\text{C}/\text{min}$ from room temperature to $120 \text{ }^\circ\text{C}$. The scale bar is $100 \mu\text{m}$**145**

Figure 6.5 “Minimum annealing temperature” (T_{min}) measured for buckles as a function of PS thicknesses for different Al thicknesses (30, 40 and 50 nm).⁶.....**146**

Figure 6.6 The wavelength (λ), amplitude (A) and aspect ratio (AR) as a function of PS thicknesses. The ITO capping film thickness is 40 nm.¹⁴ The solid lines are meant to guide the eye.....**147**

Figure 6.7 Optical microscops images of thermal buckles of ITO (40 nm)/PS ($1.5 \mu\text{m}$) on the glass substrate: (a) as-sputtered buckles due to thermal expansion mismatch when sputtering at $160 \text{ }^\circ\text{C}$; and (b) two generations of buckles after annealing at $120 \text{ }^\circ\text{C}$ followed by sputtering.....**148**

- Figure 6.8** a) 3D microfluidic mixer made by Shrinky Dinks[®];⁹ b) cross-sections of the microfluidic channels before and after shrinkage⁹ and c) photograph of gold (top) and ITO (bottom) coated SD before and after annealing.....**150**
- Figure 6.9** SEM images of “crumbled” surfaces of gold (thickness ~40 nm) with an underlying chromium (thickness ~5 nm) layer (left column) and ITO (thickness ~40 nm) (right column) on SD before and after annealing at 120 °C for 30 min on a hotplate.....**151**
- Figure 6.10** Absorption spectra of plain SD (SDC), shrunken SD (snk-SDC), ITO coated SD (ITO/SDC), and shrunken ITO coated SD (snk-ITO/SDC). The ITO film is 40 nm thick, and shrinking occurs after annealing at 120 °C for 30 min on a hotplate.....**151**
- Figure 6.11** a) Schematic depicting 3D structures induced by electric field at polymer/air single layer;¹⁷ b) schematic of 3D structures induced by electric field at polymer/polymer/air trilayer¹⁸ and SEM images of c) cage-type and d) column structures made of poly(methyl methacrylate) (PMMA) while removing PS by cyclohexane with electric field on PS/PMMA/air trilyer with different electrode set-up.^{18,20}.....**153**
- Figure 6.12** Experimental procedure leading to: (a) oxidizing and cleaning silicon substrates; (b) spin-coating PS films and annealing; (c) typical PDMS mask used for sputtering; (d) Al sputtering on masked PS films; (e) as-sputtered Al/PS/Si samples; and (f) assembling samples with the e-field connections.....**155**
- Figure 6.13** Schematic of the experimental set-up: (a) original planar Al/PS thin films on silicon substrate with thermal oxide layer; (b) thermal buckles (λ_1) formed via heating the sample on the hot-stage without e-field; and (c) e-field buckles (λ_2) formed by applying e-field.....**157**
- Figure 6.14** Time evolution of buckles grown under a constant voltage (175 V) for a sample of Al (50 nm)/PS (5 μ m). The scale bar is 500 μ m.....**158**
- Figure 6.15** Optical microscopy images of buckle topographies from samples with different PS thicknesses by applying e-field (~35 V/ μ m): (a) 0.5 μ m thick PS film after 7 hours and (b) 5 μ m thick PS film after 1 minute. The inset images are initial thermal buckles. The Al film thickness is 50 nm. The scale bars are 500 μ m. Typical profilometry line scans for (c) thermal

buckles on 0.5 μm thick PS film and (b) e-field buckled on 5 μm thick PS film.....	159
Figure S6.1 Film thickness as a function of the concentration of polystyrene stock solution (wt%) in toluene and spin speed for coating process based on (a) results from literature; ²⁶ open circles represent 0.5 wt%; open square 1 wt%; open diamond 2 wt%; “X” represents 4 wt%; “+” represents 6 wt%; open triangle represents 8 wt%; solid circles represent 10 wt%; solid squares represent 15 wt%; solid diamond represent 20 wt% and solid triangles represent 30 wt%, and (b) our experimental results. ¹⁴	164
Figure S6.2 Real-time investigation of isotropic buckles based on ITO (40 nm)/PS (500 nm) bilayer on a silicon substrate. The buckles start to grow around temperature of 107 $^{\circ}\text{C}$, and then fully grow on the show surface and remain when the sample is cooled down. ITO thin film is deposited by 20W RF sputtering with 4 mTor process pressure. The sample is heated in the hot-stage with the heating rate of 10 $^{\circ}\text{C}/\text{min}$ from room temperature to 120 $^{\circ}\text{C}$. The scale bar is 100 μm	165

Appendix A

Figure A.1 Schematic of photocurrent generation in an OPV. ⁸ (a) photon absorption; (b) exciton diffusion; (c) separation of an exciton at heterojunction and (d) transport of charge carriers (electrons and holes).....	176
Figure A.2 Previous work on light trapping in OPVs based on a) microprism; ¹⁸ b) lambertian light scatterer; ²⁰ c) V-shaped/W-shaped configuration ²⁴ and d) surface relief gratings pattern. ²²	178
Figure A.3 Similar transmission spectra of as-sputtered ITO/glass compared with that of commercial ITO/glass in the range from 400 nm to 650 nm.....	181
Figure A.4 Amorphous as-sputtered ITO and crystalline commercial ITO from XRD profiles.....	181
Figure A.5 Photographs of reference device layouts on a) commercial ITO; b) homemade device on as-sputtered ITO with large active area and c) homemade device on as-sputtered ITO with small active area. The substrates are 1x1 inch ²	182

Figure A.6	Current density-voltage curves for the reference device and the homemade device. Reference device: $V_{oc}=0.42$ V; $J_{sc}=6.36$ mA/cm ² ; PCE=1.18%; FF=0.45. Homemade device: $V_{oc}=0.40$ V; $J_{sc}=4.80$ mA/cm ² ; PCE=0.65%; FF=0.34.....	183
Figure A.7	Current density-voltage curves for device without post-annealing (left) and with post-annealing (right).....	185
Figure A.8	Photographs of P3HT:PCBM films cast from different concentrations: a) 10:8 mg/ml P3HT:PCBM solution, spin speed is 600 rpm for 60 sec and b) 20:16 mg/ml P3HT:PCBM solution spin speed is 2000 rpm for 60 sec.....	186
Figure A.9	Photographs of different device layouts: a) crossed layout and b) central layout.....	187
Figure A.10	Schematic of the set up for I-V measurement through a mask.....	188
Figure A.11	(a) Profilometer scan images (3D and 2D) show the representative buckled surface of ITO/PS films; (b) Reflectances relative to Al reference for planar and buckled CuPc/C60 absorbing layer; and (c) Photograph of light scattering through buckled ITO/PS substrate from a red laser point. ⁴⁵	190
Figure A.12	Current density-voltage curves for planar and buckled devices. Planer device: $V_{oc}=0.46$ V; $J_{sc}=7$ μ A/cm ² ; PCE=1.89%; FF=0.569. Buckled device: $V_{oc}=0.46$ V; $J_{sc}=11$ μ A/cm ² ; PCE=2.2%; FF=0.425. (Credit: Ethan Klem and Jay Lewis).....	191

CHAPTER 1

Introduction to Shape Programmable Polymers

Overview

This review focuses on material strategies for shape programmable polymeric materials that can convert planar two-dimensional (2D) sheets into three-dimensional (3D) shapes. Working with 2D sheets is appealing because they are compatible with many planar processes developed for semiconductor processing as well as other patterning techniques, including, screen printing, roll-to-roll processing, and inkjet printing. The desire to create 3D shapes is based on the general premise that shape defines function in many materials, and the obvious fact that we live in a 3D world.

We categorize this review of shape programmable, stimuli-responsive 2D materials into two broad categories: 1) 2D substrates that use “hinges” or strain management to achieve out-of-plane folding, bending, or rolling; or 2) substrates that start out flat but form a characteristic topography on their surface in response to an external stimulus. **Figure 1.1** illustrates conceptually these two categories. The unifying thread in these two classes of structures is the importance of shape transformation in planar materials. The difference between these two categories is that the former one introduces the out-of-plane motion while the latter one remains macroscopically planar, although there can be in-plane motion (e.g., expansion or contraction). While in this review we focus on polymeric materials, we also mention other materials that might be utilized in conjunction with polymers. Shape transformation can occur due to asymmetrical distortion of the material due to expansion (e.g., thermal expansion, swelling), contraction (e.g., strain relaxation, deswelling), or flow (e.g., displacement of material due to a stress).

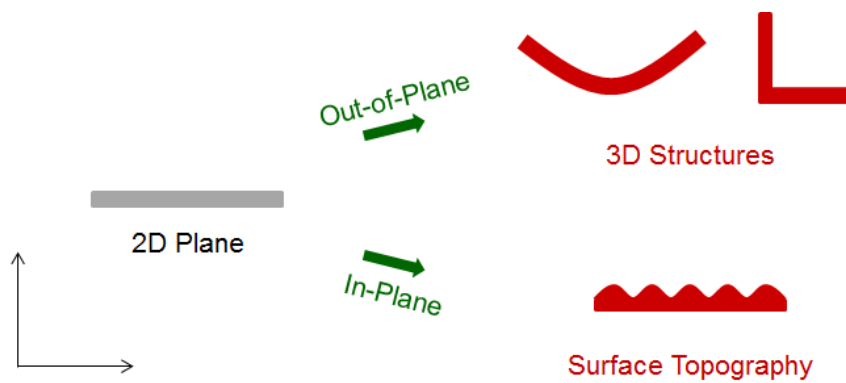


Figure 1.1. Cross-sectional illustration of strategies to generate 3D shapes by using shape programmable polymeric materials in two categories: 3D structures by out-of-plane bending or folding, and 2D in-plane form with surface topography.

There are many different strategies for materials and mechanisms that may be utilized to achieve these types of shape transformations. We briefly review the various strategies that are employed for these two material categories. In cases of mature fields, we point the reader to reviews that contain more detailed information. We also include a brief discussion of non-polymeric materials that may be utilized in conjunction with polymers to create actuating composites.

1.1 Why Shape Programming from 2D is Interesting

The use of 2D substrates has been preferred in manufacturing because of their compatibility with many high-throughput processes, such as conventional inexpensive 2D patterning techniques (i.e., lithography, screen printing, inkjet printing, and laser cutting) and more sophisticated nanofabrication (e.g., spin casting, photolithography, thin film deposition, etching, and other additive/subtractive processes developed for semiconductor processing).

Shape transformation from 2D to 3D structures has emerged in many applications, including such as reconfigurable devices,^{1,2} actuators and sensors,³⁻⁵ implantable devices,⁶⁻⁸ assembly, optics, meta materials, and deployable objects. For example, the manufacture of advanced morphing structures⁹ (e.g., aircraft wings) requires novel materials with high stiffness at high strains to enhance the performance over broad operation conditions. Other conceptual applications of next-generation mobile devices with morphing structures such as “Morphees” (shape-shifting mobile devices)¹³ and “MorePhone” (a cellphone curls upon a call)^{10,11} have been developed recently. In addition, novel optical or electrical functionalities can be generated if optical or electrical devices are fabricated in 3D geometries. For example, sensors constructed in 3D structures allow for the measurement of signals from three independent axes to obtain accurate angular and orientation parameters.³

Shape transformation from 2D plane to 3D surface topography has also been widely applied in smart adhesives¹², anti-fouling coatings^{13,14}, optical sensors,¹⁵ and haptic 3D touchscreen devices.¹⁶

1.2 Strategies of Converting 2D Plane to 3D Structure

There are many materials strategies and stimuli that can be utilized for shape programming polymers. Following the scheme in **Figure 1.1**, we first discuss the most prominent materials and mechanisms to convert 2D plane to 3D structures which have out-of-plane bending or folding.

1.2.1 Active Materials for Shape Programming

Piezoelectric materials: Piezoelectric materials possess an intrinsic electro-mechanical coupling behavior related to the presence of electric dipole moments in solids. This behavior is manifested by applying an electric field to change the shapes of these materials, or by deformation exerted through external mechanical forces that induces an electric field (**Figure 1.2a**).^{17,18} Both natural materials (e.g., natural crystals, dry bone, and tendon) and synthetic materials (e.g., piezoelectric ceramics^{17,19} such as lead zirconium titanate (PZT), and electroactive polymers such as polyvinylidene fluoride (PVDF)^{20,21}) have shown piezoelectric properties. Piezoelectric materials have been applied as sensors (e.g., **Figure 1.2b**) and actuators.²²⁻²⁴ For example, NASA recently launched “LaRC-MFC Actuator” for piezoelectric autonomous responsiveness [posted on YouTube].²⁵

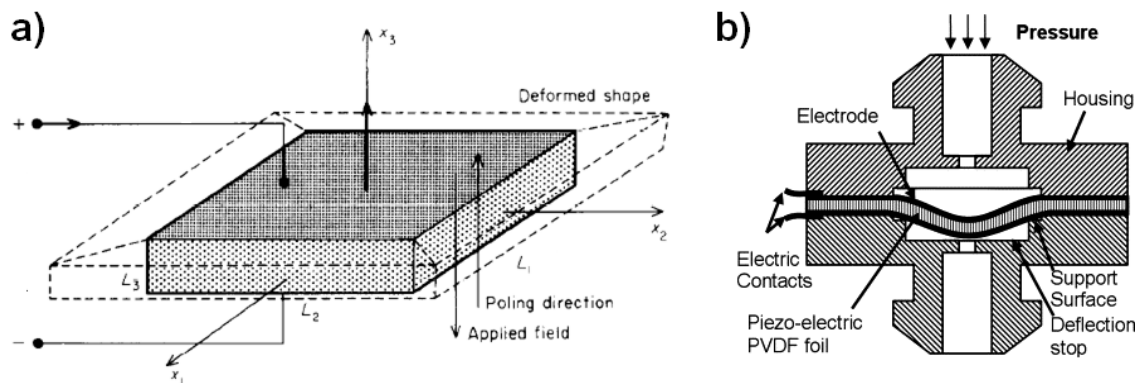


Figure 1.2. (a) A typical piezoelectric materials with the electrodes applied on the top and bottom faces. The dash lines sketch a deformed shape in response to the electric field²⁶; and (b) Schematic of piezoelectric PVDF films used as a pressure sensor due to the deflection.²¹

Polymer Brushes: Polymers grafted to substrates may exhibit conformational changes based on the application of external stimuli, such as, pH, temperature, salt concentration, or type of solvent, and have been reviewed before.^{27–29} This deformation can actuate bending motion.^{30–32} For example, a highly reversible cantilever actuator can be driven by coating it with polyelectrolyte brushes (e.g., polymethacryloyl ethylene phosphate (PMEP)).³⁰ In solutions with $\text{pH} < 2$, the brushes are protonated and insoluble in the solution; as a result a compressive stress is generated to cause the bending of the cantilever. When the solution pH exceeds 8, the brushes are deprotonated, which leads to compressive stresses due to an electrostatic repulsion between neighboring chains that causes bending of the cantilever.

Hydrogels: Hydrogels are water-soluble, soft polymeric networks containing high water content ($\gg 90\%$). For example, agarose gel contains $>99\%$ water and $\sim 1\%$ agarose

polymer, which is widely used in electrophoretic separation of proteins.³³ Hydrogels are noted for their ability to swell (and deswell) in response to environmental changes.³⁴ Hydrogels have been employed as biosensors and actuators, artificial muscles, drug delivery, bio-related media such as scaffolds or for cell encapsulations.³⁵⁻⁴¹ Recently, several interesting studies appeared that aimed at inducing the formation of 3D shapes from flat gel sheets in response to environmental changes such as ionic strength and solvents.^{38,39,41,42} For example, ionoprinting applies an oxidative bias to metal anode so ions are delivered on a polyelectrolyte hydrogel (e.g., sodium polyacrylate, pNaAc). The Cu^{2+} ions generate the crosslinks between neighboring polymers and induce local shrinkage by releasing water.³⁹ Out-of-plane bending can be induced due to the local shrinkage as shown in **Figure 1.3**. Another interesting example is that 3D shapes with nearly constant Gaussian curvature can be generated from 2D flat sheets by a simple halftone lithography of photo-crosslinkable poly(N-isopropylacrylamide) copolymers containing pendent benzophenone units for crosslinking.⁴¹

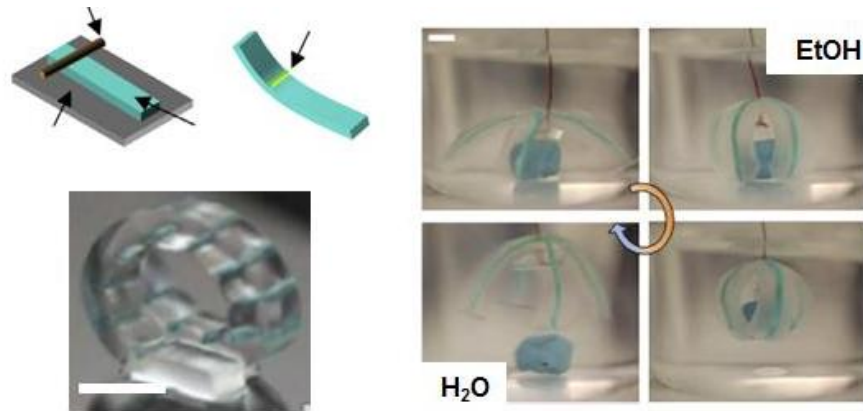


Figure 1.3. 3D coil induced by local bending due to ionoprinting of a copper wire on pNaAc gel. A consequent gel gripper is demonstrated to catch and release a small blue cube of PDMS (~1g) in ethanol and water respectively. The scale bar is 10 mm.³⁹

Shape memory materials (SMM): Shape memory effect describes a phenomenon wherein a material can return to its original shape from a temporary shape, defined by deforming the material and fixing it in a metastable state.⁴³ Swedish physicist Arne Olander discovered the shape-memory effect in the early 1930s in gold-cadmium (Au-Cd) alloys, which can be plastically deformed when cooling and can return to the original shape by heating.⁴⁴ Other researchers demonstrated the application for mechanical lifting using this alloy in 1950s.^{43,44} Materials demonstrating the shape-memory effect are called shape-memory materials (SMM). They include not only metal alloys but also other materials such as ceramics, liquid crystalline elastomers, polymers, and gels.^{19,45} Shape memory alloys (SMA) and shape memory polymers (SMP) are two of the most popular SMM.^{19,46,47}

Many different metal alloys (e.g., Nickel-Titanium alloys, copper-zinc-aluminum-nickel, copper-aluminum-nickel) have also shown reversible phase transitions, especially the

most common one Nickel-Titanium alloys (Nitinol)^{19,44,48} Those metal alloys demonstrate the shape-memory effect due to the intrinsic phase transition from a symmetrical austenitic phase at high temperatures to an asymmetrical martensitic phase at low temperatures.^{19,43,48} SMAs can be patterned as thin films on substrates to induce 3D structures due to the deflection of the substrates,⁴⁹ or patterning as actuating hinges that induce the folding of 2D planes when applying heat through joule-heating (**Figure 1.4**).^{1,50}

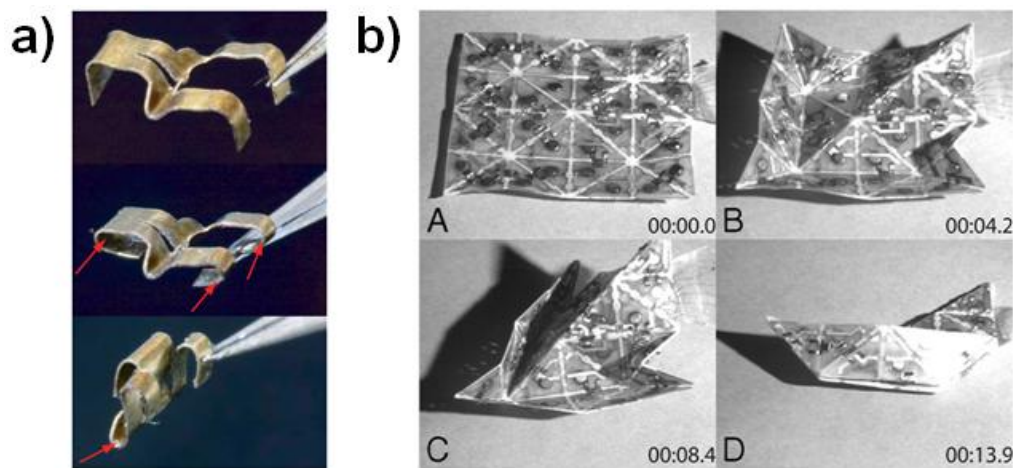


Figure 1.4. (a) SMA actuators can be folded by applying Joule-heating (red arrows show the heating direction). b) Demonstration of folding a “boat” from a 2D planar composite sheets patterned with SMA hinges which can cause the folding through Joule-heating.¹

SMPs were first synthesized in 1980s and enjoyed a rapid development and great attention due to their light weight, flexibility, high transformation strain, and low actuation forces compared to similar properties observed in metal alloys.⁴⁸ SMPs possess a great potential in a variety of applications such as automatic switches or sensors, intelligent

packaging and tissue engineering.^{12,19,43,48,51-53} The shape memory feature is governed by both the molecular architecture of polymers and the “programming process”. The ability to maintain the stable shape macroscopically for both the original and recovered structures relies on primary cross-linked net points in the form of either covalent bonds (i.e., chemical cross-linking) or strong intermolecular interactions (i.e., physically cross-linking).⁴⁸ Secondary cross-links, i.e., strong reversible interactions, are required to fix the temporary structure shapes. The secondary cross-linked domains (i.e., soft segments of SMPs) can be generated by utilizing interactions or steric hindrance due to side chains, or chain segments between two cross-linked points.⁴⁸

According to the properties of the cross-linking net points, SMPs can be divided into thermoplastic SMPs (i.e., physically cross-linked) and thermosetting SMPs (i.e., chemically cross-linked).⁴⁸ Thermoplastic SMPs (e.g., polyurethanes, polystyrene, polyethylene terephthalate, etc.) have been studied intensively and applied at a small scale (e.g., “biomaterials and textiles”). Polyurethane SMPs are advantageous compared to other thermoplastic SMPs due to their advantageous abilities of shape recovery, a wide recovery temperature range, better biocompatibility and processing ability.⁴⁸ Thermoplastic polymers are processed easily from solution or melt.⁵¹ Thermosetting SMPs (e.g., cross-linked polyethylene, thermosetting epoxy resins, shape memory polysiloxanes) are mostly used as structural materials in deployable structures and automobile applications due to their better thermal and mechanical properties relative to thermoplastic SMPs.⁴⁸

Macroscopic shape memory effect can be used for shape changing from 2D to 3D by pre-programming SMPs. For example, poly(ϵ -caprolactone) based SMPs stay at their temporary 2D planes at $T < T_{\text{trans}}$, and recover their original 3D shapes (i.e., closed cube) triggered by heating over T_{trans} (**Figure 1.5**).⁵⁴

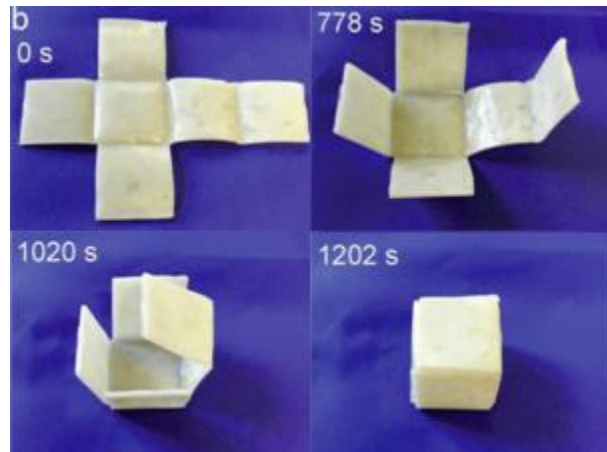


Figure 1.5. Photographs of folded cubes from a pre-programmed 2D SMP sheet.⁵⁴

A special class of light-responsive SMPs involves materials which bear photosensitive functional groups or molecules in the polymer networks. Triggered by appropriate UV wavelengths, the transferring effects in molecular level can have an impact on macroscopic volume change (shrinking or swelling) of polymers. The most studied photosensitive polymers can be categorized into three groups: azobenzenes, truphenylmethane leuco derivative, and photoreactive molecules.^{41,37}

1.2.2 Approach to Shape Programming: Self-folding

There are many approaches that may achieve shape changing from 2D to 3D out-of-plane as shown in **Figure 1.1**. Inspired by the autonomous folding found in nature (e.g., sensitive plants close the leaves in response to the gentle touch) and ancient Japanese art of origami folding,^{55,56} self-folding is one of these approaches to achieve the conversion from 2D to 3D shapes with out-of-plane bending. Self-folding is deterministic self-assembly approach that causes a 2D template with pre-defined hinges to fold into 3D shapes triggered by stimuli (**Figure 1.6**).⁵⁷ Hinges are regions on the substrate that activate (i.e., fold) in response to the external stimulus.^{57,58} With increasing need for reconfigurable devices, actuators, and sensors in numerous emerging applications, there is a great body of research in the field of self-folding utilizing different driving forces and different active materials.^{1,50,56–}

63

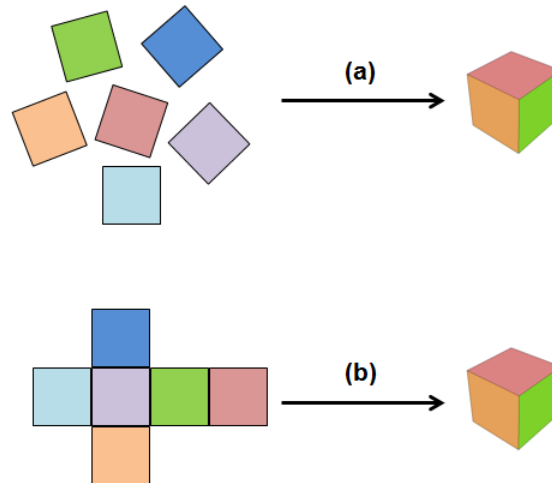


Figure 1.6. Schematics of the comparison between self-assembly and self-folding.

1.2.2.1 Designs of 2D Sheets for Self-folding

In general, three main designs have been developed for 2D sheets to achieve self-folding as illustrated in **Figure 1.7**:⁵⁹ 1) heterogeneous responsive materials patterned as “hinges” in the bulk materials; 2) bilayer structures and 3) macroscopically homogeneous materials, which are either homogeneous shape memory materials that are locally pre-programmed or materials with in-plane locally gradient properties (e.g., gradient of crosslinks).

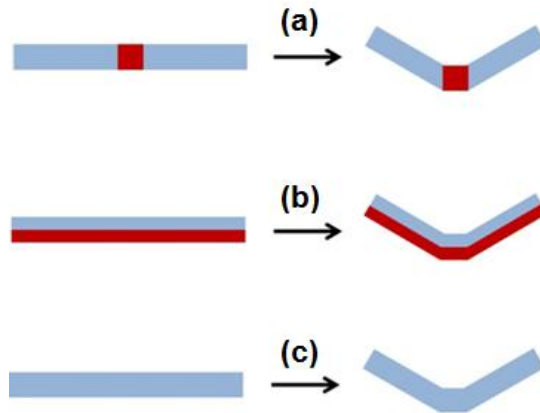


Figure 1.7. Schematics of different designs on 2D planar template for self-folding in cross-sectional view. (a) heterogeneous “hinge” materials (red) embedded in the bulk materials ; (b) bilayer structure with one responsive layer (red); and (c) pre-programming of homogeneous materials.

Case 1: Heterogeneous hinges

Figure 1.7a shows a strategy employed to fold 2D substrates in which the hinged region differs in composition from the rest of the sheet. These hinged regions may be composed of a variety of materials that shrink in response to an external stimulus. For

example, polyimide can shrink significantly when heated at high temperatures ($>200\text{ }^{\circ}\text{C}$ ⁶⁴ or $500\text{ }^{\circ}\text{C}$ ⁶⁵) due to out-gassing of strongly-bound solvents. Likewise, a pre-strained polymer film patterned as a hinge can shrink upon heating.⁶⁶ Shape memory metal alloys can usually be embedded as hinges to actuate with the application of resistive heating (**Figure 1.4**).⁶⁷ Moreover, a polymer (e.g., polycaprolactone, melting point $>60\text{ }^{\circ}\text{C}$ ⁶⁸) or melting metal (e.g., solder^{69,70}) can be patterned as a hinge and cause folding when heated. In addition, some gels swell in response to selected solvents and may therefore be used as hinges. For example, hydrophilic elastomers based on polyurethane (PU)/2-hydroxyethyl methacrylate (HEMA) swell significantly in acetic acid while the PDMS bulk planar sheet maintains its original size. This combination of various materials may be utilized for folding of 3D structures and twisting of helices.⁶¹

Case 2: Bilayer structures.

Figure 1.7b illustrates laminate structures composed of two distinct materials adhered together. The mismatch in mechanical response of the two layers in the bilayer to stimuli governs the folding behavior. A classic example is a thermal bimorph, featuring two material layers with distinctly different thermal expansion coefficients. The bilayer curls in response to heat. An alternative approach is to have one layer to be selectively responsive to a stimulus. In pioneering work using electroactive polymers (i.e. polypyrrole)/gold thin films as hinges, the polypyrrole (PPy) film can shrink (or swell) in response to ion diffusion in the electrolyte solution (sodium dodecylbenzenesulfonate, Na^+DBS^-), while the gold film constitutes an inert, passive substrate so that a stress difference drives folding.⁷¹

The difference in intrinsic stress built during the deposition process inside one active layer in a bilayer structure provides the driving force for bending/folding.^{72–76} The bilayer structure with an active polymer layer (e.g, thermally responsive poly(*N*-isopropylacrylamide)-based polymers, $T_{\text{transition}} \sim 33 \text{ }^{\circ}\text{C}$; ^{4,77,78} solvent responsive polyvinyl alcohol and poly(PEGMA-*co*-PEGDMA)⁷⁹) can swell or shrink upon changing pH, ionic strength, or temperature. Moreover, a closed microcage made of an SU8 epoxy (high thermal expansion coefficient) and diamond-like carbon (DLC) (low thermal expansion coefficient) can open upon heating.⁸⁰ A bilayer comprising layers with different bending moduli can be used as a pneumatic actuator.^{81–83}

Case 3: Macroscopically homogenous materials

Figure 1.7c describes a third approach that utilizes chemically homogeneous substrates. For example, shape memory polymers can be locally pre-programmed to temporary shapes and return back to a permanent shapes when a certain critical temperature is exceeded to achieve shape changing from 2D to 3D shapes out-of-plane in response to uniform or local stimuli.^{43,48,51,50,54,84–87} A typical example is shown in **Figure 1.5**. Light-responsive SMPs can bend due to local light exposure at ambient temperature (usually in UV wavelengths).^{52,88,89}

Some macroscopically homogenous planar materials can undergo shape-change to 3D structures under uniform stimuli due to gradients across the sheet. Pre-defined gradients of crosslink densities or filler concentration across the film may be utilized.^{72,90–93} For example, thermal rolling of a photo-crosslinkable copolymer based on poly(*N*-isopropylacrylamide)

(PNIPAM) can be induced by patterning both high and low swelling region caused by controlling UV curing time.^{91,93} A crosslink gradient (high crosslink density on the surface) for a negative photoresist SU-8 was generated via low exposure to UV.⁹⁰ The bending curvature of the laminate depends on the exposure to UV and film thickness. Materials such as magnetic nanoparticles can be embedded inside the polymer matrix during the curing process to create a gradient under external magnetic field. The resulting polymer sheet can fold/bend in response to external magnetic field.⁹²

1.2.2.2 Different Stimuli Utilized for Self-folding

The previous sections described strategies for designing folding responses that are inherent to the substrate. It is also possible to use stimuli strategies to trigger the folding by various forces including pneumatics, surface tension, intrinsic residual stresses, light, and heat.^{44,57-59} Representative examples of those strategies are summarized in **Table 1.1**. Our research on self-folding described in this thesis focuses specifically on thermal actuation due to its simplicity and the availability of thermal triggers (i.e., light, resistive heating, and thermal radiation).

Further insight into the folding mechanism involving diverse stimuli can be obtained by understanding the nature and role of nonhomogeneous strains or stresses in the hinge region due to mismatch of thermal expansion coefficients, elastic moduli, shrinkage, or swelling ratio. Therefore, the ability to generate stepwise or gradual changes in stress/strain (or in applied stimuli) is critical in comprehending self-folding and utilizing it in various applications.

Table 1.1 Representative research work on self-folding regarding different stimuli applied.

Stimuli	Materials	Scales	Advantages	Disadvantages	Reversibility
Thermal bimorph actuation ⁹⁴	bilayers with different thermal expansion coefficients (e.g., polymer/metal)	μm -mm	Able to trigger remotely	High temperature required for small folding, depends on degree of mismatch	Yes
Thermal-responsive shape memory ^{43,51,50,54}	Shape memory alloys & polymers	μm -mm	Large gripping force achieved	Programming of motion required for SMP; limited strain (<10%) for SMA	SMA can induce reversible folding
Thermal shrinkage of polyimide ^{64,65}	Polyimide	μm	Large angle displacement can be achieved (0~180°)	High temperature needed (~500 °C); pattern PI hinge; response in minutes	Yes
Swelling in bilayers ^{50,36,38,39}	Hydrogels; ionic polymers	μm -mm	Remote application of electric field	Trigger by electrolytes or special solvents	Yes
Light-induced shape memory ^{88,89,52}	Elastomers; gels; or polymers with photosensitive groups	μm -mm	Remote; room temperature	Usually requires UV	Yes
Pneumatics, ⁸¹⁻⁸³	Elastomers (e.g., Ecoflex, PDMS); Perylene;	mm	Inexpensive, light in weight, high loads; fast response time (ms~s) depending on air flow rate;	Tethering needed; Supply of liquid/gas needed; require mismatch in flexibility/modulus between both sides to asymmetrical bending	Yes
Thin-film stress ^{73-75,95}	Metal films (e.g., Chromium)	nm- μm	Intrinsic stress forces to trigger	Multistep fabrication, passive actuation; angle depends on stress, modulus, thickness	No
Surface tension ^{69,70}	Solder, Tin, poly(ϵ -caprolactone), etc.	nm-mm	Hinges can be sealed (locked)	High temperature to melt metals	No
Magnets ^{92,96-99}	Ferromagnetic materials	nm-mm	Remote control by magnetic field	Substrate required to hold the active structure; locking mechanism required to keep it in position	Yes
muscular actuation ^{100,101}	Muscular cells	mm-cm	Bio-mimic, triggered by biochemical environment	Limited by robustness and longevity of cells	Yes

1.2.2.3 Management of Stress/Strain Gradient to Control Folding Process

Bending Mechanism

A theoretical study on bending behavior of bilayered laminates offers useful information for folding/bending, which is induced by mismatch in stress (or strain) between the two layers. Studying the bending curvature in bilayered systems offers a measure of the effect of stress (or strain) on system performance. The general theory of bilayer bending is derived from the model of a bi-metal strip as given by Timoshenko in 1925 (**Figure 1.8**).¹⁰² Here bending is assumed to take place in one direction only and the heating of the strip is assumed to be uniform. The bending curvature of the bilayer can be described by Equation (1.1).¹⁰²

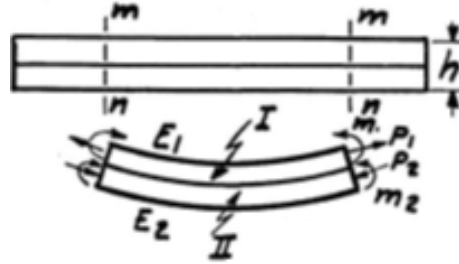


Figure 1.8. Schematics of bending of bi-metal strip.¹⁰² E_1 and E_2 are elastic moduli; α_1 and α_2 are thermal expansion coefficients for two layers separately; h_1 and h_2 are film thicknesses; and h is total thickness. P_1 is tensile force for layer 1 and P_2 is compressive force for layer 2.

$$\frac{1}{\kappa} = \frac{6(\alpha_2 - \alpha_1)(T - T_0)(1 + m)^2}{h \left[3(1 + m)^2 + (1 + mn) \left(m^2 + \frac{1}{mn} \right) \right]} \quad (1.1)$$

In Equation (1.1), κ is the curvature, h is the total thickness of bilayers, m is the h_1/h_2 ratio and n is the E_1/E_2 ratio. The sample is heated from the initial temperature T_0 to temperature

T. Equation (1.1) offers a guide to predict the bending curvature and impact parameters such as moduli, film thickness and temperature. However, Equation (1.1) only predicts uniform bending curvature and thus cannot predict the bending direction. Moreover, Equation (1.1) considers only elastic deformation so that it cannot be applied for viscoelastic polymers.

Recently, an analytical solution was introduced that predicts large deflections of circular or elliptical plates with lenticular cross-sectional shape when applying a temperature gradient across the film thickness.^{103,104} Self-rolling either from short side or long side has been demonstrated by controlling the ratio of length to width for a rectangular shape.^{105–107} For example, final rolling direction of epitaxially stressed $\text{In}_x\text{Ga}_{1-x}\text{As}/\text{GaAs}$ rectangular films was found to depend on the dimension (length and width) of the original film as well as the tube circumference. Long-side rolling occurred with high aspect ratio of the film or larger tube circumference than film width.

These early studies on bending curvature are based on systems with small volume changes and low stress (or strain) gradients due to internal stress of materials, limited thermal expansion mismatch or ion compensation, which is not suitable for polymers or hydrogels involving high swelling ratio.

Thermal Transport Study

Since thermal actuation is one of the most widely utilized mechanisms for self-folding, thermal analysis is necessary that correlates temperature changes with folding (e.g., bending curvature driven by mismatch of thermal expansion coefficient). For example, a thermal bimorph cantilever used as a thermo-mechanical actuator in micro-scale devices possesses a bilayer structure with asymmetrical thermal properties.¹⁰⁸ A thermal transient

analysis based on lumped capacitance method has been applied to estimate the heat transfer between the solid and its surroundings to predict the temperature change within the solid as a function of time. Subsequent analysis assumes that the temperature gradient inside the solid is negligible, which is usually true for MEMS devices. The energy balance can be expressed using Equations (1.2-1.4) to describe the displacement of the cantilever:

$$q_h A_h - h(T - T_\infty) A_c = \rho V c \frac{dT}{dt} \quad (1.2)$$

which gives the temperature profile:

$$\frac{T - T_\infty}{T_0 - T_\infty} = \exp\left(-\frac{t}{\tau_T}\right) + \frac{q_h A_h}{h(T - T_\infty) A_c} [1 - \exp\left(-\frac{t}{\tau_T}\right)] \quad (1.3)$$

where

$$\tau_T \equiv \frac{1}{h A_c} \rho V c = R_T C_T \quad (1.4)$$

In the Equations (1.2) and (1.3), q_h is power density, A_h is surface area being heated, h is convection coefficient for air, T_∞ is temperature of air, ρ is density of the solid, V is the volume of the solid materials, c is the thermal capacitance of the solid, T is temperature of the solid at time t , R_T is the resistance to convection and C_T is the lumped thermal capacitance.

If thermal actuation is triggered by means of Joule-heating, the temperature of bimorph beams can be governed by basic heat transport incorporating the heat generated through current (assuming that convection and radiation contribute little to heat losses):¹⁰⁹

$$k \frac{d^2 T}{dx^2} + J^2 \rho = 0 \quad (1.5)$$

$$J = \frac{V}{RA} = \frac{V}{\rho L} \quad (1.6)$$

In Equations (1.5-1.6), J is the current density, V is applied voltage, R is the resistance, A is cross section of the beam, L is the length of the wires for Joule-heating, ρ is resistivity, and k is thermal conductivity of the solid materials.

The method as introduced above, which applies Joule-heating on pre-strained polymer sheet to localize the thermal actuation, models the heat generation in the core region (i.e., polymer directly above the electrical trace) at a semi-infinite surface where the core region is at $x = 0$ and the margin extended away from the core is semi-infinite ($x \rightarrow \infty$). In this manner the basic heat transport solution can be applied.⁵⁰

Modeling of Shape Memory Polymer behavior

Because large and complex shape changes occur during pre-programming of SMPs, prediction of deformation history of SMPs is desired for optimization of property recovery.¹¹⁰ Constitutive models have been developed for thermally-activated SMPs based on thermo-mechanical properties of SMPs and fundamental understanding of structure-function relationships.¹¹⁰⁻¹¹² Different constitutive models limited to small deformation in 1D,¹¹³ based on multiphasic materials (active phase and frozen phase),¹¹⁴ and 3D finite deformation^{110,112} are based on volume fraction and explicit phases (glassy and rubbery phases). Recently, a constitutive model based on structural and stress relaxation has been developed.¹¹⁵

1.3 Strategies of Converting 2D plane to 2D with Surface Topography

There are many materials strategies and stimuli that can be utilized for shape programming of polymers to undergo changes from flat 2D sheets to planar structures bearing pre-defined

surface topographies. We discuss the most prominent materials and mechanisms to form surface topography responding inherently to the properties of the substrate. For example, we do not include lithography here.

1.3.1 Surface Topography via Buckles Formation

Buckling (or “wrinkling”) is a common phenomenon found in nature.^{116,117} Buckled surfaces typically form when a thin rigid film is placed on top of a thick elastic substrate and the bilayered laminate is exposed to an external stress (thermal expansion or mechanical stretching), as illustrated in **Figure 1.9**. For example, when a thin metal film is deposited on a thermally expanded polymer, buckles form during the cooling process to room temperature in response to release of the compressive stress in the metal film.¹¹⁸ Buckles can also form on a pre-stretched elastomer sheets with a rigid top film (e.g., metal, oxide or oxidized original surface with high degree of crosslinks) when introducing or releasing mechanical strain.¹¹⁹ In all cases, buckles form on top of the polymeric film with a ‘hard’ skin as a result of the balance between the energy of bending (top film) and stretching (bottom layer).^{117,120,121}

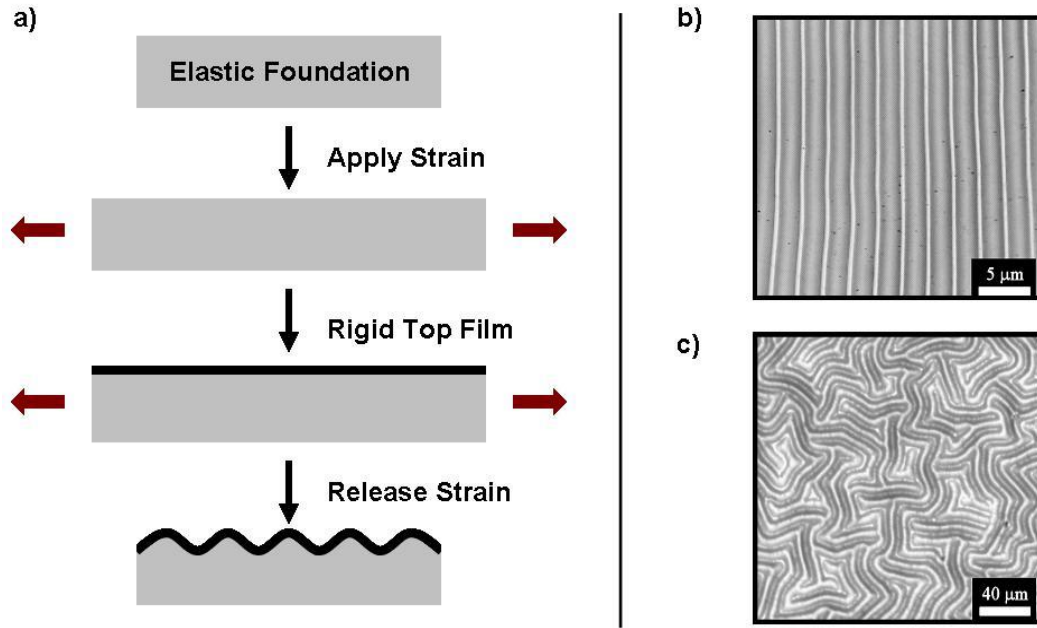


Figure 1.9. a) Schematic of the formation of buckles on an elastic substrate; b) optical microscopy images (top view) of typical unidirectional buckles and c) optical microscopy image of isotropic buckles (oriented in random directions).¹²⁰

Although buckling is a spontaneous process, the attributes of the buckles are controllable to some extent. Assuming relatively small strains and an infinitely thick foundation, there is a well-developed model that predicts the wavelength (λ) and amplitude (A) of the buckles:

$$\lambda = 2\pi h \left(\frac{(1-\nu_f^2)E_s}{3(1-\nu_s^2)E_f} \right)^{1/3} \quad (1.14)$$

$$A = h \left(\frac{\varepsilon}{\varepsilon_c} - 1 \right)^{1/2} \quad (1.15)$$

where the subscripts s and f denote the skin and the elastic foundation, respectively, E is Young's modulus, ν is Poisson's ratio, h is the thickness of the skin, ε is applied compressive

strain and ϵ_c is the critical value of ϵ .^{117,122} The wavelength based on an infinitely thick foundation is a function of materials' properties (i.e., Young's modulus and Poisson's ratio) and the amplitude depends on the wavelength and the applied strain.

Although elastomers (e.g., PDMS) have been widely used as soft substrates in most studies featuring buckling/wrinkling, other materials such as polymers, hydrogels and polymer brushes can also be used to form buckles.

1.3.1.1 Mechanism for Buckles Formation

Mechanical stretching

Buckles can form by mechanically stretching the elastic substrate. PDMS is used frequently as the elastic foundation due to its outstanding flexibility (Young's modulus of ≈ 1 MPa) and stretching ability.^{119,121} The skin can be manufactured by stiffening the surface of PDMS through oxidation by means of oxygen plasma or UV/Ozone (UVO) treatments, which transform the topmost regions of PDMS to a silica-like layer,¹¹⁹ or depositing metal or metal oxide (e.g., Au, Pt, ITO) on the pre-stretched elastomer substrate.^{118,123,124} Anisotropic buckles, i.e., arrangement of buckles in the direction perpendicular to the stretching direction, can be achieved after releasing uniaxially the mechanical strain, as shown in **Figure 1.10**.

Mechanical stretching can be applied by using a custom-designed stretcher (**Figure 1.10a**). A PDMS sheet was stretched uniaxially in the stretcher and then treated by oxygen plasma (Diener Electronic) or UVO (Jelight Inc.) to form an oxidized top thin film (Young's modulus of ~ 40 GPa)¹²¹ on the PDMS surface. After surface oxidization, the strain was released at a controlled rate. The release rate is known to affect the occurrence of defects and

cracks in the buckled topography; a fast strain release rate results in more defects, while a slow strain release rate generates numerous cracks.¹¹⁹

Atomic force microscopy (AFM) images of unidirectional buckles formed with by applying 50% strain are shown in **Figure 1.10b, c**. The aspect ratio, i.e., the ratio of the amplitude to the wavelength, of the buckles changed depending on the UVO dose, as shown in **Table 1.2**. The aspect ratio is a function of the materials' properties, the thickness of top rigid layer and the applied strain.^{118,119} The aspect ratio for buckles due to mechanical stretching is usually limited to ~ 0.2 .^{119,121}

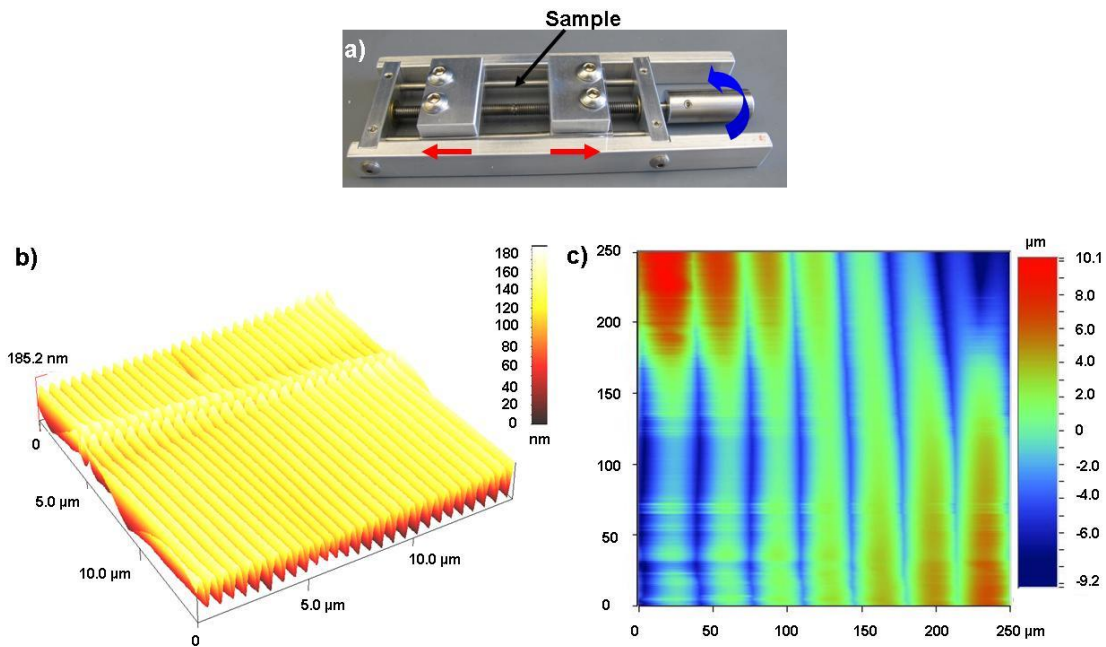


Figure 1.10. a) Photograph of the custom-designed stretcher. The sample such as a PDMS sheet is sandwiched tightly by screws, the sample is stretched axially (labeled in red) by rotating the shaft (labeled in blue); b) AFM image of unidirectional buckles on stretched PDMS with air plasma treated surface and c) Map scan by profilometry of unidirectional buckles on stretched PDMS with UVO treatment.

Table 1.2. The aspect ratio of buckles resulting from different UVO doses. The applied axial strain is 50% for all samples, and the thickness of PDMS is ≈ 1 mm. The power density of UVO is 7.6 mW/cm^2

UVO time (min)	UVO dose (J/cm^2)	Wavelength (μm)	Aspect ratio
45	20.6	≈ 42	0.08-0.10
60	27.5	≈ 48	0.12-0.16
75*	34.4	≈ 60	0.17-0.26

When a large strain is imposed, the resulting topography comprises hierarchically-structured buckles, where smaller buckles reside on top of larger ones (**Figure 1.11a**).^{117,119} Up to five generations of buckles (sizes ranging from nanometers to a fraction of a millimeter) have been detected by profilometry and scanning probe microscopy (**Figure 1.11b, c**).

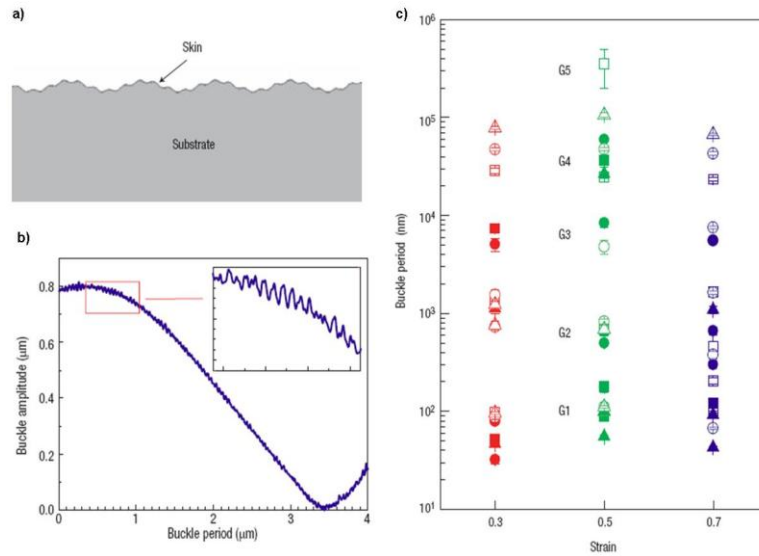


Figure 1.11. Hierarchically-buckled topography due to large strain applied to UV/Ozone-treated PDMS. a) Illustration of hierarchically-buckled topography; b) hierarchical profile collected by profilometry and c) wavelengths of multiple generations of buckles as a function of applied strains.¹¹⁹

Different metals can be deposited as a hard skin on the surface of pre-stretched elastomer sheets to form buckles upon releasing the strain from the sample. For example, Indium tin oxide (ITO) is used frequently in forming transparent electrodes in applications such as solar cells and flat panel displays for its optimal optical and electrical properties.¹²⁴ In our experiments, an ITO film (40 nm) was deposited onto a pre-stretched PDMS sheet (1 mm, $\epsilon \approx 10\%$) by sputtering. After ITO deposition, the strain was slowly released from the sample, which resulted in the formation of buckles.

The surface topography was studied by optical microscopy and a representative example is shown in **Figure 1.12**. The process exhibited a hysteretic behavior during the release-stretch cycle, as reported.¹²³ The as-sputtered film, without releasing the strain, already contained buckles aligned parallel to the stretching direction. The formation of such buckles can be explained as follows. Due to the large thermal expansion coefficient of PDMS ($\approx 96 \times 10^{-5} \text{ K}^{-1}$),¹²⁵ PDMS expands along the direction perpendicular to the side confined by the clamps due to the heat generated from sputtering. When the substrate is cooled down after sputtering, it shrinks to form buckles aligned parallel to the stretching direction.¹²⁶ The orientation of the buckles remains the same during the release and re-stretch. Cracks are formed at relatively slow strain release rates (images from $\epsilon \approx 6\%$ to less strain). The buckles align parallel to the stretching direction are recovered when $\epsilon \approx 12\%$.

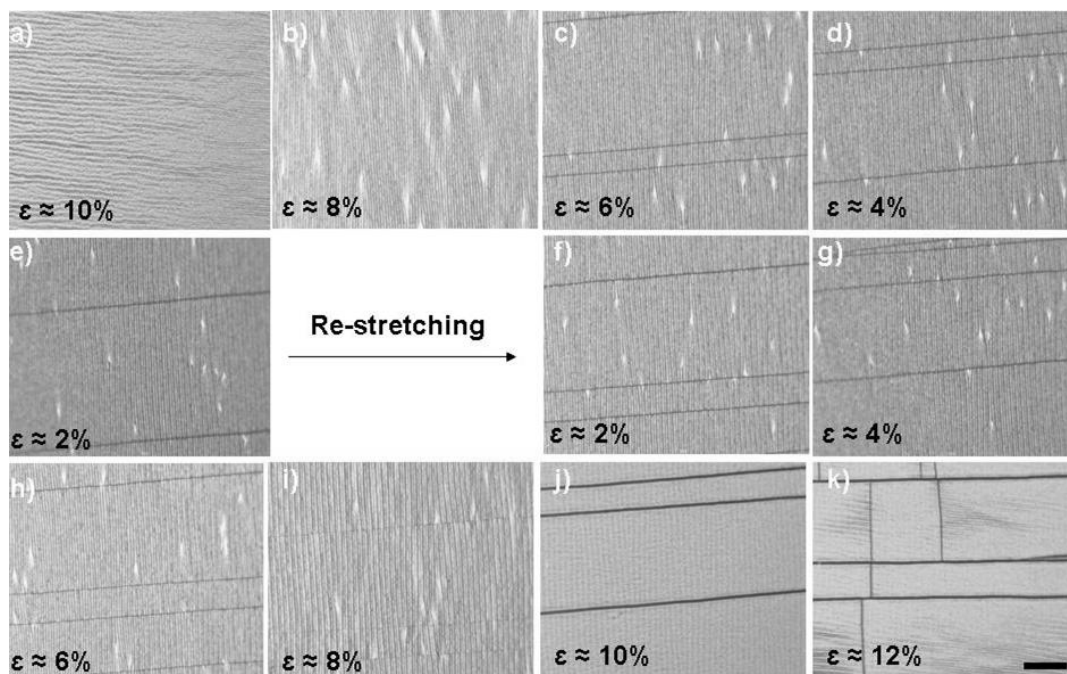


Figure 1.12. Optical microscopy images of buckles formation when releasing and re-applying strain on an ITO sputtered PDMS sheet. The image was first taken right after ITO sputtering ($\epsilon \approx 10\%$), more images were taken when slowly releasing the strain from 10% to 2%. The film was re-stretched after total release ($\epsilon \approx 0\%$) to $\epsilon \approx 10\%$ and overstretched to $\epsilon \approx 12\%$. The images were taken consecutively (scale bar: 20 μm for all images)

While elastomers, like PDMS, are popular as the substrates for buckle formation, generation of wrinkles by stretching other polymers (i.e., synthetic PET or rubbers) has also been demonstrated.¹²⁷

Thermal expansion

Another stress source for buckling originates from the mismatch of thermal expansion coefficients between top film and the bottom substrate. For example, PDMS possesses a high thermal expansion coefficient ($\approx 96 \times 10^{-5} \text{ K}^{-1}$).¹²⁵ A stiff skin can be formed by coating the PDMS foundation with a thin layer of a rigid material (e.g., Au, Pt, ITO).^{119,123,124} Because

the polymer substrate is heated and expanded either by external heat source before the deposition of top film or by energy generated during the deposition, a compressive stress develops in the top film upon cooling that competes with the tensile stress in the polymer substrate and results in the formation of buckles in random direction (isotropic buckles) **(Figure 1.9c)**.^{118,125}

Besides generating isotropic buckles by utilizing thermal expansion through pre-heating the substrate before or during the deposition of top metal film, isotropic buckles can be also formed during annealing of metal (metal oxide)/polymer bilayer films deposited on flat rigid substrates.^{128,129} For example, buckles can be formed after heating bilayer films of Al/PS resting on silicon substrates.¹²⁸ Here buckling takes place due to the mismatch of thermal expansion between the top capping film (Al, $25 \times 10^{-6} \text{ K}^{-1}$) and the bottom support (Si, $3 \times 10^{-6} \text{ K}^{-1}$). To test this hypothesis, by replacing Si with Zn as the support, no buckles are detected after heating the specimen, which can be explained by considering that the thermal expansion of Al and Zn is the same.

Other stress sources

There are other mechanisms that lead to the formation of buckled topographies, such as swelling. Swelling in polymer gels (e.g., hydrogels or photocurable resin) also induces buckling as shown in **Figure 1.13**.^{130–132}

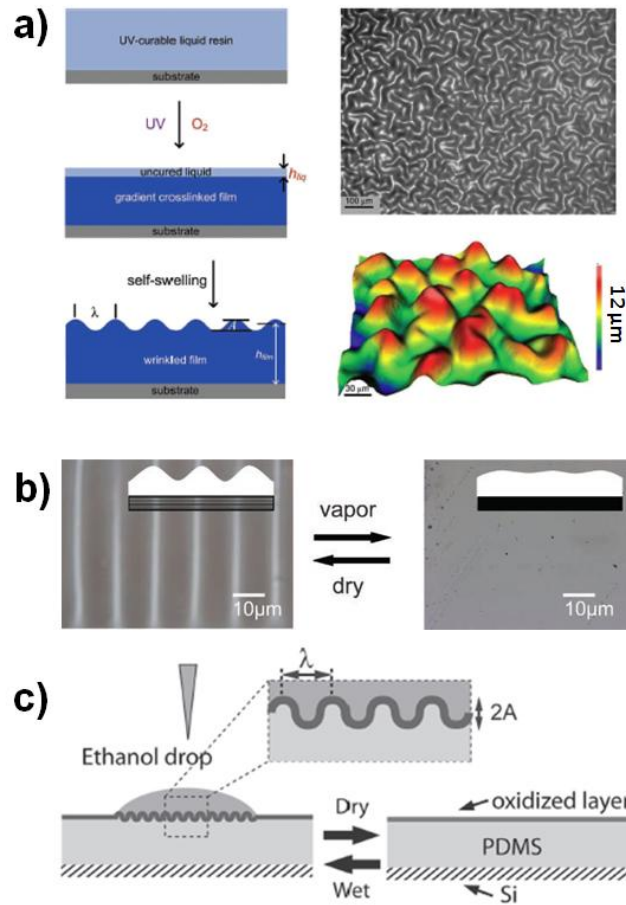


Figure 1.13. (a) Schematic, optical microscopy image and 3D profilometer image of isotropic buckles formed due to spontaneous swelling of a gradient crosslinked UV-curable resin (2-phenoxyethyl acrylate, crosslinker is 1,6-hexanediol diacrylate, photoinitiator is Irgacure 184).¹³⁰ (b) Optical microscopy images of ordered buckles on Polyacrylamide/NP-TiO₂-CTAB PVP hybrid gel before and after water vapor treatment. (CTAB: cetyltrimethylammonium bromide; NP-TiO₂: titania nanoparticles).¹³¹ (c) Schematic of reversible surface buckles of UVO-treated PDMS to oxidize the surface due to the swelling in response to different solvents.¹³²

1.3.1.2 Applications

The ability to form buckled surfaces has already been used to create smart surfaces with for various applications, including, anti-fouling coatings,^{14,133} microfluidic devices to

direct the cell growth,¹³⁴ smart adhesive surfaces,¹³⁵ optical devices such as microlenses and¹³⁶ diffraction gratings.^{122,125} Moreover, by making use of the buckling mechanism, buckled structures can be applied as a characterization tool to assess the modulus of materials employed as rigid thin layers.¹²² In addition, the application of buckled structures as light trapping surfaces has been explored.^{137–140} Hierarchical buckles are well-suited topographical structures that enhance trapping of light with various wavelengths since the buckle wavelengths range from micro- to the nano-scale.¹¹⁹ In contrast to previously fabricated light trapping structures (e.g., light-scattering reflector, V-shaped structure), buckled surfaces offer unprecedented means of tailoring topographies and sizes in a simple manner and are thus expected to be well-suited for fabrication of OPV devices that possess increased efficacy of light absorption. Buckling represents a simple fabrication method and does not require any complex processing steps beyond those already used to make planar devices.

We propose that a buckled substrate with corrugations and therefore improved light trapping provides a promising means of preparing high-efficiency OPV devices in a simple, low-cost manner. This will be further discussed in Chapter 6.

1.3.2 Surface Topography via Shape Memory Effect

3D surface topography on the planar substrate can be triggered by shape memory effect as well,^{15,141} which often results in the surface function change. As shown in **Figure 1.14**, the original surface topography (e.g., grating pattern) can be recovered by heating the samples (~ 120 °C). Light diffraction due to the grating pattern can be easily observed from the color change of the surface. This structure can be applied for optical harvesting devices

and optical sensors. Moreover, the surface topography recovered of a shape memory polymer has shown a repeatable, strong and reversible dry adhesion to a glass substrate.¹²

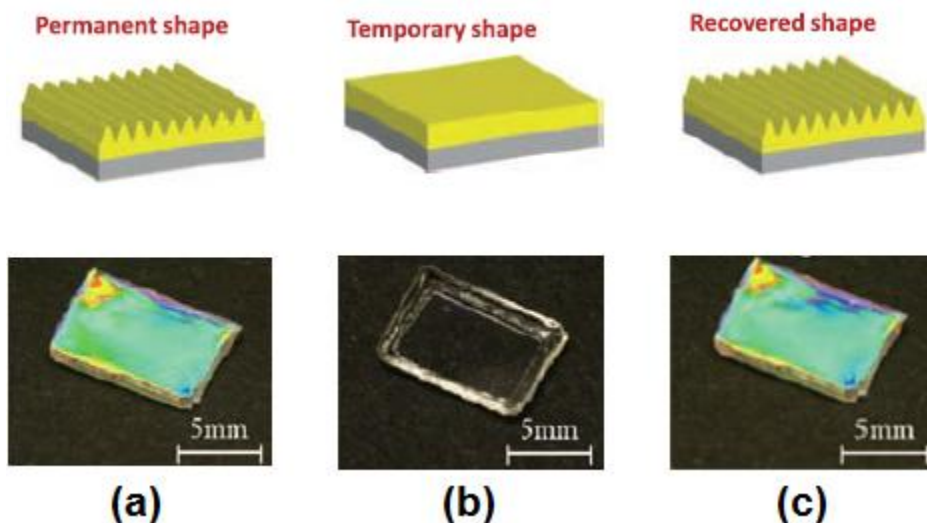


Figure 1.14. Surface topography due to shape memory effect in an acrylate-based SMP (cured from methyl methacrylate (MMA), poly(ethylene glycol dimethacrylate) (PEGDMA) as crosslinker and 2,2-dimethoxy-2-phenylacetodphenone (initiator)). Schematics (top) and images (bottom) for different stages: (a) permanent pattern molded by thermally embossing nanoimprint lithography at ~ 180 °C; (b) 2D planar surface after programming with a flat mold; and (c) recovered surface topography after heating at ~ 120 °C. The pattern has a pitch of ~ 800 nm and a height of ~ 180 nm.¹⁴¹

1.3.3 Surface Topography via Polymer Brushes

Changes in surface topography can be also induced by employing polymer brushes. The conformational change of brushes due to some external trigger can be employed in controlling surface wettability,^{142,143} or adhesion properties.^{144,145} For example, surface topography comprising ridging or blister patterns can form by treating electrolysis in a pulse to growing polymer brushes (poly(glycidyl methacrylate), PGMA) due to the local release of

Au-thiol bonds and so expansion in lateral direction. This can be applied in soft lithography stamping or in manufacture of nanofluidic channels.³¹

1.4 Summary and Dissertation Outline

In this review, we have introduced several fabrication strategies and stimuli mechanisms that can be used to convert 2D planar shape programmable polymeric materials to a 3D shapes, involving either out-of-plane bending or change of in-plane surface topography. Working with 2D sheets is attractive since these structures are compatible with many planar processes developed for semiconductor processing as well as many patterning techniques. In this Ph.D. dissertation we focus specifically on strategies that employ polymeric materials and thermal actuation to trigger self-folding of polymer sheets to generate 3D structures with various shapes and the formation of buckled surface topographies.

The general design that induces self-folding relies on the utilization of heterogeneous materials acting as hinges. This process requires multistep complex fabrications methods (e.g., lithography), or increases cost due to the need to pre-program the shape memory materials. Bilayer structures usually follow bending rather than folding with sharp edges due to the low strain and delocalized strain mismatch. We propose a simple way to realize self-folding of homogeneous pre-strained polymer sheets by employing conventional 2D printing techniques. Specifically, Chapter 2 introduces a simple and novel approach to self-folding by employing polymer sheets and high throughput 2D patterning techniques. The ink printed ink on selected regions on the sheet acts as a hinge by locally absorbing energy from a uniform light source and converting it to heat, which causes localized strain relaxation in the

sheet. Because the strain relaxes in a gradual manner across the sheet thickness, the film folds in the inked region. We have study experimentally the influence of key process parameters and modeled the thermal transport phenomenon to achieve precise control of folding. Chapter 3 provides an insight into the kinetics of this self-folding process based on pre-strained polymer sheets. We correlate the macroscopic, thermally-driven shrinkage behavior of pre-strained polystyrene sheets to the kinetics of self-folding of these sheets. The macroscopic shrinkage of pre-strained polymer sheets as a function of temperature, time and heating rate provides information about the kinetics of shrinkage of the polymer within the dynamic thermal environment that the polymer sheets experience during folding. A simple geometric model that incorporates these macroscopic measurements predicts successfully the maximum bending angle as well as the kinetics of folding process in the ‘hinge’ (*i.e.*, folding angle as a function of time). Different light (or heat) sources are capable programming self-folding of pre-strained polymer sheets. Chapter 4 demonstrates rapid self-folding of pre-strained polymer sheets using focused laser light. This hinging response occurs even without pre-defined hinges on a compositionally homogeneous polymer sheet. Chapter 5 investigates self-folding by adopting different ink colors and utilizing light-emitting diodes (LEDs) with various emitting wavelengths, which is appealing to realize sequential folding for many applications such as reconfigurable devices and complicated origami folding.

The second part of my Ph.D. dissertation (Chapter 6) discusses the formation of buckled topographies based on metal/metal oxide bilayers deposited on top of polymer films. Application of buckled topographies for the fabrication of organic solar cells to enhance light

trapping will be discussed in detail. Different approaches to amplify the aspect ratio of isotropic buckles will also be outlined.

References

1. Hawkes, E. *et al.* Programmable matter by folding. *Proc. Natl. Acad. Sci.* **107**, 12441–12445 (2010).
2. Rashed Khan, M., Hayes, G. J., So, J.-H., Lazzi, G. & Dickey, M. D. A frequency shifting liquid metal antenna with pressure responsiveness. *Appl. Phys. Lett.* **99**, 013501 (2011).
3. Cho, J.-H. *et al.* Nanoscale Origami for 3D Optics. *Small* **7**, 1943–1948 (2011).
4. Bassik, N., Abebe, B. T., Laflin, K. E. & Gracias, D. H. Photolithographically patterned smart hydrogel based bilayer actuators. *Polymer* **51**, 6093–6098 (2010).
5. Ilievski, F., Mazzeo, A. D., Shepherd, R. F., Chen, X. & Whitesides, G. M. Soft Robotics for Chemists. *Angew. Chem.* **123**, 1930–1935 (2011).
6. Small, W., Wilson, T. S., Benett, W. J., Loge, J. M. & Maitland, D. J. Laser-activated shape memory polymer intravascular thrombectomy device. *Opt Express* **13**, 8204–8213 (2005).
7. Small, IV, W., Singhal, P., Wilson, T. S. & Maitland, D. J. Biomedical applications of thermally activated shape memory polymers. *J. Mater. Chem.* **20**, 3356 (2010).
8. Kuribayashi, K. *et al.* Self-deployable origami stent grafts as a biomedical application of Ni-rich TiNi shape memory alloy foil. *Mater Sci Eng -Struct Mater Prop Microstruct Process* **419**, 131–137 (2006).
9. Henry, C. P., McKnight, G. P., Enke, A., Bortolin, R. & Joshi, S. 3D FEA simulation of segmented reinforcement variable stiffness composites</title></title> in (Dapino, M. J. & Ounaies, Z.) 69290X–69290X–12 (2008). doi:10.1117/12.778891
10. Morphees: Shape-shifting mobile devices (w/ Video). at <<http://phys.org/news/2013-04-morphees-shape-shifting-mobile-devices-video.html>>

11. MorePhone: Revolutionary shape-changing phone curls upon a call (w/ Video). at <<http://phys.org/news/2013-04-morephone-revolutionary-shape-changing-video.html>>
12. Eisenhaure, J. D., Xie, T., Varghese, S. & Kim, S. Microstructured Shape Memory Polymer Surfaces with Reversible Dry Adhesion. *ACS Appl. Mater. Interfaces* **5**, 7714–7717 (2013).
13. Blewitt, M. J. & Willits, R. K. The Effect of Soluble Peptide Sequences on Neurite Extension on 2D Collagen Substrates and Within 3D Collagen Gels. *Ann. Biomed. Eng.* **35**, 2159–2167 (2007).
14. Efimenko, K., Finlay, J., Callow, M. E., Callow, J. A. & Genzer, J. Development and Testing of Hierarchically Wrinkled Coatings for Marine Antifouling. *ACS Appl. Mater. Interfaces* **1**, 1031–1040 (2009).
15. Xu, H. *et al.* Deformable, Programmable, and Shape-Memorizing Micro-Optics. *Adv. Funct. Mater.* **23**, 3299–3306 (2013).
16. Strategic Polymer Sciences, Inc. - EMP Technology. at <http://www.strategicpolymers.com/technology/>>
17. Jaffe, B. *Piezoelectric Ceramics*. (Elsevier, 2012).
18. Pak, Y. E. Linear electro-elastic fracture mechanics of piezoelectric materials. *Int. J. Fract.* **54**, 79–100 (1992).
19. Wei, Z. G., Sandström, R. & Miyazaki, S. Shape-memory materials and hybrid composites for smart systems: Part I Shape-memory materials. *J. Mater. Sci.* **33**, 3743–3762 (1998).
20. Ambrosy, A. & Holdik, K. Piezoelectric PVDF films as ultrasonic transducers. *J. Phys. [E]* **17**, 856–859 (1984).
21. Shirinov, A. V. & Schomburg, W. K. Pressure sensor from a PVDF film. *Sensors Actuators Phys.* **142**, 48–55 (2008).

22. Spanner, K. & Koc, B. *An Overview of Piezoelectric Motors*. (Messe Bremen-Hvg Hanseatische Veranstaltungs-GmbH, 2010).
23. Jones, D. J., Prasad, S. E. & Wallace, J. B. in *Adv. Ceram. Mater. Appl. Adv. Mater. High-Tech Soc.* (Mostaghaci, H.) **122-1**, 71–143 (Trans Tech Publications Ltd, 1996).
24. Watson, B., Friend, J. & Yeo, L. Piezoelectric ultrasonic micro/milli-scale actuators. *Sensors Actuators Phys.* **152**, 219–233 (2009).
25. *NASA Piezoelectric Autonomous Responsivness (Plane Flapping Like a Bird)*. (2010). at http://www.youtube.com/watch?v=Vc_3uZNaAIU&feature=youtube_gdata_player
26. Hagood, N. W. & von Flotow, A. Damping of structural vibrations with piezoelectric materials and passive electrical networks. *J. Sound Vib.* **146**, 243–268 (1991).
27. Stuart, M. A. C. *et al.* Emerging applications of stimuli-responsive polymer materials. *Nat. Mater.* **9**, 101–113 (2010).
28. Luzinov, I., Minko, S. & Tsukruk, V. V. Responsive brush layers: from tailored gradients to reversibly assembled nanoparticles. *Soft Matter* **4**, 714 (2008).
29. Wu, T., Efimenko, K. & Genzer, J. Combinatorial Study of the Mushroom-to-Brush Crossover in Surface Anchored Polyacrylamide. *J. Am. Chem. Soc.* **124**, 9394–9395 (2002).
30. Zhou, F., Shu, W., Welland, M. E. & Huck, W. T. S. Highly Reversible and Multi-Stage Cantilever Actuation Driven by Polyelectrolyte Brushes. *J. Am. Chem. Soc.* **128**, 5326–5327 (2006).
31. Edmondson, S., Frieda, K., Comrie, J. E., Onck, P. R. & Huck, W. T. S. Buckling in Quasi-2D Polymers. *Adv. Mater.* **18**, 724–728 (2006).

32. Valiaev, A., Abu-Lail, N. I., Lim, D. W., Chilkoti, A. & Zauscher, S. Microcantilever Sensing and Actuation with End-Grafted Stimulus-Responsive Elastin-Like Polypeptides. *Langmuir* **23**, 339–344 (2007).
33. Serwer, P. Agarose gels: Properties and use for electrophoresis. *Electrophoresis* **4**, 375–382 (1983).
34. Peppas, N. A., Hilt, J. Z., Khademhosseini, A. & Langer, R. Hydrogels in Biology and Medicine: From Molecular Principles to Bionanotechnology. *Adv. Mater.* **18**, 1345–1360 (2006).
35. Hendrickson, G. R. & Andrew Lyon, L. Bioresponsive hydrogels for sensing applications. *Soft Matter* **5**, 29 (2009).
36. Ionov, L. Biomimetic Hydrogel-Based Actuating Systems. *Adv. Funct. Mater.* n/a–n/a (2013). doi:10.1002/adfm.201203692
37. Malda, J. *et al.* 25th Anniversary Article: Engineering Hydrogels for Biofabrication. *Adv. Mater.* n/a–n/a (2013). doi:10.1002/adma.201302042
38. Morales, D., Palleau, E., Dickey, M. D. & Velez, O. D. Electro-actuated Hydrogel Walkers with Dual Responsive Legs. *Soft Matter* (2013). doi:10.1039/c3sm51921j
39. Palleau, E., Morales, D., Dickey, M. D. & Velez, O. D. Reversible patterning and actuation of hydrogels by electrically assisted ionoprinting. *Nat. Commun.* **4**, (2013).
40. Song, J., Saiz, E. & Bertozzi, C. R. A New Approach to Mineralization of Biocompatible Hydrogel Scaffolds: An Efficient Process toward 3-Dimensional Bonelike Composites. *J. Am. Chem. Soc.* **125**, 1236–1243 (2003).
41. Kim, J., Hanna, J. A., Byun, M., Santangelo, C. D. & Hayward, R. C. Designing Responsive Buckled Surfaces by Halftone Gel Lithography. *Science* **335**, 1201–1205 (2012).
42. Wu, Z. L. *et al.* Three-dimensional shape transformations of hydrogel sheets induced by small-scale modulation of internal stresses. *Nat. Commun.* **4**, 1586 (2013).

43. Lendlein, A. & Kelch, S. Shape-Memory Polymers. *Angew. Chem. Int. Ed.* **41**, 2034 (2002).
44. Mavroidis, C. Pfeiffer, C. Mosley, M. Conventional actuators, shape memory alloys and electrorheological fluids. (1999)
45. Rousseau, I. A. & Mather, P. T. Shape Memory Effect Exhibited by Smectic-C Liquid Crystalline Elastomers. *J. Am. Chem. Soc.* **125**, 15300–15301 (2003).
46. Mavroidis, C., Pfeiffer, C. & Mosley, M. *Conventional Actuators, Shape Memory Alloys, And Electrorheological Fluids*. (1999).
47. Taboodada. Shape Memory And Iron Palladium Alloys. *taboodata.com* at <<http://taboodada.wordpress.com/2011/03/31/41/>>
48. Leng, J., Lan, X., Liu, Y. & Du, S. Shape-memory polymers and their composites: Stimulus methods and applications. *Prog. Mater. Sci.* **56**, 1077–1135 (2011).
49. Lee, A. P. *et al.* A practical microgripper by fine alignment, eutectic bonding and SMA actuation. *Sensors Actuators Phys.* **54**, 755–759 (1996).
50. Felton, S. M. *et al.* Self-folding with shape memory composites. *Soft Matter* **9**, 7688 (2013).
51. Lendlein, A. Biodegradable, Elastic Shape-Memory Polymers for Potential Biomedical Applications. *Science* **296**, 1673–1676 (2002).
52. Lendlein, A., Jiang, H., J ünger, O. & Langer, R. Light-induced shape-memory polymers. *Nature* **434**, 879–882 (2005).
53. Zhao, Y., Huang, W. M. & Fu, Y. Q. Formation of micro/nano-scale wrinkling patterns atop shape memory polymers. *J. Micromechanics Microengineering* **21**, 067007 (2011).

54. Behl, M., Razzaq, M. Y. & Lendlein, A. Multifunctional Shape-Memory Polymers. *Adv. Mater.* **22**, 3388–3410 (2010).
55. Brittain, S. T., Schueller, O. J. A., Wu, H., Whitesides, S. & Whitesides, G. M. Microorigami: Fabrication of Small, Three-Dimensional, Metallic Structures. *J. Phys. Chem. B* **105**, 347–350 (2001).
56. Pickett, G. T. Self-folding origami membranes. *Eur. Lett. EPL* **78**, 48003 (2007).
57. Leong, T. G., Zarafshar, A. M. & Gracias, D. H. Three-Dimensional Fabrication at Small Size Scales. *Small* **6**, 792–806 (2010).
58. Fernandes, R. & Gracias, D. H. Self-folding polymeric containers for encapsulation and delivery of drugs. *Adv. Drug Deliv. Rev.* **64**, 1579–1589 (2012).
59. Ionov, L. Soft microorigami: self-folding polymer films. *Soft Matter* **7**, 6786 (2011).
60. Ionov, L. Bioinspired Microorigami by Self-Folding Polymer Films. *Macromol. Chem. Phys.* **214**, 1178–1183 (2013).
61. Jeong, K.-U. *et al.* Three-dimensional actuators transformed from the programmed two-dimensional structures via bending, twisting and folding mechanisms. *J. Mater. Chem.* **21**, 6824 (2011).
62. Smela, E., Inganäs, O. & Lundström, I. Controlled Folding of Micrometer-Size Structures. *Science* **268**, 1735–1738 (1995).
63. Stoychev, G., Turcaud, S., Dunlop, J. W. C. & Ionov, L. Hierarchical Multi-Step Folding of Polymer Bilayers. *Adv. Funct. Mater.* **23**, 2295–2300 (2013).
64. Ebefors, T., Källvesten, E. & Stemme, G. Dynamic actuation of polyimide V-groove joints by electrical heating. *Sensors Actuators Phys.* **67**, 199–204 (1998).

65. Suzuki, K., Yamada, H., Miura, H. & Takanobu, H. Self-assembly of three dimensional micro mechanisms using thermal shrinkage of polyimide. *Microsyst. Technol.* **13**, 1047–1053 (2006).
66. Piqué A., Mathews, S. A., Charipar, N. A. & Birnbaum, A. J. Laser origami: a new technique for assembling 3D microstructures. in (Bachmann, F. G. *et al.*) 82440B–82440B–7 (2012). doi:10.1117/12.909187
67. Hawkes, E. *et al.* Programmable matter by folding. *Proc. Natl. Acad. Sci.* (2010).
68. Azam, A., Laflin, K. E., Jamal, M., Fernandes, R. & Gracias, D. H. Self-folding micropatterned polymeric containers. *Biomed. Microdevices* **13**, 51–58 (2011).
69. Cho, J.-H., Azam, A. & Gracias, D. H. Three Dimensional Nanofabrication Using Surface Forces [†]. *Langmuir* **26**, 16534–16539 (2010).
70. Leong, T. G., Lester, P. A., Koh, T. L., Call, E. K. & Gracias, D. H. Surface Tension-Driven Self-Folding Polyhedra. *Langmuir* **23**, 8747–8751 (2007).
71. Jager, E. W. H. Microrobots for Micrometer-Size Objects in Aqueous Media: Potential Tools for Single-Cell Manipulation. *Science* **288**, 2335–2338 (2000).
72. Huang, G., Mei, Y., Thurmer, D. J., Coric, E. & Schmidt, O. G. Rolled-up transparent microtubes as two-dimensionally confined culture scaffolds of individual yeast cells. *Lab. Chip* **9**, 263 (2009).
73. Bassik, N., Stern, G. M. & Gracias, D. H. Microassembly based on hands free origami with bidirectional curvature. *Appl. Phys. Lett.* **95**, (2009).
74. Arora, W. J., Nichol, A. J., Smith, H. I. & Barbastathis, G. Membrane folding to achieve three-dimensional nanostructures: Nanopatterned silicon nitride folded with stressed chromium hinges. *Appl Phys Lett* **88**, 3 (2006).
75. Leong, T. G., Benson, B. R., Call, E. K. & Gracias, D. H. Thin Film Stress Driven Self-Folding of Microstructured Containers. *Small* **4**, 1605–1609 (2008).

76. Ionov, L. Soft microorigami: self-folding polymer films. *Soft Matter* **7**, 6786–6791
77. Stoychev, G., Turcaud, S., Dunlop, J. W. C. & Ionov, L. Hierarchical Multi-Step Folding of Polymer Bilayers. *Adv. Funct. Mater.* **23**, 2295–2300 (2013).
78. Zakharchenko, S., Pureskiy, N., Stoychev, G., Stamm, M. & Ionov, L. Temperature controlled encapsulation and release using partially biodegradable thermo-magneto-sensitive self-rolling tubes. *Soft Matter* **6**, 2633 (2010).
79. Guan, J. J., He, H. Y., Hansford, D. J. & Lee, L. J. Self-folding of three-dimensional hydrogel microstructures. *J Phys Chem B* **109**, 23134–23137 (2005).
80. Luo, J. K. *et al.* Modelling and fabrication of low operation temperature microcages with a polymer/metal/DLC trilayer structure. *Sensors Actuators Phys.* **132**, 346–353 (2006).
81. Martinez, R. V., Fish, C. R., Chen, X. & Whitesides, G. M. Elastomeric Origami: Programmable Paper-Elastomer Composites as Pneumatic Actuators. *Adv. Funct. Mater.* **22**, 1376–1384 (2012).
82. Lu, Y.-W. & Kim, C.-J. Microhand for biological applications. *Appl. Phys. Lett.* **89**, 164101 (2006).
83. Shinya Kusuda, Satoshi Sawano & Satoshi Konishi. Fluid-resistive bending sensor having perfect compatibility with flexible pneumatic balloon actuator. in 615–618 (IEEE, 2007).
84. Cuevas, J. M. *et al.* Triple-shape memory effect of covalently crosslinked polyalkenamer based semicrystalline polymer blends. *Soft Matter* **8**, 4928 (2012).
85. Julich-Gruner, K. K., Löwenberg, C., Neffe, A. T., Behl, M. & Lendlein, A. Recent Trends in the Chemistry of Shape-Memory Polymers. *Macromol. Chem. Phys.* **214**, 527–536 (2013).
86. Small, W., Metzger, M. F., Wilson, T. S. & Maitland, D. J. Laser-activated shape memory polymer microactuator for thrombus removal following ischemic stroke:

- preliminary in vitro analysis. *IEEE J. Sel. Top. Quantum Electron.* **11**, 892–901 (2005).
87. Yakacki, C. M. *et al.* Unconstrained recovery characterization of shape-memory polymer networks for cardiovascular applications. *Biomaterials* **28**, 2255–2263 (2007).
 88. Suzuki, A. & Tanaka, T. Phase transition in polymer gels induced by visible light. *Nature* **346**, 345–347 (1990).
 89. Jiang, H. Y., Kelch, S. & Lendlein, A. Polymers Move in Response to Light. *Adv. Mater.* **18**, 1471–1475 (2006).
 90. Jamal, M., Zarafshar, A. M. & Gracias, D. H. Differentially photo-crosslinked polymers enable self-assembling microfluidics. *Nat. Commun.* **2**, 527 (2011).
 91. Kim, J., Hanna, J. A., Hayward, R. C. & Santangelo, C. D. Thermally responsive rolling of thin gel strips with discrete variations in swelling. *Soft Matter* **8**, 2375–2381 (2012).
 92. Liu, Y. *et al.* Programmable responsive shaping behavior induced by visible multi-dimensional gradients of magnetic nanoparticles. *Soft Matter* **8**, 3295 (2012).
 93. Kim, J., Hanna, J. A., Byun, M., Santangelo, C. D. & Hayward, R. C. Designing Responsive Buckled Surfaces by Halftone Gel Lithography. *Science* **335**, 1201–1205 (2012).
 94. Luo, J. K. *et al.* Modelling and fabrication of low operation temperature microcages with a polymer/metal/DLC trilayer structure. *Sensors Actuators Phys.* **132**, 346–353 (2006).
 95. Tyagi, P. *et al.* Self-Assembly Based on Chromium/Copper Bilayers. *J. Microelectromechanical Syst.* **18**, 784–791 (2009).
 96. Boncheva, M. Magnetic self-assembly of three-dimensional surfaces from planar sheets. *Proc. Natl. Acad. Sci.* **102**, 3924–3929 (2005).

97. In, H. J., Lee, H., Nichol, A. J., Kim, S.-G. & Barbastathis, G. Carbon nanotube-based magnetic actuation of origami membranes. *J. Vac. Sci. Technol. B Microelectron. Nanometer Struct.* **26**, 2509 (2008).
98. Iwase, E. & Shimoyama, I. Multistep sequential batch assembly of three-dimensional ferromagnetic microstructures with elastic hinges. *J. Microelectromechanical Syst.* **14**, 1265–1271 (2005).
99. Yi, Y. W. & Liu, C. Magnetic actuation of hinged microstructures. *J. Microelectromechanical Syst.* **8**, 10–17 (1999).
100. Feinberg, A. W. *et al.* Muscular Thin Films for Building Actuators and Powering Devices. *Science* **317**, 1366–1370 (2007).
101. Xi, J., Schmidt, J. J. & Montemagno, C. D. Self-assembled microdevices driven by muscle. *Nat. Mater.* **4**, 180–184 (2005).
102. Timoshenko, S. ANALYSIS OF BI-METAL THERMOSTATS. *J. Opt. Soc. Am.* **11**, 233 (1925).
103. Mansfield, E. H. Bending, Buckling and Curling of a Heated Thin Plate. *Proc. R. Soc. Math. Phys. Eng. Sci.* **268**, 316–327 (1962).
104. Mansfield, E. H. Bending, Buckling and Curling of a Heated Elliptical Plate. *Proc. R. Soc. Math. Phys. Eng. Sci.* **288**, 396–417 (1965).
105. Cendula, P., Kiravittaya, S., Mönch, I., Schumann, J. & Schmidt, O. G. Directional Roll-up of Nanomembranes Mediated by Wrinkling. *Nano Lett.* **11**, 236–240 (2011).
106. Chun, I. S., Challa, A., Derickson, B., Hsia, K. J. & Li, X. Geometry Effect on the Strain-Induced Self-Rolling of Semiconductor Membranes. *Nano Lett.* **10**, 3927–3932 (2010).
107. Alben, S., Balakrisnan, B. & Smela, E. Edge Effects Determine the Direction of Bilayer Bending. *Nano Lett.* **11**, 2280–2285 (2011).

108. Baglio, S., Castorina, S., Fortuna, L. & Savalli, N. Modeling and design of novel photo-thermo-mechanical microactuators. *Sensors Actuators Phys.* **101**, 185–193 (2002).
109. Luo, J. K. *et al.* Fabrication and characterization of diamond-like carbon/Ni bimorph normally closed microcages. *J. Micromechanics Microengineering* **15**, 1406–1413 (2005).
110. Qi, H. J., Nguyen, T. D., Castro, F., Yakacki, C. M. & Shandas, R. Finite deformation thermo-mechanical behavior of thermally induced shape memory polymers. *J. Mech. Phys. Solids* **56**, 1730–1751 (2008).
111. Nguyen, T. D., Jerry Qi, H., Castro, F. & Long, K. N. A thermoviscoelastic model for amorphous shape memory polymers: incorporating structural and stress relaxation. *J. Mech. Phys. Solids* **56**, 2792–2814 (2008).
112. Diani, J., Liu, Y. & Gall, K. Finite strain 3D thermoviscoelastic constitutive model for shape memory polymers. *Polym. Eng. Sci.* **46**, 486–492 (2006).
113. Tobushi, H., Okumura, K., Hayashi, S. & Ito, N. Thermomechanical constitutive model of shape memory polymer. *Mech. Mater.* **33**, 545–554 (2001).
114. Liu, Y., Gall, K., Dunn, M. L., Greenberg, A. R. & Diani, J. Thermomechanics of shape memory polymers: uniaxial experiments and constitutive modeling. *Int. J. Plast.* **22**, 279–313 (2006).
115. Nguyen, T., Qi, H. J., Castro, F. & Long, K. A thermoviscoelastic model for amorphous shape memory polymers: Incorporating structural and stress relaxation. *J. Mech. Phys. Solids* **56**, 2792–2814 (2008).
116. Khang, D.-Y., Rogers, J. A. & Lee, H. H. Mechanical Buckling: Mechanics, Metrology, and Stretchable Electronics. *Adv. Funct. Mater.* **19**, 1526–1536 (2009).
117. Genzer, J. & Groenewold, J. Soft matter with hard skin: From skin wrinkles to templating and material characterization. *Soft Matter* **2**, 310 (2006).

118. Bowden, N., Brittain, S., Evans, A. G., Hutchinson, J. W. & Whitesides, G. M. Spontaneous formation of ordered structures in thin films of metals supported on an elastomeric polymer. *Nature* **393**, 146–149 (1998).
119. Efimenko, K. *et al.* Nested self-similar wrinkling patterns in skins. *Nat. Mater.* **4**, 293–297 (2005).
120. Stafford, C. M., Guo, S., Harrison, C. & Chiang, M. Y. M. Combinatorial and high-throughput measurements of the modulus of thin polymer films. *Rev. Sci. Instrum.* **76**, 062207 (2005).
121. Chiche, A., Stafford, C. M. & Cabral, J. T. Complex micropatterning of periodic structures on elastomeric surfaces. *Soft Matter* **4**, 2360 (2008).
122. Stafford, C. M. *et al.* A buckling-based metrology for measuring the elastic moduli of polymeric thin films. *Nat. Mater.* **3**, 545–550 (2004).
123. Ohzono, T. & Shimomura, M. Geometry-Dependent Stripe Rearrangement Processes Induced by Strain on Preordered Microwrinkle Patterns. *Langmuir* **21**, 7230–7237 (2005).
124. Park, S. K., Han, J. I., Kim, W. K. & Kwak, M. G. Deposition of indium–tin-oxide films on polymer substrates for application in plastic-based flat panel displays. *Thin Solid Films* **397**, 49–55 (2001).
125. Shih, T.-K., Ho, J.-R., Liao, H.-Y., Chen, C.-F. & Liu, C.-Y. Fabrication of optical gratings by shrinkage of a rubber material. *Thin Solid Films* **516**, 5339–5343 (2008).
126. Watanabe, M. Wrinkles formed on a thin gold film deposited onto stretched elastic substrates. *Polym. Adv. Technol.* **16**, 744–748 (2005).
127. Volynskii, A. L., Bazhenov, S., Lebedeva, O. V. & Bakeev, N. F. Mechanical buckling instability of thin coatings deposited on soft polymer substrates. *J. Mater. Sci.* **35**, 547–554 (2000).

128. Okayasu, T., Zhang, H.-L., Bucknall, D. G. & Briggs, G. A. D. Spontaneous Formation of Ordered Lateral Patterns in Polymer Thin-Film Structures. *Adv. Funct. Mater.* **14**, 1081–1088 (2004).
129. Kim, J. & Lee, H. H. Wave formation by heating in thin metal film on an elastomer. *J. Polym. Sci. Part B Polym. Phys.* **39**, 1122–1128 (2001).
130. Chandra, D. & Crosby, A. J. Self-Wrinkling of UV-Cured Polymer Films. *Adv. Mater.* **23**, 3441–3445 (2011).
131. Takahashi, M. *et al.* Photo-Fabrication of Titania Hybrid Films with Tunable Hierarchical Structures and Stimuli-Responsive Properties. *Adv. Mater.* **22**, 3303–3306 (2010).
132. Kim, H. S. & Crosby, A. J. Solvent-Responsive Surface via Wrinkling Instability. *Adv. Mater.* **23**, 4188–4192 (2011).
133. Genzer, J. & Efimenko, K. Recent developments in superhydrophobic surfaces and their relevance to marine fouling: a review. *Biofouling* **22**, 339–360 (2006).
134. Yoo, P. J., Park, S. Y., Kwon, S. J., Suh, K. Y. & Lee, H. H. Microshaping metal surfaces by wave-directed self-organization. *Appl. Phys. Lett.* **83**, 4444 (2003).
135. Chan, E. P. & Crosby, A. J. Fabricating Microlens Arrays by Surface Wrinkling. *Adv. Mater.* **18**, 3238–3242 (2006).
136. Chandra, D., Yang, S. & Lin, P.-C. Strain responsive concave and convex microlens arrays. *Appl. Phys. Lett.* **91**, 251912 (2007).
137. Kolaric, B., Vandeparre, H., Desprez, S., Vallée, R. A. L. & Damman, P. In situ tuning the optical properties of a cavity by wrinkling. *Appl. Phys. Lett.* **96**, 043119 (2010).
138. Koo, W. H. *et al.* Light extraction from organic light-emitting diodes enhanced by spontaneously formed buckles. *Nat. Photonics* **4**, 222–226 (2010).

139. Koo, W. H. *et al.* Polarization Conversion in Surface-Plasmon-Coupled Emission from Organic Light-Emitting Diodes Using Spontaneously Formed Buckles. *Adv. Mater.* **23**, 1003–1007 (2011).
140. Kim, J. B. *et al.* Wrinkles and deep folds as photonic structures in photovoltaics. *Nat. Photonics* **6**, 327–332 (2012).
141. Wang, Z. *et al.* Programmable, Pattern-Memorizing Polymer Surface. *Adv. Mater.* **23**, 3669–3673 (2011).
142. Motornov, M. *et al.* Stimuli-Responsive Colloidal Systems from Mixed Brush-Coated Nanoparticles. *Adv. Funct. Mater.* **17**, 2307–2314 (2007).
143. Wu, T., Efimenko, K., Vlček, P., Šubr, V. & Genzer, J. Formation and Properties of Anchored Polymers with a Gradual Variation of Grafting Densities on Flat Substrates. *Macromolecules* **36**, 2448–2453 (2003).
144. Sheparovych, R., Motornov, M. & Minko, S. Adapting Low-Adhesive Thin Films from Mixed Polymer Brushes. *Langmuir* **24**, 13828–13832 (2008).
145. Sheparovych, R., Motornov, M. & Minko, S. Low Adhesive Surfaces that Adapt to Changing Environments. *Adv. Mater.* **21**, 1840–1844 (2009).

CHAPTER 2

Self-folding of Polymer Sheets Using Local Light Absorption*

* This chapter is partially based on Y. Liu, J. K. Boyles, J. Genzer., M. D. Dickey, *Soft Matter*, 2012, 8, 1764 and M. D. Dickey, Y. Liu, J. Genzer, *SPIE newsroom*, 2012.

2.1 Introduction

This chapter describes a simple approach for converting two-dimensional (2D) patterns on polymer sheets into 3D objects. Conventional high-throughput patterning techniques (i.e., photolithography, screen printing, and inkjet printing) are inherently 2D. However, the ability to convert 2D patterns into 3D structures is attractive for a number of applications, including assembly, packaging, and mechanical actuation. Self-folding is a deterministic assembly process that causes a predefined 2D template to fold into a desired 3D structure with high fidelity.¹ Self-folding has been used for robotic actuators and sensors,^{2,3} containers for drug delivery and biological devices,⁴⁻⁶ solar cells⁷ and reconfigurable devices.⁸

The general strategy for self-folding involves defining hinges on planar surfaces that fold in response to an external stimulus. Previous efforts for self-folding have been accomplished by harnessing various forces including surface tension,^{7,9} intrinsic residual stress of thin films^{2, 10-12} and stress generated by external stimuli (e.g., magnets,^{13,14} pneumatics,¹⁵ swelling,¹⁶ heat,^{8,17-19} light,²⁰⁻²² and chemical modification¹⁷). Thermal actuation, the approach used here, represents a particularly attractive strategy because of its simplicity and the availability of thermal triggers (i.e., light, Joule heating, and thermal radiation).

Most examples of self-folding employ hinges that actuate when the substrate is exposed evenly to an external stimulus. Hinges can be defined in shape memory polymers (SMPs)^{19, 23-25} that return to a pre-programmed shape when a certain critical temperature is exceeded (*cf.* **Figure 2.1a**). SMPs have been designed and synthesized to respond to various

stimuli, including heat^{19,22,26} and light.^{20,27} The use of SMPs typically requires processing at elevated temperatures and necessitates pre-programming the desired shape (in contrast, our approach induces a uniformly deformed SMP to fold into shapes that are not pre-programmed in the SMP). An alternative approach is to define hinges composed of a material (or stack of materials) that differs from the bulk substrate such that only the hinges respond to a uniform stimulus (*cf.* **Figure 2.1b**). Examples include polyimide hinges that shrink at temperatures >500 °C,^{18,28} and shape memory metal alloys that actuate with Joule-heating.^{1,8} These methods require multiple fabrication steps to define the hinges since they must differ in chemical composition from the folding ‘panels’. Multilayer film stacks (*cf.* **Figure 2.1c**) with different thermal expansion coefficients or swelling ratios can also be employed as hinges.^{25, 29-32}

Our approach to self-folding (**Figure 2.1d**) employs localized absorption of light from an inexpensive infrared (IR) light bulb on an otherwise compositionally homogenous sheet of shape memory polymer to convert a uniform external triggering stimulus (i.e., unfocused light) into a hinging response. This approach uses mass-produced materials without the use of multiple fabrication steps.^{1,33} Black ink defines the hinges, which can be patterned, in principle, by nearly any conventional printing process; we chose to use a desktop printer out of simplicity. The polymer directly underneath the ink heats rapidly to exceed the glass transition temperature (T_g) of the polymer. As a result, the hinged regions relax and bend the sheet. Bidirectional folding (i.e., folding both toward the light source and away from the source) can be realized by patterning black ink on opposite sides of the polymer film as schematized in **Figure 2.1d**.

We use sheets of inkjet printable Shrinky-Dinks, commercially available toys composed of pre-stressed polystyrene shrink sheets (the printable versions of Shrinky-Dinks include a proprietary surface coating to improve adhesion of ink or toner).^{34,35} Pre-stressed polymer sheets are essentially shape memory materials that are fabricated by heating the polymer above T_g , stretching, and subsequently cooling below T_g to preserve the deformed shape.³⁶ As a consequence of such processing, the stress stored temporarily in the films releases rapidly when heated above the T_g (e.g., sheets of Shrinky Dinks contract in-plane by 50-60% in both the x and y dimensions³⁴; cf. **Figure S2.1** in the supporting information). Shrinky-Dinks have been used previously as substrates for the fabrication of microfluidic chips^{34,35} the densification of metal microdot arrays,³⁷ and the topographical patterning of surfaces³⁸ All of these applications make use of uniform heating of Shrinky-Dinks to cause the entire film to shrink. In contrast, our self-folding process requires rapid local heating of the hinges to induce self-folding. We achieve hinging without doing any shape pre-programming by selectively heating small regions of the sheets. In this study, we demonstrate and characterize this simple self-folding process experimentally and present a simple theoretical model that provides insight into the folding mechanism.

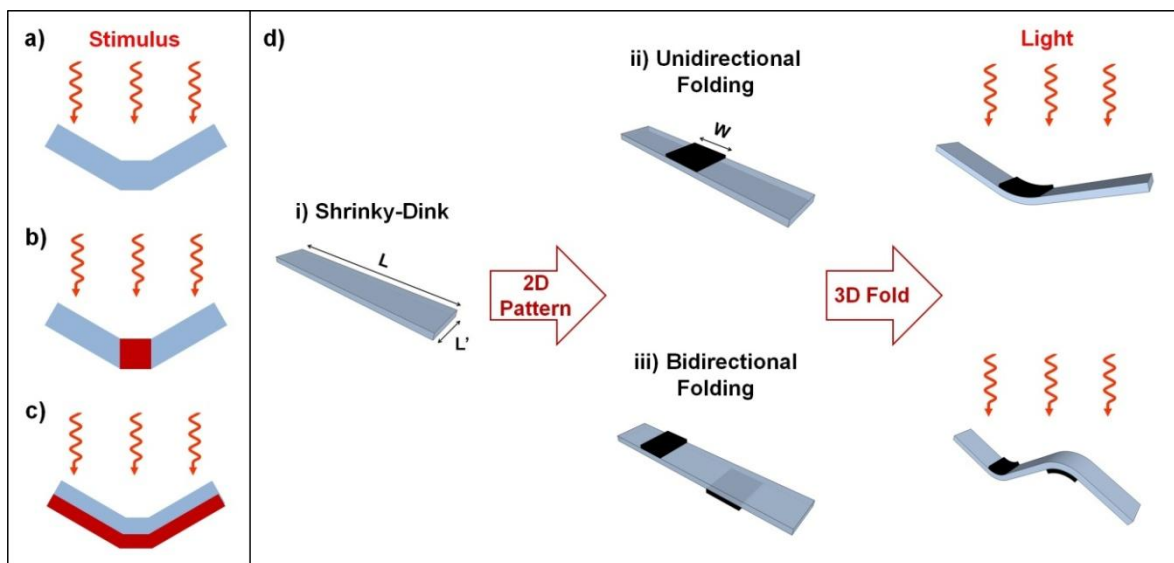


Figure 2.1. Schematic of different approaches to self-folding via thermal actuation (a-c are in cross-sectional view). Previous approaches include folding induced by²⁵: a) pre-programming of shape memory polymers; b) responsive hinges (red) composed of materials that differ from the bulk (blue); c) expansion mismatch of multilayer film stacks; and d) Our approach uses a uniform sheet and an even stimulus that is localized by surface patterns: i) A plain Shrinky-Dink; ii) Unidirectional folding via absorption of light by black ink (width, w) patterned on one side of the Shrinky-Dink; and iii) Bidirectional folding due to ink on both sides of the transparent Shrinky-Dink. Due to effective light absorption by the ink, the polymer under the black ink heats up faster than the rest of the polymer. The thicknesses of polymer films and black ink are not drawn to scale.

2.2 Experimental

A desktop laser printer (HP-P3005dn) produced 2D patterns (designed in CorelDRAW[®]) onto clear inkjet Shrinky-Dinks (Grafix Shrink Film). We cut the patterned polymer sheets into smaller samples (e.g., $L = 25$ mm, $L' = 10$ mm). An unfocused IR heat lamp (S4998, Satco) placed a constant distance of 5 cm from the polymer films to provide consistent light intensity for each experiment. We centered the polymer films under the lamp to improve the

uniformity of irradiation. A thermopile (818P-001-12, Newport) measured the flux to be 988 mW/cm² at this distance. In some cases, we carried out the the folding experiments on a hot plate (EchoTherm™ HS30, Torrey Pines Scientific) to raise the support temperature of the polymer sheet closer to T_g prior to irradiation. We separated the samples from the hotplate using a 0.5 mm thick polydimethylsiloxane (PDMS) network sheet to minimize heat flux at the bottom of the Shrinky Dink during exposure to light (the surface of the PDMS was typically ~ 2 °C within the hot plate temperature).

2.3 Results and Discussion

We patterned black toner on Shrinky-Dinks using a desktop printer and induced folding by placing the sheets under an IR light bulb at a set distance (5 cm from the lamp). The samples folded typically within seconds upon exposure to the light. The folding time required to complete folding depends on the intensity of the IR light (fixed in our experiment at 988 mW/cm²), the hinge width (w), and the temperature (T_S) of the base support (e.g., a hot plate on which the 2D patterned sheet rested during the IR light exposure). The folding angle (α_F , the angle between two adjacent facets on the inked side of the hinge) can be controlled by varying the exposure time to light and the shape, size, and pattern of the inked region that defines the hinge. For clarity, we note that α_F is related complementarily to the angular displacement of the fold (α_B) as $\alpha_F = 180^\circ - \alpha_B$. For instance, to achieve a folding angle of 60°, the originally flat sheet has to bend by 120°.

Figures 2.2a-c depict three examples of 3D folds generated via our approach. The left column depicts the 2D structures before irradiation with IR light and the right column

displays the corresponding 3D structures after self-folding. **Figures 2.2b, c** demonstrate bidirectional folding of patterned Shrinky-Dinks; black ink patterned on the backside of the sheet absorbs the IR light that passes through the sheet (The sheets are slightly hazy due to light scattering, but transmit light effectively as shown in Figure S1. Measurements using an integrating sphere attachment on a UV-Vis spectrometer show ~90% transmission.). White Shrinky-Dinks featuring patterns of black lines also undergo unidirectional self-folding, but bidirectional folding requires transparent substrates.

Self-folding can form 3D structures, including rectangular and polyhedral boxes, as shown in **Figures 2.2d-f**. The folding angle generated by a single hinge is typically 90° , which is convenient for forming boxes. The folding angle can, however, range from 60° to 90° depending on the exposure to light exposure time and the width of the hinge (*cf.* **Table S2.1** in the supporting information). We created tetrahedral boxes by defining hinges with folding angles of 60° (*cf.* **Figures 2.2e, f**). Single line hinges with line widths narrower than 2 mm result in folding angles larger than 60° and thus incomplete closing of the tetrahedral box. This limitation can be overcome by increasing the width of the printed line (*cf.* **Figure 2.2e**). Alternatively, adjacent parallel lines (*cf.* **Figure 2.2f**) also produce hinges that possess small folding angles (*cf.* **Table S2.2** in the supporting information). These empirical results suggest that various 3D structures can be realized by controlling the line width and pattern of the hinge.

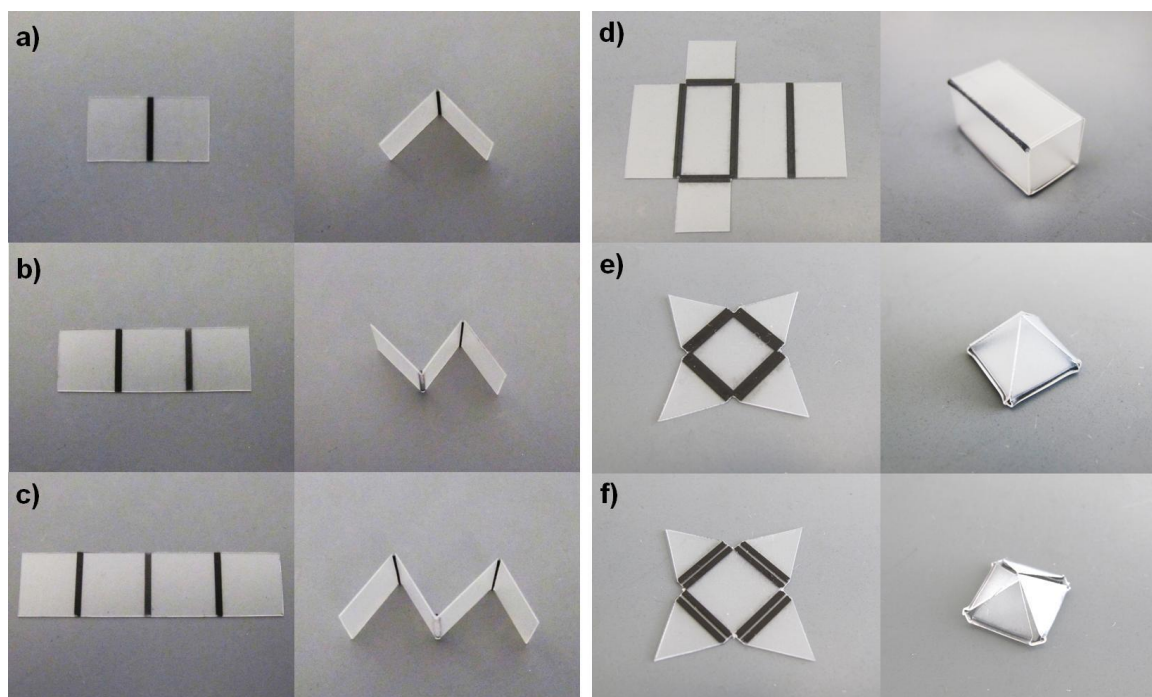


Figure 2.2. Photographs of 3D structures created by self-folding of Shrinky-Dinks patterned with a desktop printer. a) Single line ($w = 1$ mm, $L' = 10$ mm) patterned on the top side of the Shrinky-Dink; b) two lines ($w = 1$ mm, 12 mm spacing, $L' = 10$ mm) patterned on either side of the Shrinky-Dink; c) three lines patterned on alternating sides of the Shrinky-Dink ($w = 1$ mm, 12 mm spacing, $L' = 10$ mm); d) rectangular box (20 mm x 10 mm x 10 mm, $w = 1.5$ mm); e) tetrahedral box ($w = 2.0$ mm); and f) tetrahedral box with adjacent double hinges ($w = 1.0$ mm, inter-hinge spacing 0.3 mm). Both tetrahedrons have a square bottom facet (10 mm x 10 mm) and equilateral triangles on the other facets.

We measured the surface temperature of the polymer sheet as a function of time during exposure to light using an IR camera (FLIR A325). The measurements reveal that folding begins when the surface of the hinge exceeds 120 °C (*cf.* **Figure S2.2** in the supporting information), which is above T_g of the polymer sheet (≈ 102.7 °C, as measured by differential scanning calorimetry). At temperatures above T_g , the polymer starts relaxing to

obtain sufficient shrinkage for folding. Notably, the temperature of the non-patterned regions of the polymer does not change significantly in most cases (e.g., a sheet pre-heated to 80 °C stays within the range of 80 - 90 °C during folding).

We performed systematic experimental measurements to study the impact of the line width and the temperature of the support on the onset of folding. For these studies, we define the ‘onset of folding’ as the exposure time to the IR source required to initiate folding as observed by the naked eye. Since heat is required for folding, it is intuitive that faster onset of folding times occur at higher T_S values (which require less light absorption to generate the heat required to exceed T_g) and larger w values (which provide more heat absorption), as shown in **Figure 2.3a**. With T_S set to 90 °C, folding commences within one second regardless of the width of the patterned line (2.0 mm down to 0.5 mm, $w < 0.5$ mm gives imperfect folding). Lines having w ranging from 1.5 mm to 2.0 mm at T_S values of 50 °C and 70 °C also initiate folding at a similar rate. At the other extreme, T_S at 20 °C and line widths < 0.7 mm, folding occurs after prolonged exposure times, which results in imperfect folding and deformation of non-hinged regions of the substrate (**Figure S2.3** in the supporting information shows deformed panels resulting from over exposure to light). During long exposure times, heat dissipates and is no longer localized at the hinge; this observation underscores the importance of differential heating of the hinge relative to the facets.

We modeled the temperature profile inside the polymer films using COMSOL Multiphysics 4.0a software and compared the simulation results to the experimental measurements to gain more insight into the folding mechanism. The model assumes that (1)

the black patterned lines act as heat sources with a heat flux equivalent to the local intensity of the lamp, (2) the only source of heat originates from the absorption of light by the printed lines, (3) the bare surface of the Shrinky-Dinks does not absorb light, (4) the initial temperatures for the polymer sheets are the same as the temperatures of the support, and (5) the thermal conductivity and heat capacity of the polymer sheet are those of polystyrene.³⁹ Based on our thermal imaging measurements we define the theoretical onset time required to initiate folding as the instant at which any point on the top surface reaches ≈ 120 °C (*cf.* **Figure S2.2** in supporting information).

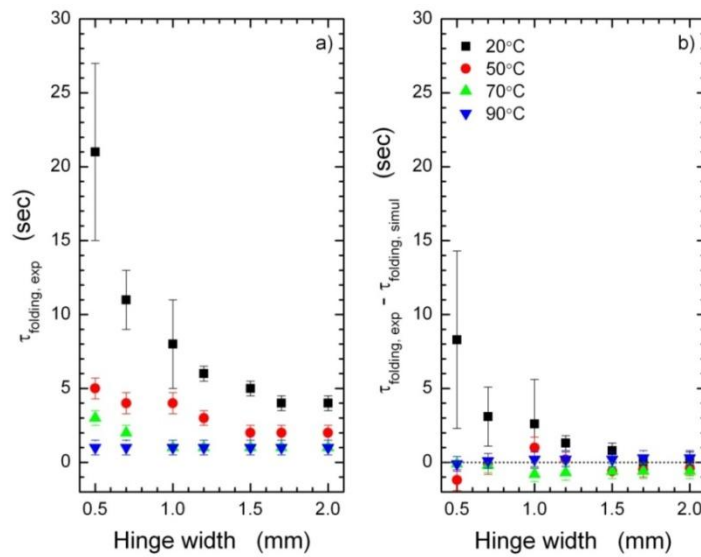


Figure 2.3. a) Experimental time needed to initiate folding ($\tau_{\text{folding,exp}}$) as a function of different patterned line widths and support temperatures and b) Time difference between the experiment and simulation ($\tau_{\text{folding,exp}} - \tau_{\text{folding,simul}}$) needed to initiate folding as a function of different patterned line widths and support temperatures. Shrinky-Dinks (25 mm x 10 mm) feature a single line of ink patterned across the center of the sample. The initial support temperatures (T_s) range from 20 to 90 °C and the widths of the lines vary from 0.5 mm to 2.0 mm.

In **Figure 2.3b** we plot the difference between the experimental and theoretical onset of folding times as a function of the width of the line hinge. It is apparent from the data that the model captures effectively the folding trends measured experimentally at elevated support temperatures (50 ~ 90 °C). This agreement supports the assumptions in the model including the heat fluxes and the threshold surface temperature of the hinge (120 °C) needed for folding to commence. The model is less accurate in describing the onset of folding times in the samples that possess narrow line widths (<1.5 mm) and low T_S values (20 °C). At long onset of folding times, heat can transfer to and from the substrate in ways that are neglected by the model. In addition, heat is transferred radially from the surface of the line to the bulk and the temperature of the polymer near the lines increase as a function of time (*cf.* **Figure S2.4** in supporting information). The polymer sheet is able to dissipate the heat created by light absorption by the narrow lines. It therefore takes more time for the hinges to get warm enough to relax and cause folding at these conditions. During this time, the non-patterned regions of the polymer also heat up due to heat transfer from the lines and the supporting substrate. It is also possible that due to rather slow folding under these conditions we may not observe the initial onset of folding with the naked eye; consequently the observed onset of folding appear longer than predicted theoretically by our model. Regardless of the reasons for the aforementioned small discrepancies, the model and experimental data are in satisfactory agreement to justify thermal flux as the stimulus for folding.

Figure 2.4 compares the simulated temperature profiles of both the top and bottom sides of the polymer sheets with different line widths patterned on the top surfaces of the sheet. The thermal profiles represent snapshots captured when folding begins (i.e., when the

maximum temperature reaches 120 °C). The data are plotted as a function of the two most extreme support temperatures explored in this study (the two top-most plots are at $T_S = 20$ °C and the two bottom-most plots are at $T_S = 90$ °C) and the two most extreme line widths (the two left-most plots have $w = 0.5$ mm and the two right-most plots have $w = 2.0$ mm). Importantly, the temperature at the bottom sides does not exceed T_g as noted by the horizontal dotted line, which is consistent with the observation that only the top faces bearing the ink pattern shrink. If the hinge shrunk uniformly throughout the depth of the film, then the film would likely shrink in-plane or distort, rather than fold.

For a given T_S , the temperature profiles of samples with different line widths show the same temperature peak height but different peak widths. Wider hinges ($w = 2.0$ mm) have more area between the temperature profile (on the top side) and T_g than that for narrower hinges ($w = 0.5$ mm). This result is consistent with intuition; the amount of energy absorbed increases while increasing the width of the printed line hinge. The result is also consistent with observation; the onset of folding time decreases as the width of the printed line hinge increases.

For a given w , the temperature profiles possess similar shapes but different support temperatures. Longer onset times are demonstrated in samples with low support temperature ($T_S = 20$ °C) relative to those with high support temperature ($T_S = 90$ °C), consistent with experimental observations. Moreover, high support temperatures produce profiles with a more significant portion of the sheet above the T_g than those at low support temperatures. Thus, the time difference between different line widths at high support temperatures is smaller than the difference at low support temperatures.

In addition, for a given line width, the temperature profiles spread further outside the line width at lower support temperatures than at higher support temperatures. This results likely in more imperfect folding (i.e., bare regions of the Shrinky-Dinks contract) due to the heating of non-patterned region, as observed experimentally.

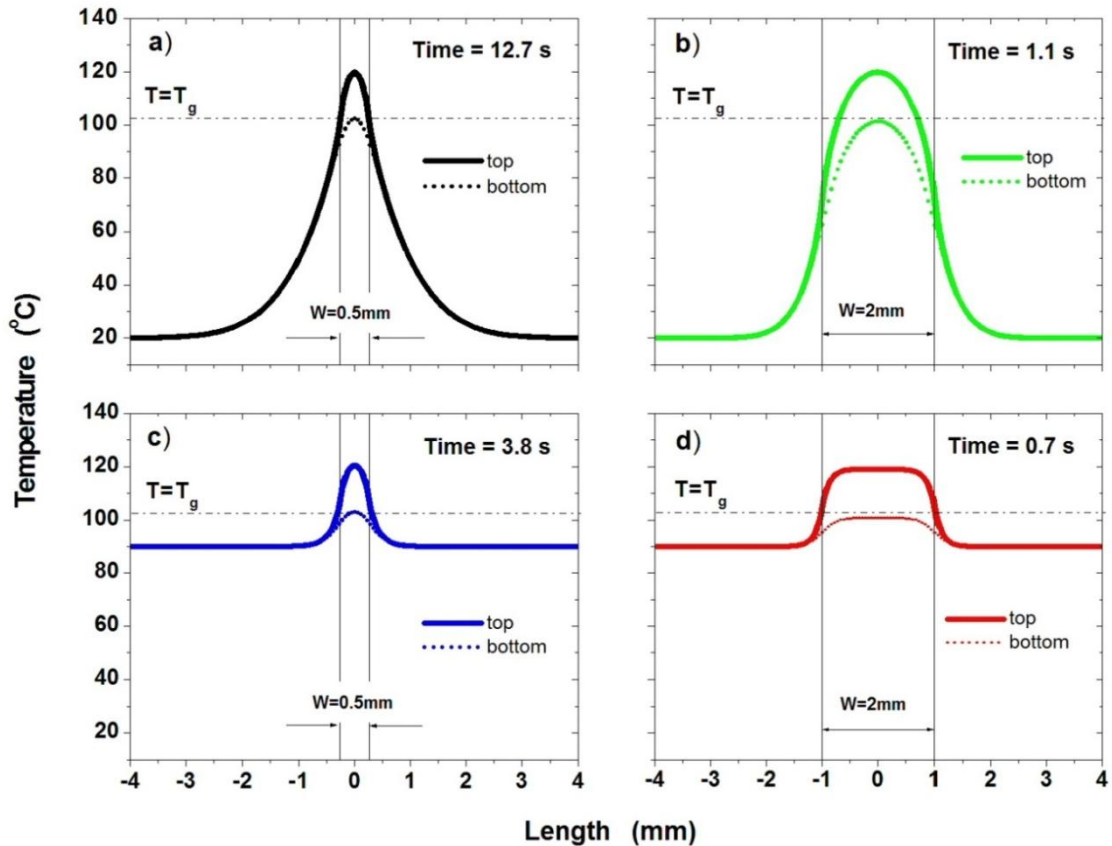


Figure 2.4. Simulated cross-sectional temperature profiles on the top (solid lines) and bottom (dotted lines) sides across the length of Shrinky-Dinks with different line widths ($w = 0.5\text{ mm}$ and $w = 2.0\text{ mm}$) at two different support temperatures ($T_S = 20\text{ °C}$ and $T_S = 90\text{ °C}$). a) $w = 0.5\text{ mm}$, $T_S = 20\text{ °C}$; b) $w = 2.0\text{ mm}$, $T_S = 20\text{ °C}$; c) $w = 0.5\text{ mm}$, $T_S = 90\text{ °C}$; and d) $w = 2.0\text{ mm}$, $T_S = 90\text{ °C}$. Each profile depicts a snap-shot of the temperature near the patterned line when the top central surface first reaches 120 °C . Times listed in each panel indicate response times for onset of folding as determined from the COMSOL simulation.

Besides w and T_S , other parameters may also affect the folding behavior. The folding of the hinged region is similar to a classic bending beam.⁴⁰ Due to the thermal gradient through the thickness of the film, there is also a gradient in strain relaxation. The top of the film, which is hottest, relaxes the fastest and therefore relieves the most strain to induce folding. This asymmetric relaxation is critical for folding. Although our experiments focus on a small set of materials and geometries, based on the proposed mechanism we believe that the folding behavior will depend on factors such as the magnitude of the heat flux, the support temperature, the geometry of the sample (e.g., sheet thickness), the mechanical properties of the polymer (e.g., the amount of stored stress, the time scales of relaxation, and the bending modulus as a function of temperature), and the thermal transport properties. In the current state, the folding is irreversible. The folded shapes, however, can revert back to a flat, shrunken version of the initial 2D sheet by uniformly heating the shapes above T_g as shown in **Figure 2.5**. Further study has demonstrated the availability of folding complex origami shapes by our approach as shown in **Figure 2.6**.

Folding of the polymer film can be also realized by employing a light source with other wavelengths (i.e., 320-500 nm). Although we focused on simple line hinges in this study, other hinge geometries, i.e. circular hinges, can form curvilinear saddle points (cf. **Figure S2.5** in the supporting information). Moreover, lines created by markers (e.g., Sharpie makers and China markers) can also absorb light and induce folding, but toner patterned with a desktop printer offers better control of the geometry of the hinge. The folding also depends on the loads imposed on the facets. We made a crude measurement of the force exerted by the folding process. Specifically, we clipped weights (i.e., small binder clips) on the end of a

sample like the one depicted in **Figure 2.2a** and measured the weight at which it would no longer fold (≈ 2.8 g placed a distance of 1 cm from a hinge with $w = 1$ mm).

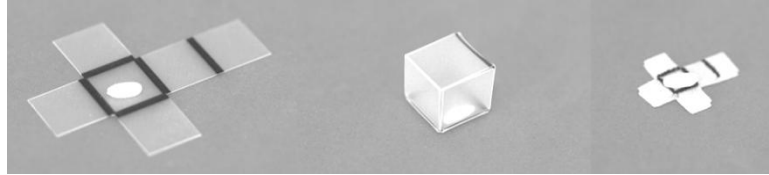


Figure 2.5. Depiction of a folding / unfolding scenario. A grain of rice (left) can be packaged into a self-folded box (center). Uniformly heating the box above the glass transition temperature causes it to unfold and shrink in plane (right).



Figure 2.6. Demonstration of some origami structures induced by self-folding utilizing our approach. The left column shows 2D flat template patterned with black inks as hinges, and the right column shows 3D shapes self-folded when exposing those templates to light. The hinge width is 1.5 mm in these images.

2.4 Conclusion

We demonstrate self-folding of pre-stressed, planar polymer films (Shrink-Dinks) by using local light absorption that heats pre-defined hinges patterned by black toner from a desktop printer. The appeal of our simple approach is the ability to convert 2D patterns into 3D structures using inexpensive materials without the use of complex fabrication steps. We achieve folded structures by choosing an appropriate geometry of the inked pattern, line width and the support temperature. A model based on heat transfer captures effectively the folding trends measured experimentally. Wide hinges fold faster than narrow hinges, which may be useful for creating chronologically synchronized folding. Although we kept light intensity and the light source constant in the experiments, increased light intensity and more focused light should result in faster and more uniform folding; this may be required to achieve the necessary differential heating between the hinge and substrate to miniaturize the process. It may also be possible to induce folding with patterned light rather than patterned hinges. Moreover, inks absorbing heat corresponding to different wavelengths can be applied for self-folding. Other shrink films with different thicknesses and different pre-stresses may provide different scales for 3D structure and folding angles. In the current state, the folding is irreversible. The folded shapes, however, can revert back to a flat, shrunken version of the initial 2D sheet by uniformly heating the shapes above T_g ; this reversion may be useful for packaging and unpackaging of objects.

2.5 Acknowledgements

I thank Ms. Julie Boyles for her work with me to try all preliminary self-folding tests. I thank Dr. Orlin Velev's lab for assistance with the modeling, Kevin A. Ross for measuring the thermal photographs with the IR camera and Dr. Henderson's lab for using the DSC.

References

1. Leong, T.G., A.M. Zarafshar, and D.H. Gracias, *Three-dimensional fabrication at small size scales*. *Small*, 2010. 6(7): p. 792-806.
2. Bassik, N., G.M. Stern, and D.H. Gracias, *Microassembly based on hands free origami with bidirectional curvature*. *Appl. Phys. Lett.*, 2009. 95: p. 091901.
3. Cho, J.H., S. Hu, and D.H. Gracias, *Self-assembly of orthogonal three-axis sensors*. *Appl. Phys. Lett.*, 2008. 93: p. 043505.
4. J. Chen, et al., *Gold nanocases: a novel class of multifunctional nanomaterials for theranostic applications*. *Adv. Funct. Mater.*, 2010. 20: p. 3684-3694.
5. Ye, H., et al., *Remote radio-frequency controlled nanoliter chemistry and chemical delivery on substrates*. *Angewandte Chemie*, 2007. 119: p. 5079-5082.
6. W. Small, I., et al., *Biomedical applications of thermally activated shape memory polymers*. *J. Mater. Chem.*, 2011. 20: p. 3356-3366.
7. Guo, X., et al., *Two- and three-dimensional folding of thin film single-crystalline silicon for photovoltaic power applications*. *PNAS*, 2009. 106(48): p. 20149-20154.
8. Hawkes, E., et al., *Programmable matter by folding*. *PNAS*, 2010. 107: p. 12441-12445.
9. Leong, T.G., et al., *Surface tension-driven self-folding polyhedra*. *Langmuir*, 2007. 23: p. 8747-8751.
10. Tyagi, P., et al., *Self-assembly based on chromium/copper bilayers*. *J. Microelectromech. Syst.*, 2009. 18(4): p. 784-791.
11. Leong, T.G., et al., *Thin film stress driven self-folding of microstructured containers*. *Small*, 2008. 4(10): p. 1605-1609.

12. W.J. Arora, et al., *Membrane folding to achieve three-dimensional nanostructures: nanopatterned silicon nitride folded with stressed chromium hinges*. Appl. Phys. Lett., 2006. 88: p. 053108.
13. J.W. Judy and R.S. Muller, *Magnetically actuated, addressable microstructures*. J. Microelectromech. Syst., 1997. 6: p. 249.
14. Y.W. Yi and C. Liu, *Magnetic actuation of hinged microstructures*. J. Microelectromech. Syst., 1999. 8: p. 10.
15. Y.W. Lu and C.J. Kim, *Microhand for biological applications*. Appl. Phys. Lett., 2006. 89(164101).
16. J. Guan, et al., *Self-folding of three-dimensional hydrogel microstructures*. J. Phys. Chem. B, 2005. 109: p. 23134-23137.
17. Leong, T.G., et al., *Tetherless thermobiochemically actuated microgrippers*. PNAS, 2009. 106(3): p. 703-708.
18. Suzuki, K., et al., *Self-assembly of three dimensional micro mechanisms using thermal shrinkage of polyimide*. Microsyst Technol, 2007. 13: p. 1047-1053.
19. Leng, J., et al., *Electroactive thermoset shape memory polymer nanocomposite filled with nanocarbon powders*. Smart Mater. and Struct., 2009. 18: p. 074003.
20. Leng, J., et al., *Study on the activation of styrene-based shape memory polymer by medium-infrared laser light*. Appl. Phys. Lett., 2010. 96: p. 111905.
21. Lendlein, A., et al., *Light-induced shape -memory polymers*. Nature, 2005. 434: p. 879-882.
22. H. Jiang, S. Kelch, and A. Lendlein, *Polymers move in response to light*. Adv. Mater., 2006. 18: p. 1471-1475.

23. J. Leng, X. Wu, and Y. Liu, *Infrared light-active shape memory polymer filled with nanocarbon particles*. J. Appl. Polym. Sci. , 2009. 114(2455).
24. Lendlein, A. and S. Kelch, *Shape-memory polymers*. Angew. Chem. Int. Ed., 2002. 41: p. 2034-2057.
25. L. Ionov, *Soft microorigami: self-folding polymer films*. Soft Matter, 2011. 7: p. 6786-6791.
26. K.M. Lee, et al., *Light-activated shape memory of glassy, azobenzene liquid crystalline polymer networks*. Soft Matter, 2011. 7: p. 4318-4324.
27. N. Liu, et al., *Formation of micro protrusion arrays atop shape memory polymer*. J. Micromech. Microeng., 2008. 18: p. 027001.
28. Ebefors, T., E. Kälvesten, and G. Stemme, *Dynamic actuation of polyimide v-groove joints by electrical heating*. Sensors and Actuators A, 1998. 67: p. 199-204.
29. Luo, J.K., et al., *Fabrication and characterization of diamond-like carbon/Ni bimorph normally closed microcages*. J. Micromech. Microeng., 2005. 15: p. 1406-1413.
30. Luo, J.K., et al., *Modelling and fabrication of low operation temperature microcages with a polymer/metal/DLC trilayer structure*. Sensors and Actuators A, 2006. 132: p. 346-353.
31. G. Stoychev, N. Puretskiy, and L. Ionov, *Self-folding all-polymer thermoresponsive microcapsules*. Soft Matter, 2011. 7: p. 3277-3279.
32. S. Zakharchenko, et al., *Temperature controlled encapsulation and release using partially biodegradable thermo-magneto-sensitive self-rolling tubes*. Soft Matter, 2011. 6: p. 2633-2636.
33. Pister, K.S.J., et al., *Microfabricated hinges*. Sensors and Actuators A, 1992. 33: p. 249-256.

34. Chen, C.S., et al., *Shrinky-Dink microfluidics: 3D polystyrene chips*. Lab on a Chip, 2008. 8: p. 622-624.
35. Grimes, A., et al., *Shrinky-Dink microfluidics: rapid generation of deep and rounded patterns*. Lab on a Chip, 2008. 8: p. 170-172.
36. P.T. Mather, X. Luo, and I.A. Rousseau, *Shape memory polymer research*. Annu. Rev. Mater. Res., 2009. 39: p. 445-471.
37. Y. Yabu, et al., *Spontaneous formation of microwrinkles on metal microdot arrays by shrinkage of thermal shrinkable substrate*. Applied Materials & Interfaces, 2010. 2(1): p. 23-27.
38. M.H. Lee, et al., *Programmable soft lithography: solvent-assisted nanoscale embossing*. Nano Lett., 2010. 11(2): p. 311-315.
39. Mark, J.E., *Physical properties of polymers handbook*. 2007, New York, USA: Springer.
40. Gere, J.M. and S. Timoshenko, *Mechanics of materials*. 4th ed. 1997, Boston: PWS Pub Co. xvi, 912 p.

Supporting Information

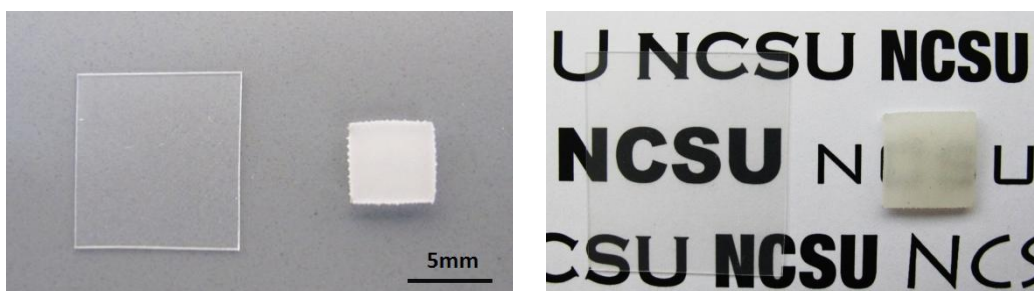


Figure S2.1. Photographs of Shrinky-Dink substrates like those used in this study. (left) A pristine substrate shrinks significantly in plane via uniform heating in the oven at 120 °C. (right) The pristine substrate is slightly hazy prior to shrinking, but transmits light effectively.

Table S2.1. Folding angles as a function of line width patterned across the narrow dimension of a Shrinky-Dink ($L = 25$ mm, $L' = 10$ mm).

Line Width (mm)	Folding Angle (°)
2.0	≈60
1.7	≈75
1.5	≈75
1.2	≈90
1.0	≈90
0.7	≈90
0.5	≈90

Table S2.2. Folding angles for double-line hinges as a function of line spacing on Shrinky-Dinks (25 mm x 10 mm). Two lines (each with a width of 1 mm) were patterned parallel to each other across the center of the sheet with a space placed between the lines.

Line Spacing (mm)	Folding Angle (°)
1	≈45
0.5	≈60
0.3	≈60

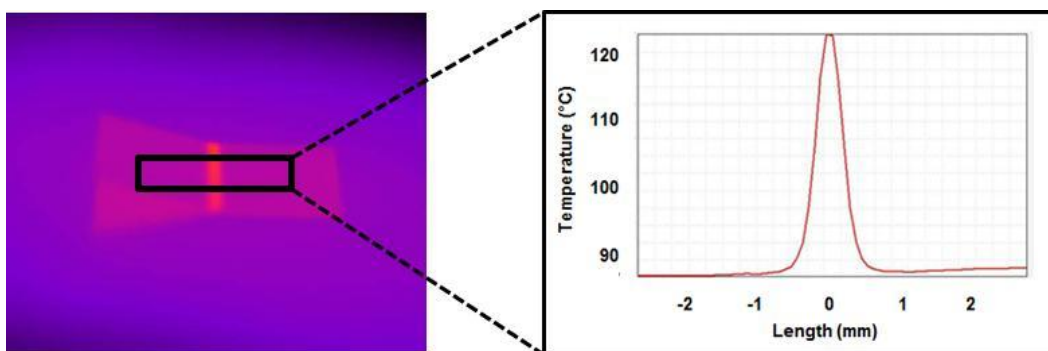


Figure S2.2. Thermal photograph (left) of a Shrinky-Dink ($L = 25$ mm, $L' = 10$ mm) during the folding process taken using an infrared camera and the corresponding temperature profile defined in the black box (right). It is apparent that the film is beginning to fold in this snapshot. In this experiment, the substrate started with a support temperature of ≈ 80 °C prior to irradiation. The temperature is plotted as a function of distance along the axis perpendicular to the hinge. The temperature is largest in the middle of the line and reaches ≈ 120 °C when folding first initiates, yet quickly tapers off to the support temperature, which is important for rapid, selective heating of the hinge.



Figure S2.3. Photograph of a deformed box that is representative of the deformation that occurs to the panels when a sample is over-exposed to the light.

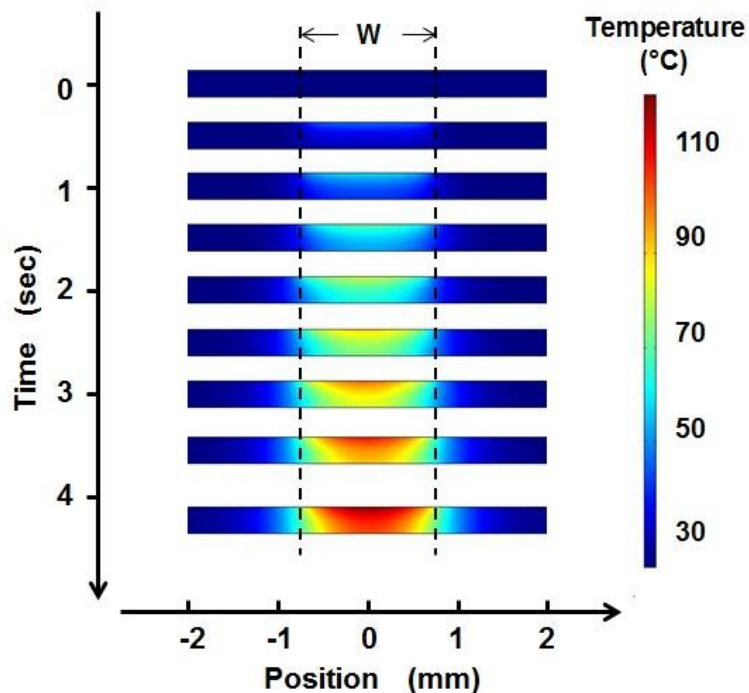


Figure S2.4. Colored maps of the modeled temperature profile in the cross-section of a Shrinky-Dink during the first 4.2 seconds of exposure at $T_s = 20\text{ }^\circ\text{C}$. The heat originates from the top surface, which is the location of the ink. The two vertical dashed lines represents the patterned line width ($w = 1.5\text{ mm}$).

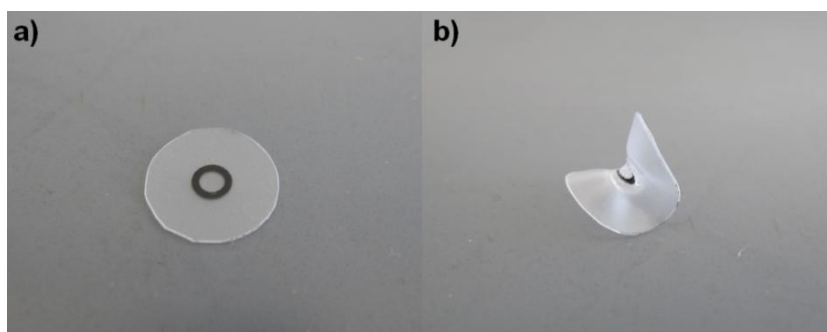


Figure S2.5. Photographs of (a) a 2D Shrinky-Dink (diameter 10 mm) patterned with black toner in the shape of a concentric circle ($w = 1\text{ mm}$, outer diameter 6 mm) and (b) the resulting 3D saddle structure that forms upon exposure to light.

CHAPTER 3

Modeling Self-Folding Kinetics Using Thermal Shrinkage of Pre-Strained Polymer Sheets*

* This chapter is partially based on Y. Liu, R. Mailen, Y. Zhu, M. D. Dickey, J. Genzer. *Advanced Materials Interfaces*, submitted.

3.1 Introduction

This chapter develops a predictive model of the dynamic folding angle of thermally driven self-folding sheets. Self-folding sheets are substrates that fold without human intervention, which is appealing for packaging, assembly, and actuation.¹⁻⁶ Self-folding is typically accomplished by pre-defining hinges in a two-dimensional (2D) substrate that facilitate the formation of three-dimensional (3D) structures.^{1,2} Previously, we demonstrated a simple approach to self-folding by printing black ink (*e.g.*, toner from a desktop printer) as a light absorber on pre-strained polymer sheets, *i.e.*, shrink films, which are shape memory polymers (SMPs) that shrink in plane when heated above their glass temperature, and triggering the folding of the sheet by irradiating it with light.⁷ The inked region, *i.e.*, ink and the polymer underneath the ink, which defines the self-folding ‘hinges’, absorbs light preferentially relative to the rest of the optically transparent sheet. Folding occurs when the inked region gets sufficiently hot to allow the pre-strained polymer sheet to relax directly under the ‘hinge’ in a gradient fashion through the depth of the sheet. The appeal of this approach is its simplicity in converting 2D patterning of inexpensive plastic materials into 3D objects using only light.

We sought to understand and model the folding kinetics, *i.e.*, folding angle as a function of time, which is important for understanding and controlling the self-folding of pre-strained polymer sheets. Constitutive models have been developed previously for amorphous SMPs that incorporate their thermo-mechanical behavior to capture the shape memory effect.⁸⁻¹⁰ These methods require a number of intrinsic material parameters and complex finite element analysis for the prediction of the shape memory effect.^{8, 9, 11-13} Here, we

predict the kinetics of self-folding using macroscopic properties of pre-strained polymer sheets incorporated into a simple geometric model without the need to measure the intrinsic thermo-mechanical properties of the polymer. We measure the time evolution of the macroscopic in-plane sheet shrinkage over a range of constant temperatures and constant heating rates. We then employ these macroscopic measurements to predict both the maximum folding angle and the change of folding angle with time through the use of a simple geometric model of the shrinkage profile across the depth of the ‘hinge’.

3.2 Experimental

A desktop laser printer (HP-P3005dn) produced 2D black ink patterns (designed in CorelDRAW[®]) onto clear inkjet Shrink Film (Grafix[®]). The film thickness is ≈ 0.3 mm, as measured by a caliper. An infrared heat lamp (250 W, Phillips) and a halogen lamp (90 W, Phillips) were used as heating sources. Shrinkage was carried out on a hot stage (Mettler Toledo FP82HT) with the initial temperature of 100 °C. Non-isothermal shrinkage test for high heating rates (>20 °C/min) was carried out on a hot plate (EchoTherm[™] HS30, Torrey Pines Scientific) at the pre-heating temperature of 100 °C. Plain pre-strained PS sheets were used for shrinkage test in the hot stage. Plain sheets coated with black ink were used for non-isothermal shrinkage test under the exposure to IR and halogen lamps. All polymer sheets for shrinkage test had initial dimensions of 20 mm x 20 mm. The dimensions of the polymer sheet in the X and Y directions before and after shrinkage were measured by a caliper. The temperatures of the surface of ink patterned PS sheet and hinge area of the folding sample were measured by IR camera (FLIR A325). The hinge patterned PS sheets were cut into

smaller samples (25 mm x 10 mm). The bending angles of the samples were recorded by video camera (Cannon Vixia HF S20).

3.3 Results and Discussion

Our approach to self-folding relies on the local delivery of external heat to a hinge relative to the rest of the sheet. This localized heating can be accomplished by patterning hinges of black ink from a desktop printer. **Figure 3.1** compares the response to light (an infrared heat lamp, Phillips) of both plain pre-strained polystyrene (PS) sheets (Grafix[®] shrink film, $\approx 122\%$ biaxial pre-strain) and a sheet printed with black ink. The samples rest on a hot plate set to 90 °C, which brings the sheet closer to the glass transition temperature (T_g) of PS. An infrared (IR) camera measures the average temperature of the top surface of the PS sheets as a function of exposure time to the lamp. Absorption of light by the black ink causes the coated PS sheet to heat up and shrink due to strain relaxation. The shrinkage of the pre-strained polymer sheet (S) is defined as:

$$S = \frac{l_0 - l}{l_0} \quad . \quad (3.1)$$

In Equation (3.1), l_0 is the original length of the polymer sheet before strain relaxation upon heating and l is the length of the PS sheet during heating. Shrinkage reaches its maximum value ($\approx 55\%$) over the course of ≈ 10 seconds. In contrast, the plain (*i.e.*, un-inked) PS sheet maintains its original size over the course of 10 seconds of exposure to the IR lamp. The temperature of the polymer increases slightly due to absorption of the longer wavelengths (in the IR region) from the IR lamp, but does not warm up enough to induce measureable shrinkage within the time scale of the experiment. The sheet coated uniformly with black ink

initially curls upwards because the top of the PS sheet is hotter than the bottom and therefore relaxes more rapidly on the inked surface. This behavior is important for understanding how self-folding occurs when the black ink defines a hinge.

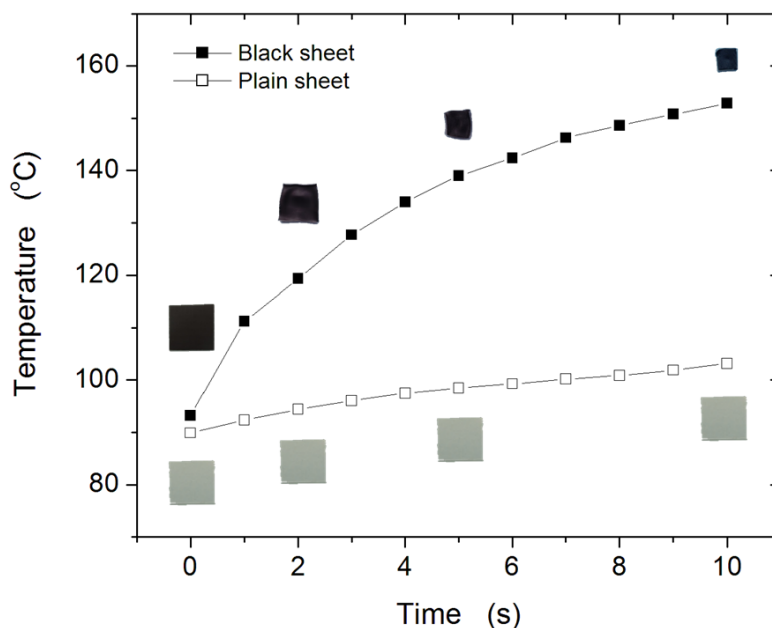


Figure 3.1. Temperature dependence on the exposure time to a heat lamp for a plain pre-strained PS sheet (open symbols) and a pre-strained PS sheet printed with black ink (solid symbols). Photographs of representative black and plain PS sheets depict the geometry for selected data points. Curled samples are flattened for imaging. The PS sheets (initial dimension 20 mm x 20 mm) rest on a hotplate at 90 °C during the exposure to IR light.

Self-folding occurs when the top of the hinge shrinks faster than the bottom of the hinge, which is realized by delivering heat locally and rapidly to the top of the hinge. Folding is ultimately a dynamic process that depends on strain relaxation, and thus, temperature across the film thickness as a function of time. We therefore seek to study the kinetics of shrinkage of pre-strained PS sheets as a function of temperature, time, and heating

rate on a macroscopic scale to ultimately understand the kinetics of folding within the confines of the hinge.

First, we studied the shrinkage behavior of PS sheets under isothermal conditions to investigate the effect of temperature on the kinetics of shrinkage. We measured the shrinkage of PS sheets versus time while holding the temperature constant within a hot stage. **Figure S3.1** (*cf.* Supporting Information) shows the shrinkage of the PS sheets as a function of time in both the horizontal (X) and the vertical (Y) direction of the sheet in portrait view. The shrinkage takes places simultaneously in both X and Y directions especially at high temperatures or high heating rates. Our analysis focuses on the shrinkage performance in one of the directions (say, X).

Figure 3.2 plots the shrinkage data of PS sheets under isothermal conditions as a function of heating time for various temperatures. As expected, the shrinkage rate, *i.e.*, the change of shrinkage with time, increases with increasing temperature. This isothermal shrinkage can be modeled analogously to first-order chemical reaction kinetics:¹⁴

$$S = S_{\infty}[1 - e^{-k_t(\tau - \tau_0)}] \quad . \quad (3.2)$$

In Equation (3.2), S is the shrinkage at time τ ; S_{∞} is defined as the ultimate shrinkage obtained at the plateau of shrinkage on the time scale of our experiments; k_t is the shrinkage rate constant, and τ_0 is the induction time (*i.e.*, the time when the nonzero stress appears¹⁵) under isothermal conditions.¹⁴ The model can be understood intuitively as having a maximum shrinkage rate when the PS strain is the largest and subsequently slowing down as strain (and stress) in the PS sheet relaxes due to shrinkage. The lines in **Figure 3.2** have been

obtained by fitting the experimental data (symbols) to Equation (3.2); the values of the fitting parameters are listed in **Table S3.1** in the Supporting Information.

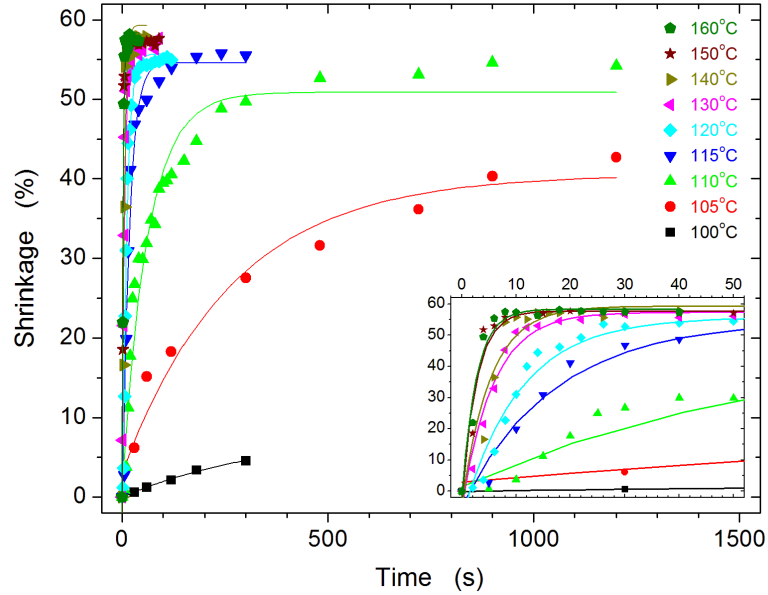


Figure 3.2. Thermal shrinkage of pre-strained PS sheets (initial dimension 20 mm x 20 mm) as a function of heating time at a constant temperature. The symbols represent the experimental data and the lines are best fit curves using Equation (3.2). The inset magnifies the data from 0 to 50 s.

Figure 3.3 shows the relationship between the ultimate shrinkage (S_{∞}) and temperature under isothermal conditions (*cf.* **Figure 3.2**). The ultimate shrinkage increases with increasing temperature and this trend can be fit by Equation (3.3):

$$S_{\infty} = S_m [1 - e^{-k_T(T-T^*)}] \quad . \quad (3.3)$$

In Equation (3.3), S_m , k_T , and T^* are the fitting parameters with the values of 57.8%, 0.204 $^{\circ}\text{C}^{-1}$, and 99.2 $^{\circ}\text{C}$, respectively. The maximum shrinkage for our pre-strained PS sheets,

defined by the amount of pre-strain incurred during the manufacturing process, is $\approx 55\%$. However, within the time scale of our experiments, S_∞ only reaches this plateau when the temperature is at least $115\sim 120\text{ }^\circ\text{C}$, which is consistent with previous measurements.¹⁶ S_∞ is a strong function of temperature in the range between 100 and $120\text{ }^\circ\text{C}$. We ultimately use Equation (3.3) to predict the maximum thermal shrinkage behavior as a function of temperature when $T > T^*$. The reference temperature (T^*) in Equation (3.3) ($99.2\text{ }^\circ\text{C}$) is very close to the T_g ($\approx 103\text{ }^\circ\text{C}$) of PS, as measured by differential scanning calorimetry (DSC).⁷ The reference temperature can be understood as a threshold temperature above which the PS sheet must be heated before shrinkage occurs. It is therefore intuitive that this value should be close to T_g of the PS sheet.

In analogy to activation energy in chemical reactions, the natural logarithm of the shrinkage constant (k_t), derived from isothermal shrinkage experiments (*cf.* **Figure 3.2**), is inversely proportional to the temperature, as governed by the well-known Arrhenius equation. The activation energy of thermal shrinkage can then be obtained from the slope of $\ln(k_t)$ vs. $1/T$. From the data in **Figure 3.3**, the slope for the temperature range between 100 and $110\text{ }^\circ\text{C}$ is much larger than that for the range between 130 and $160\text{ }^\circ\text{C}$. As a result, the activation energy of thermal shrinkage of the PS sheets ($\approx 253\text{ kJ/mol}$) at $100\sim 110\text{ }^\circ\text{C}$ is much higher than that ($\approx 43\text{ kJ/mol}$) at $130\sim 160\text{ }^\circ\text{C}$ with a transition region $\approx 115\sim 120\text{ }^\circ\text{C}$. Thus, significant shrinkage occurs at elevated temperatures due to low activation energy. This result helps explain why the ‘hinges’ in a self-folding sample need to reach $115\sim 120\text{ }^\circ\text{C}$ to achieve self-folding. Self-folding relies on rapid and local delivery of energy to the ‘hinge’ and therefore requires folding to occur quickly before the heat dissipates outside the ‘hinge’

region. Our previous work demonstrated that self-folding of PS sheets occurs when the hinge reaches ≈ 120 °C, which is well above the T_g of the polymer sheet. The critical temperature $\approx 115\sim 120$ °C derived from the present study is thus consistent with this previous observation.⁷ Our estimations for the activation energy of thermal shrinkage are within the reported range of activation energies for oriented PS in the literature,¹² which range from 84¹⁷ to 502 kJ/mol.¹⁸

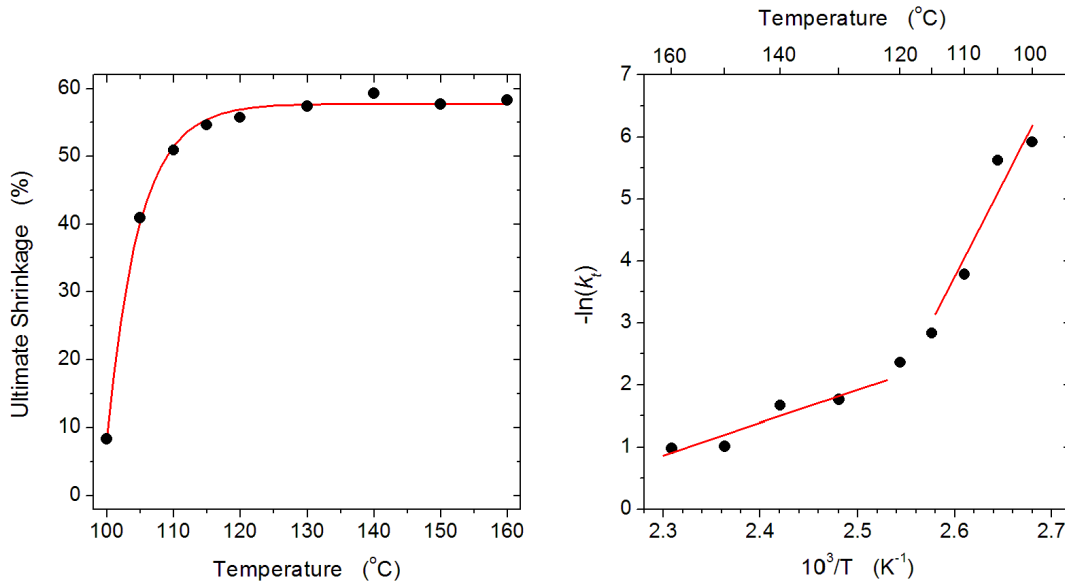


Figure 3.3. (Left) Ultimate shrinkage (S_∞) of PS sheets as a function of temperature during isothermal heating. The line is the best fit to the experimental data using Equation (3.3). (Right) Dependences of the shrinkage constant (k_f) on temperature during isothermal heating. The values of k_f have been obtained by fitting the data in Figure 2 to Equation (3.2). The slopes give activation energy for thermal shrinkage of PS above and below the critical temperature required for self-folding.

We also studied the shrinkage behavior of PS sheets under non-isothermal conditions to investigate the effect of heating rate on sheet shrinkage. Specifically, we measured the

sheet shrinkage as a function of temperature while keeping heating rates constant. We used a hot stage to create a uniform heating environment over a range of heating rates (ranging from 2 to 20 °C/min, the maximum of our hot stage) and measured how the shrinkage of the samples changes with time. We also carried out similar measurements with higher heating rates by using IR and halogen lamps and varied the heating rates by adjusting the distance of the lamp from the PS sheet. We measured the temperature of the PS sheets by an IR camera. The first-order reaction kinetics, given by Equation (3.4), can model the shrinkage kinetics at constant heating rate. This relationship works well except when the shrinkage is small (*e.g.*, the first 1~2 data points when it first starts to shrink at temperatures close to 100 °C).¹⁴

$$S = S_{\infty}[1 - e^{-K(T-T_0)}] \quad (3.4)$$

In Equation (3.4), S is the shrinkage at time τ ($\tau = 0$ corresponds to the time when heating begins); S_{∞} is the ultimate shrinkage; K is the shrinkage rate constant for a constant heating rate and T_0 is the onset temperature for shrinkage. We calculated the corresponding heating rates for the various intensities by averaging the heating rate value over the interval $[0, \tau_{MS}]$, where τ_{MS} is the time needed to achieve maximum shrinkage (*i.e.*, $\approx 55\%$) (*cf.* **Figure S3.3** in Supporting Information).

Figure 3.4 shows several representative shrinkage profiles as a function of temperature for different heating rates in order to express the first-order reaction relationship described in Equation (3.4). **Figure S3.2** in the Supporting Information contains a more comprehensive data set of shrinkage as a function of heating rates. **Table S3.2** in the Supporting Information lists the parameters representing the best fits using Equation (3.4). T_0 depends linearly on the heating rate as shown in **Figure 3.4**. High heating rates, achieved

by exposing the PS sheets to IR light, result in an onset shrink temperature much higher than T_g . This result helps explain an unexpected observation about self-folding. Previously, we observed that self-folding of PS sheets typically occurs when the surface of the hinge reaches $\approx 120\text{ }^\circ\text{C}$ under the exposure of IR light.⁷ The current study implies that the critical temperature ($115\sim 120\text{ }^\circ\text{C}$) for this type of folding in **Figure 3.3** is higher than the T_g of PS. Moreover, the dependency of T_0 in Equation (3.4) on heating rate is analogous to the relationship between T_g and the heating rate in a traditional DSC measurement.¹⁹ The intercept of the best fit line in **Figure 3.4** (*i.e.*, extrapolation to an infinitesimally slow heating rate) yields $\approx 105.5\text{ }^\circ\text{C}$, which is very close to the T_g of PS ($\approx 103\text{ }^\circ\text{C}$). This result is remarkable considering the simplicity of the measurements and the nature of the experiment; *i.e.*, performing macroscopic measurements and extracting molecular information.

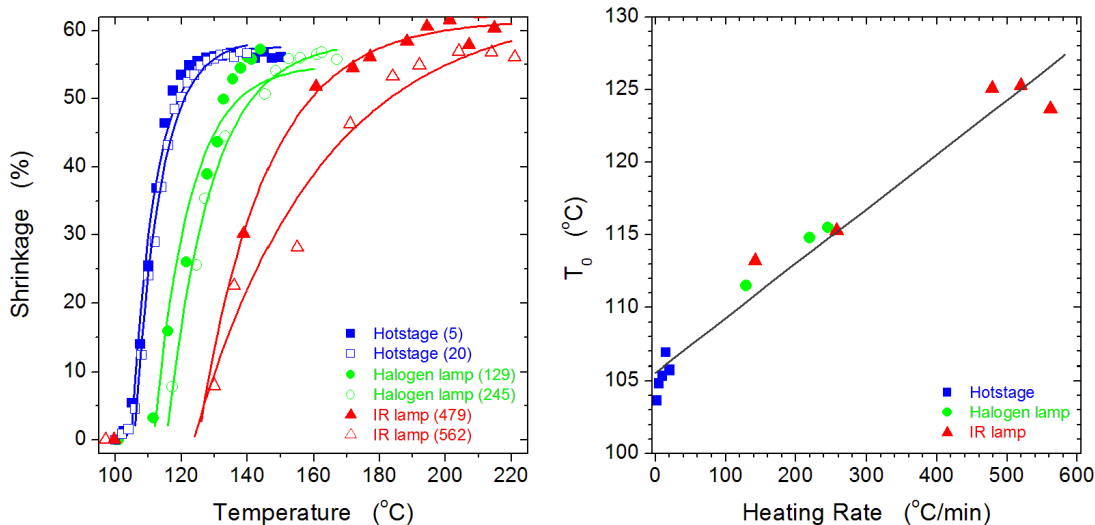


Figure 3.4. (Left) Thermal shrinkage of pre-stained PS sheets (initial dimension 20 mm x 20 mm) as a function of temperature during constant heating rate. A wide range of heating rates is realized by using a hot stage (squares), halogen lamp (circles), and IR lamp (triangles), respectively. The numbers in parentheses denote different heating rates (°C/min). The lines are best fits to Equation (3.4). (Right) Dependence of T_0 derived from the equation on the heating rates. The line is a guide to the eye.

The study of in-plane shrinkage kinetics of PS sheets under both isothermal and non-isothermal conditions (*cf.* **Figure 3.1-3.4**) helps explain the existence of a critical temperature for self-folding (≈ 120 °C for the PS sheets used in this study) and provides an estimate of T_g . The following sections correlate the macroscopic strain relaxation of the PS sheets as a function of temperature, time, and heating rate to the kinetics of folding and the folding angle for various hinge widths (*cf.* **Figure 3.5-3.6**). Specifically, we present a simple geometric model based on the differential shrinkages between the top surface of the hinge, *i.e.*, immediately below the black ink, and the bottom side of the PS sheet to predict the maximum folding angle and dynamic folding angle as a function of hinge width.

First, we predict successfully the maximum folding angle by using a simple geometric model. In our previous work we showed that during folding, the temperature on the bottom side of the PS sheet does not exceed T_g while the temperature on the top surface (the ink) reaches the critical temperature of ≈ 120 °C for folding.⁷ Ultimately, with prolonged exposure to light the PS sheets will unfold, which implies that the bottom side of the PS sheet eventually shrinks due to increased temperature. For simplicity, we assume that the folding reaches the maximum bending angle when the top surface achieves the maximum shrinkage ($\approx 55\%$) while the bottom side of the PS sheet does not shrink. The model assumes a linear shrinkage gradient across the PS film thickness (H). We record the maximum bending angle, α_B , *i.e.*, the angular displacement of the fold, which is complementary to folding angle. The predicted maximum α_B agrees well with the experimental data. The value of α_B can be calculated from Equation (3.5) as:

$$\alpha_B = 180^\circ - 2 * \tan^{-1}\left(\frac{2*H}{W*S}\right) \quad . \quad (3.5)$$

In Equation (3.5), W is the hinge width, H is the film thickness, and S is the maximum shrinkage of the PS sheet ($\approx 55\%$) as indicated in **Figure 3.5**.

The calculated α_B derived from the geometric model matches well with the experimental bending angle especially in the median range of hinge widths. The discrepancy at narrow hinge widths (≈ 0.5 mm) is likely due to the heat dissipation outside of the hinge region during the long exposure time to the light source required to induce folding. The discrepancy at wide hinge widths (1.5~2.0 mm) may be due to the fact that the folded PS ‘panel’ blocks incoming light when $\alpha_B > 90^\circ$ and therefore the light does not reach the

printed hinge. Consequently, the experimental α_B value for wider hinges plateaus close to 90° and is thus lower than that predicted by the model. This model fits the experiment well when exposing to light sources at high heating rates (*e.g.*, IR light heating shown in **Figure 3.4**). At low heating rate, however, the heat dissipates outside the hinged region and the shrinkage on the bottom side cannot be neglected (*cf.* **Figure S3.4** in Supporting Information), which results in smaller α_B than that predicted from the model. The dissipation of heat also causes the PS sheet to distort outside of the hinge. This underestimation of α_B at low heating rate by the model justifies the assumption for the geometric model that the maximum bending angle occurs when the top surface achieves the maximum shrinkage ($\approx 55\%$) while the bottom side of the sheet does not shrink. Therefore heat has to be delivered locally and rapidly to realize self-folding and fulfill the assumption of the geometric model.

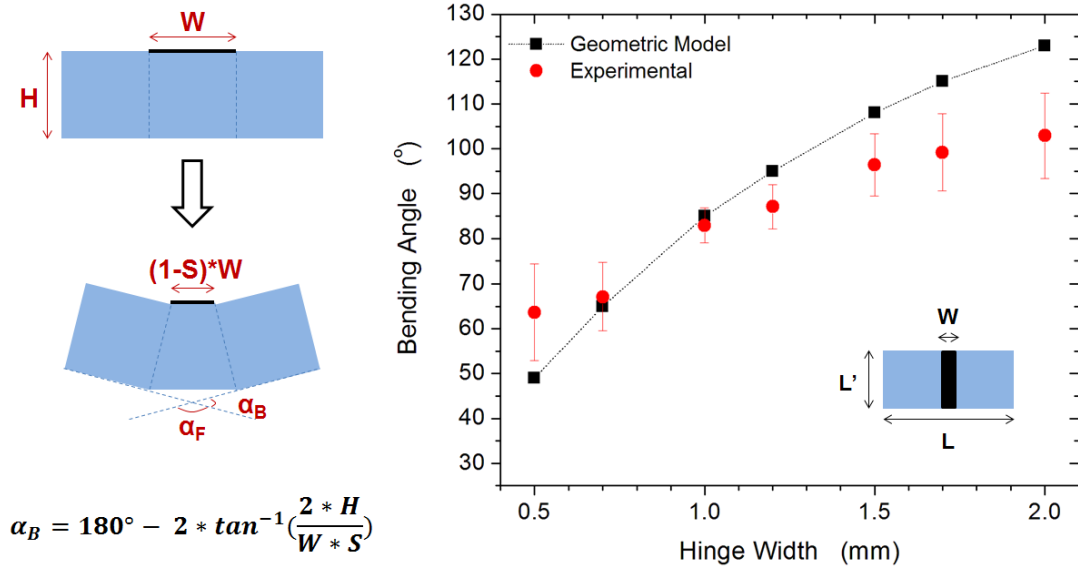


Figure 3.5. (Left) Side-view schematic of the polymer sheet (blue) and ink (black) depicting the simple geometrical model used to calculate the bending angle. (Right) Bending angles (α_B) as a function of hinge width obtained from experiment (circles) and calculated using the geometric model (squares). Experimental data were collected from pre-stained PS sheets as depicted in top-view schematic (initial dimension 25 mm x 10 mm) with a single line of ink patterned across the center of the sample resting on hotplate at 90 °C and exposed to external IR light at a distance of 5 cm.

This simple geometric model not only estimates the maximum angle well, but also predicts successfully the change in α_B with time for different hinge widths. We measured the temperature of the hinges (T_h) during folding as a function of time by an IR camera and found that the surface temperature rises quickly in the initial 2~3 seconds of exposure to the IR light for all hinge widths and then plateaus (120~130 °C) (*cf.* **Figure 3.6**) despite the constant flux ($\approx 1 \text{ W cm}^{-2}$) of energy from the lamp placed at a distance of 5 cm from the sample to achieve a high heating rate.⁷ This plateau may be due to steady state heat dissipation, decreased area for light absorption due to the shrinkage of the inked region on

the PS sheet, or the simultaneous increase of mass near the hinge due to accumulation of shrunken material. Based on this temperature profile, the shrinkage performance of the hinge area for folding can be divided into two stages: 1) non-isothermal shrinkage under the constant heating rate of the light before reaching the plateau (first 2~3 seconds of exposure to light), and 2) isothermal shrinkage for the remaining light exposure. Thus, predicting the shrinkage of the hinge associated with this thermal profile requires information from both the isothermal and constant heating models by convoluting the temperature and time profile in Equations (3.2) and (3.4), respectively, while assuming the bottom of the hinge does not shrink.

The calculated α_B obtained by combining the isothermal and non-isothermal shrinkage models in conjunction with the simple geometric model of folding agree very well with the measured α_B values for different hinge widths (*cf.* the right column of **Figure 3.6**). The change of α_B occurs rapidly in the first 2~3 seconds, which also verifies that self-folding relies on rapid heat delivery on the hinge region. This model underestimates α_B for the narrowest hinges ($W = 1.0$ mm). This discrepancy is likely due to the relatively large heat dissipation at the hinge boundaries and the low resolution of the IR camera. Nevertheless, the results in **Figure 3.6** suggest that measuring the surface temperature of the pre-strained PS sheet at the hinge as a function of time provides sufficient information to calculate the folding angle as a function of time if the macroscopic strain relaxation properties of the polymer sheet are known. The model also confirms that wider hinges lead to larger degrees of folding since there is greater strain relaxation at the hinge.

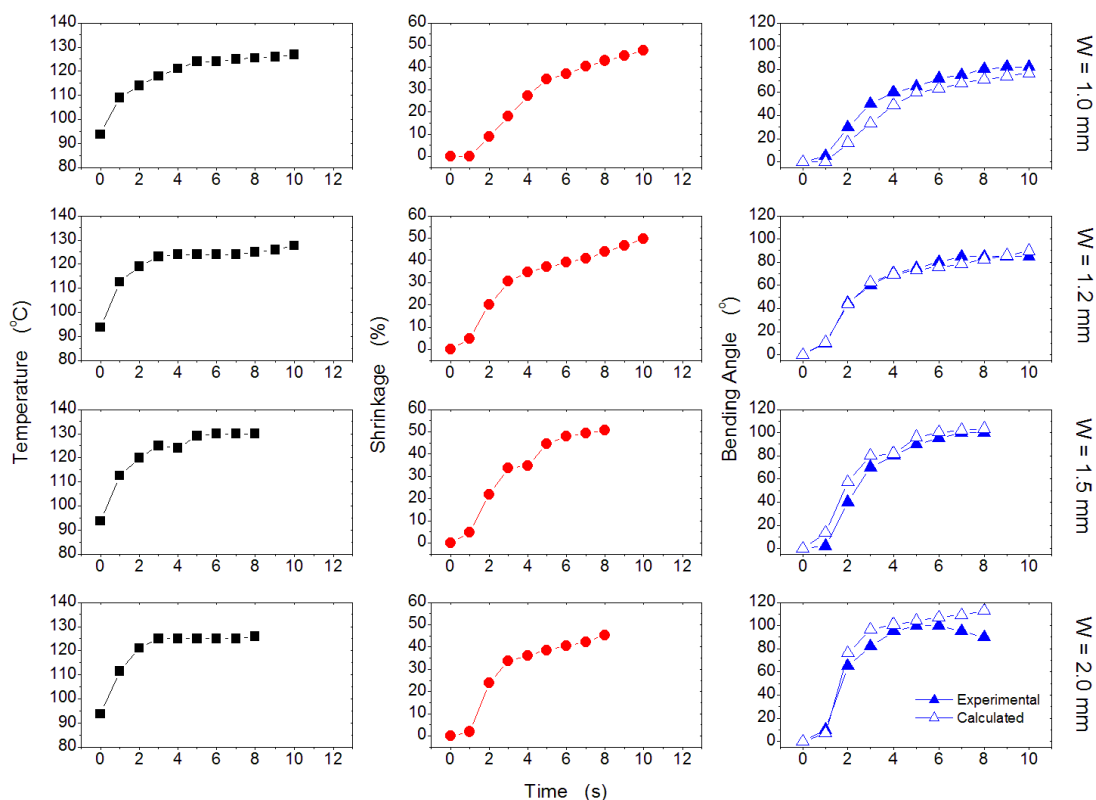


Figure 3.6. (Left column) Temperature of the inked hinge, T_h (solid squares) measured by IR camera. (Middle column) Thermal shrinkages of the PS sheets on the top surface (solid circles) derived from the temperature temporal profile. (Right column) Experimental bending angle change with time (solid triangles) compared with bending angle calculated based on the thermal shrinkage derived from the temperature temporal profile (open triangles). The different rows correspond to data with different hinge widths, W , equal to (from top to the bottom): 1.0, 1.2, 1.5, and 2.0 mm.

3.4 Conclusion

This work offers a simple model to predict successfully the kinetics of self-folding of pre-strained polymer (*i.e.*, PS) sheets as a function of hinge width when the heat is delivered rapidly and locally to the hinge. To develop the model, we studied the thermal shrinkage of these pre-strained PS sheets under two separate thermal conditions: 1) constant temperature,

and 2) constant heating rate. We measured and modeled the resulting macroscopic shrinkage behaviors of these PS sheets and used the resulting information to predict the folding dynamics using a simple geometric model. The appeal of this work is that it predicts accurately the angle of self-folding *vs.* time by simply measuring the thermal profile of the hinge with time and applying a simple model without the need for finite element analysis nor the measurement of the intrinsic thermo-mechanical properties of the polymer.

There are several important findings from the study relevant to thermal shrinkage of pre-strained polymer sheets. The increase of shrinkage with time at constant temperature or at constant heating rate follows a relationship typically found in the first-order reaction kinetics. Significant shrinkage takes place at elevated temperatures (>120 °C for the pre-strained PS sheets investigated here) due to the lowered activation energy of thermal shrinkage. This is consistent with the fact that self-folding in pre-strained PS sheets occurs at temperatures 115~120 °C, which is well above T_g of PS. These high temperatures ensure that the polymer folds rapidly before heat dissipates outside the hinged region. In addition, extrapolation of the onset temperatures obtained at different heating down to “zero” heating rate provides a macroscopic estimate of T_g of the polymer sheet.

Experiments involving self-folding help elucidate the heat management and strain relaxation in pre-strained polymer sheets heated above the glass transition of the polymer. To that end, we established that the folding follows a two-step process. Specifically, sheet relaxation is initiated by non-isothermal shrinkage that takes place under constant heating rates. Shortly thereafter (2~3 seconds in our case), this first stage is followed by isothermal shrinkage which relaxes the strain completely from the sheet.

In spite of its simplicity, the model predicts successfully the experimentally measured folding angles as a function of the hinge width. We note that although we only work with polymer sheets having constant thickness, degree of pre-strain, and chemical composition, the model we have developed should be applicable to sheets featuring other pre-strained polymers, in which the aforementioned attributes vary. In developing the model, we assumed that the strain profile across the film changes linearly with thickness and that the thickness is uniform. As we will show elsewhere,²⁰ a more complex model involving temperature- and frequency-dependent dynamic mechanical measurement incorporated into a finite element analysis can be built to offer a more detailed insight into the strain relaxation through the film. Overall, this work offers a set of necessary guidelines for localized heat management in pre-strained polymer sheets that facilitates pre-programmed sheet folding by a desired angle.

3.5 Acknowledgements

I thank Russell Mailen for his co-work to help understanding thermo-mechanical properties of pre-strained polymer sheet and developing the finite element model so that we can better understand the strain relaxation through the film. I thank Christina Tang for her training and help for the use of rheometer in Dr. Saad Khan's lab.

References

1. Leong, T. G., Zarafshar, A. M. & Gracias, D. H. Three-Dimensional Fabrication at Small Size Scales. *Small* **6**, 792–806 (2010).
2. Ionov, L. Soft microorigami: self-folding polymer films. *Soft Matter* **7**, 6786–6791 (2011).
3. Fernandes, R. & Gracias, D. H. Self-folding polymeric containers for encapsulation and delivery of drugs. *Adv. Drug Deliv. Rev.* **64**, 1579–1589 (2012).
4. Hawkes, E. *et al.* Programmable matter by folding. *Proc. Natl. Acad. Sci.* **107**, 12441–12445 (2010).
5. Small, IV, W., Singhal, P., Wilson, T. S. & Maitland, D. J. Biomedical applications of thermally activated shape memory polymers. *J. Mater. Chem.* **20**, 3356–3366 (2010).
6. Stoychev, G., Puretskiy, N. & Ionov, L. Self-folding all-polymer thermoresponsive microcapsules. *Soft Matter* **7**, 3277–3279 (2011).
7. Liu, Y., Boyles, J. K., Genzer, J. & Dickey, M. D. Self-folding of polymer sheets using local light absorption. *Soft Matter* **8**, 1764–1769 (2012).
8. Nguyen, T., Qi, H. J., Castro, F. & Long, K. A thermoviscoelastic model for amorphous shape memory polymers: Incorporating structural and stress relaxation. *J. Mech. Phys. Solids* **56**, 2792–2814 (2008).
9. Ge, Q., Yu, K., Ding, Y. & Qi, H. J. Prediction of temperature-dependent free recovery behaviors of amorphous shape memory polymers. *Soft Matter* **8**, 11098–11105 (2012).
10. Diani, J., Gilormini, P., Frédy, C. & Rousseau, I. Predicting thermal shape memory of crosslinked polymer networks from linear viscoelasticity. *Int. J. Solids Struct.* **49**, 793–799 (2012).

11. Nguyen, T. D. Modeling Shape-Memory Behavior of Polymers. *Polym. Rev.* **53**, 130–152 (2013).
12. Trznadel, M. & Kryszewski, M. Thermal Shrinkage Of Oriented Polymers. *J. Macromol. Sci. Part C Polym. Rev.* **32**, 259–300 (1992).
13. T. Pakula, M. T. Thermally stimulated shrinkage forces in oriented polymers: 1. Temperature dependence. *Polymer* **26**, 1011–1018 (1985).
14. Shih, W. K. Shrinkage modeling of polyester shrink film. *Polym. Eng. Sci.* **34**, 1121–1128 (1994).
15. Trznadel, M. Thermally stimulated shrinkage forces in oriented polymers: Induction time. *Polymer* **27**, 871–876 (1986).
16. Chen, C.-S. *et al.* Shrinky-Dink microfluidics: 3D polystyrene chips. *Lab. Chip* **8**, 622–624 (2008).
17. Kimmel, R. M. & Uhlmann, D. R. Effects of Pressure on Amorphous Polymers. III. Thermodynamic Properties of Densified Polymethyl Methacrylate. *J. Appl. Phys.* **42**, 4917–4925 (1971).
18. Chang, B. T. A. & Li, J. C. M. Recovery of compressive strain in atactic polystyrene. *J. Mater. Sci.* **16**, 889–899 (1981).
19. Wunderlich, B. *Thermal Analysis of Polymeric Materials*. (Springer Verlag, 2005).
20. Mailen, R., Liu, Y., Dickey, M.D.; Genzer, J., Zhu, Y. in preparation.

Supporting Information

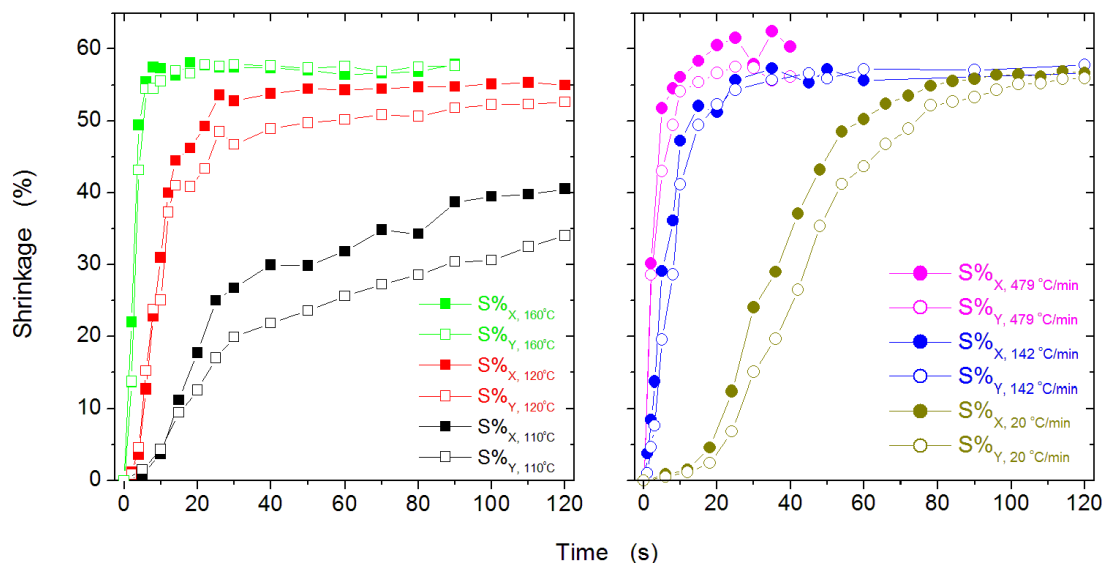


Figure S3.1. (Left) Representative in-plane shrinkage of the pre-stained PS sheets in both X and Y directions with time at a constant temperature of 110, 120 and 160 °C. The experiment is operated in a hot stage at constant temperatures. (Right) Representative in-plane shrinkage of the pre-stained PS sheets in both X and Y directions with time at a constant heating under the exposure to IR light (479 °C/min and 142 °C/min) and in the hot stage (20 °C/min). All samples (initial dimension 20 mm x 20 mm) rest on a hotplate at 100 °C or with the initial temperature at 100 °C in the hot stage.

Table S3.1. Parameters of the exponential fitted curves using Equation (3.2): $S = S_{\infty}[1 - e^{-k_t(\tau-\tau_0)}]$, in different isothermal conditions for the isothermal shrinkage of pre-strained sheets.

Temperature (°C)	S_{∞} (%)	τ_0 (s)	k_t (s ⁻¹)
160	58.3	0.10	0.373
150	57.7	0.12	0.363
140	59.3	0.32	0.189
130	57.4	0.48	0.171
120	55.7	1.46	0.095
115	54.6	1.40	0.059
110	50.9	-1.82	0.016
105	40.9	-22.62	0.004
100	8.4	1.62	0.003

Table S3.2. Parameters of the exponential fitted curves using Equation (3.4): $S = S_{\infty}[1 - e^{-K(T-T_0)}]$, at different heating rates for the non-isothermal shrinkage of pre-strained PS sheets.

Rate (°C/min)	S_{∞} (%)	T_0 (°C)	K (°C ⁻¹)
2	57.9	103.6	0.160
5	56.9	106.1	0.179
10	58.3	105.3	0.121
15	57.7	106.9	0.132
20	58.7	105.7	0.125
220 (Halogen 5cm)	57.7	114.8	0.096
245 (Halogen 10cm)	58.4	115.5	0.074
129 (Halogen 15cm)	55*	111.6	0.092
479 (IR 5cm)	61.6	125.1	0.049
562 (IR 7.5cm)	63.7	123.7	0.026
519 (IR 10cm)	59.1	125.3	0.053
258 (IR 12.5cm)	56.4	115.3	0.079
142 (IR 15cm)	55*	113.1	0.069

* $S_{\infty} = 55\%$ is fixed for the fitting.

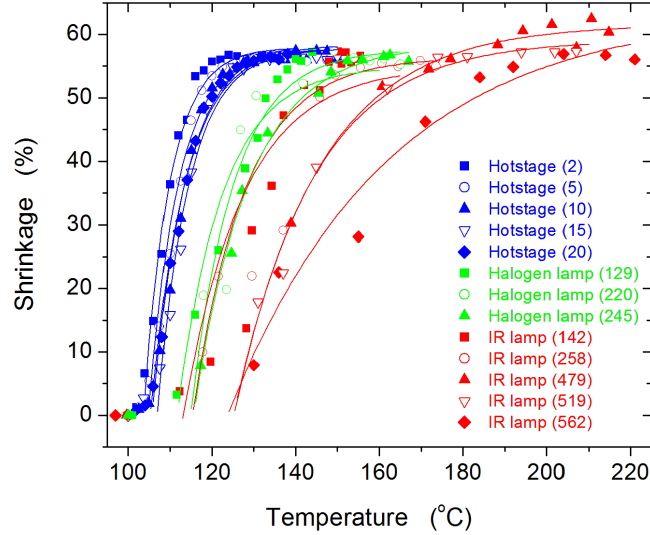


Figure S3.2. Thermal shrinkage of the pre-stained PS sheets (initial dimension 20 mm x 20 mm) as a function of temperature during constant heating rate. Experimental shrinkage data are realized by using hot stage (blue), halogen lamp (green), and IR lamp (red), respectively. The numbers in the parentheses denote different heating rates (in °C/min). The lines are best fits to Equation (3.4): $S = S_{\infty}[1 - e^{-K(T-T_0)}]$.

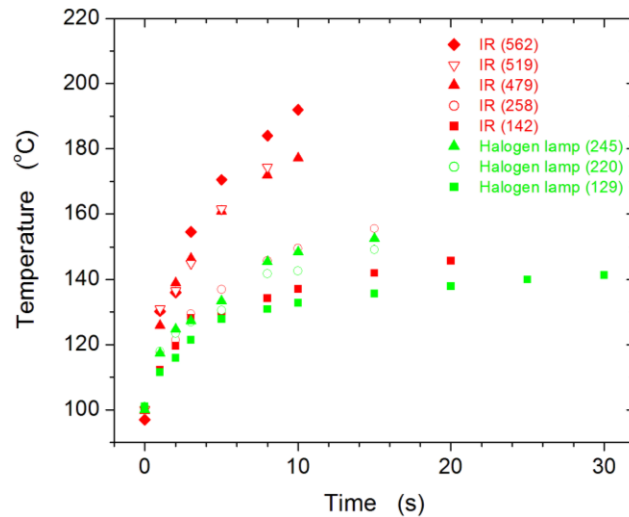


Figure S3.3. Temperature of ink patterned pre-stained PS sheets as a function of time. Experimental data are realized by using halogen lamp (green) and IR lamp (red). The numbers in the parentheses denote different heating rates (in °C/min), which are realized by varying the distance between the lamp to the sample. All samples (initial dimension 10 mm x 10 mm) rest on a hotplate at 90 °C during the light exposure.

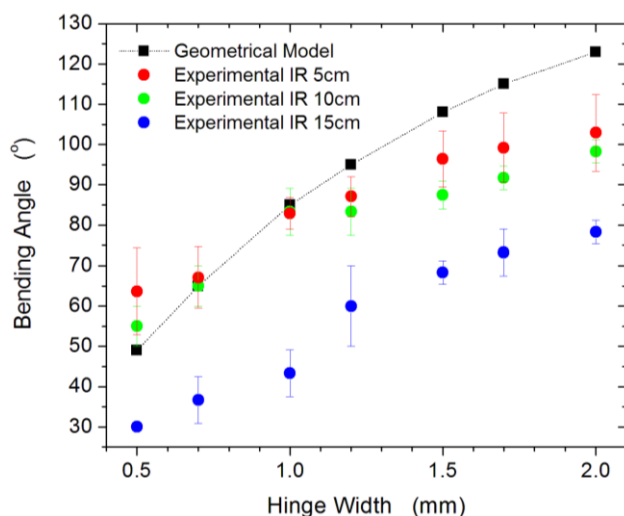


Figure S3.4. Bending angles (α_B) as a function of hinge width obtained from experiment (circles) and calculated using the geometrical model (squares). Experiment data were collected from pre-strained PS sheets (initial dimension 10 mm x 25 mm) with a single line of ink patterned across the center of the sample resting on hotplate at 90 °C and exposed to external IR light at various distances (5, 10, and 15 cm).

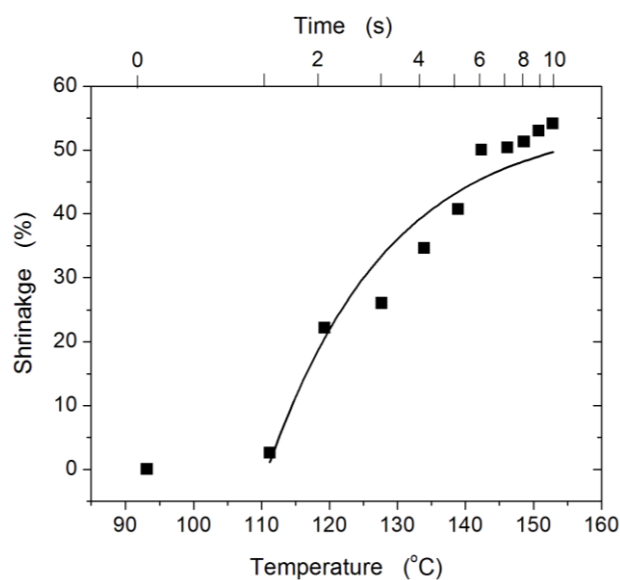


Figure S3.5. Thermal shrinkage of black ink patterned pre-strained PS sheets (initial dimension 20 mm x 20 mm) as a function of temperature under the IR lamp exposure at the distance of 5 cm from the sample. The line represents the best fit to Equation (3.4): $S = S_\infty [1 - e^{-K(T-T_0)}]$. $S_\infty \approx 55\%$ is assumed. The samples are rested on the hotplate at 90 °C.

CHAPTER 4

3D Folding of Pre-Strained Polymer Sheets *via* Laser Light

4.1 Introduction

This chapter describes the use of a laser light to induce rapid folding of planar, pre-strained polymer sheets into three-dimensional (3D) shapes. Folding is an attractive method to convert two-dimensional (2D) substrates into 3D structures for applications including actuators, sensors, and reconfigurable devices.¹⁻⁶

Self-folding is typically accomplished by pre-defining hinges in a 2D substrate that facilitate the formation of 3D structures. To induce folding, a hinge typically differs from the rest of the sheet in composition, property, or layout and responds to some external stimuli (e.g., heat, light, surface tension).^{2,7-11} Light is a particularly attractive stimulus to induce folding because it can be delivered remotely and efficiently and locally; i.e., it can be focused, manipulated, or patterned to deliver energy to only the hinged regions on the sheet. Uniform irradiation (i.e., non-patterned light) has been used previously to induce folding by remotely delivering thermal energy to a hinge. Examples include patterned light absorbers on a uniform pre-strained polymer sheet¹² or patterned hinges that absorb light.^{13,14}

In our approach, the absorbance of light by a uniform coating of black ink on the pre-strained substrate causes the polymer beneath the ink to heat and relax gradually across the sheet thickness and thus induce folding via localized shrinking. This approach has many advantages. First, it requires zero pre-processing steps (i.e., no patterning or lithography), but induces folding in a homogeneous sheet without pre-defined hinges. Second, the location of the folds can be programmed arbitrarily by changing the locus of irradiation by the laser pattern on the 2D sheet. Third, each fold is actuated independently, which satisfies the requirement of sequential folding. Forth, the folding is scalable and compatible with high

throughput manufacturing. Last, the laser delivers controlled amounts of energy to well-defined areas, which provides opportunities to study the fundamental folding response as a function of beam power, intensity and width. In addition to providing quantitative information about folding time and final folding angle, this approach provides insight into the heat dissipation of the substrates and hence the threshold power required to induce folding. Here, we describe the process of self-folding induced by irradiation of pre-strained polymer sheets with laser light and characterize and analyze the role of power and beam width on the time to fold and the folding angle.

4.2 Experimental

The beam width is defined as the Gaussian diameter of the light source in the vertical direction. The beam width is calculated based on optical lengths in the study of important process parameters, while it is measured by a beam profiler (Thorlabs, BP 104-UV beam profiler) in the study of folding mechanism. Power intensity is calculated as the ratio of power measured at the spot of the sample over the laser exposure area on the sample (i.e., sample width multiplies by beam width). The ink coating faces the laser radiation in all cases shown here, however, the folding can be still induced when the ink coating is back to the laser radiation.

4.3 Results and Discussion

Our experiments are based on a continuous wave 1046 nm Nd:YAG laser that is focused to a line using a cylindrical lens. While other beam shapes are possible, the line shape results in a

single, straight hinge produced in the polymer film that is easy to observe and characterize. To achieve different beam widths i.e., the dimension of beam parallel to the long axis of the sample, the position of the sample is moved relative to the beam focus. The polymer underneath the irradiated region heats and shrinks locally to cause folding of a flat sheet into a 90 degree fold within a few seconds (*cf.* **Figure 4.1**). Black ink coated on the pre-strained polymer sheets (Grafix[®] Clear Inkjet Printable Shrink Film, ≈ 0.3 mm thick, contract in-plan biaxially by $\sim 55\%$) coated with black ink absorbs 90% of incident light based on UV-Vis measurements, and almost all incident light ($\sim 95\%$) at 1064 nm specifically (*cf.* **Figure S4.1** in Supporting Information).

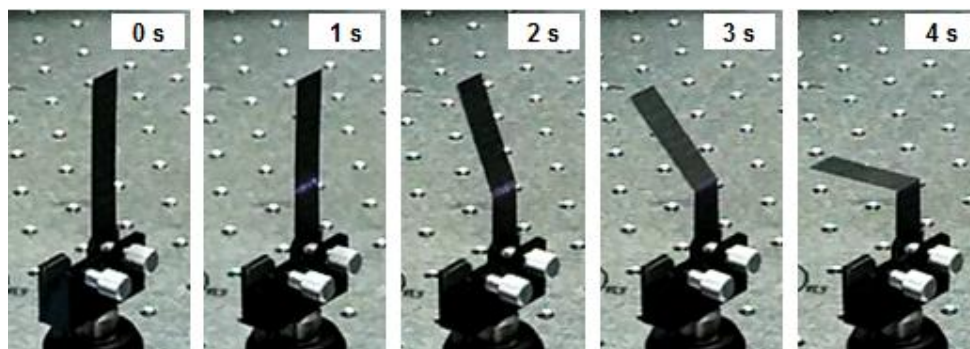


Figure 4.1. Photographs of the folding of a pre-strained polymer sheet coated with black ink triggered by IR laser light. The sample is 10 mm x 50 mm and is irradiated with a laser beam that spans the width of the sample and irradiates from the left side of the images. The beam, though not visible to the naked eye, can be clearly seen in the captured images impinging on the sample at times 1 and 2 s. The sample is held in place at the bottom by a clamp supported by a laser table.

All tests in this work were done with samples that were cut into striped, which had width of 4 mm. The parameters we varied directly were the beam power (in mW) and beam

width (in μm), and indirectly the beam intensity (in W/cm^2). We studied the effect of these key process parameters on the bending angle and folding time. We define the ‘bending angle’, α_B , as the angular displacement of the fold, while ‘folding angle’ is the angle between two adjacent facets on the inked side of the hinge. We measure ‘bending angle’ in the discussion here. We define ‘onset of folding’ as the time the substrate is exposed to light before it first starts folding. Although we choose onset time as a key metric, we note that short onset time corresponds to short total time of folding (the time required to get to the final bending angle) (*cf.* **Figure S4.2** in Supporting Information).

Figure 4.2 shows three regions for the folding: no-folding, transitional region, and 90° folding. We varied the absorbed incident laser power (50~150 mW) and the beam widths (0.5 ~ 1.7 mm). In the experiments, the hinge angle was measured after the sample had been exposed to the laser beam for 2 min; this allowed for any folding processes to complete fully. The onset time was measured using a stopwatch.

As seen in **Figure 4.2**, folding occurs above a power threshold (~ 60 mW). As expected, increasing the power decreases the onset time and increases the bending angle. The bending angle plateaus at 90° because the folded ‘panels’ of the polymer sheet eventually folds into the path of the incident beam, preventing further heating of the hinge. Although we found that the sample can fold $> 90^\circ$ by changing the incident angle of the laser, we only investigated the folding performance when the laser was normally incident to the sample.

We observed that narrower beams require lower powers (mW) for a given onset time of folding (or a given bending angle) as shown in **Figure 4.2a, b** because of smaller

footprint. Once power is normalized by the footprint of the irradiated light (i.e., power intensity, W/cm^2), then narrower beams required larger power densities than the wider beams (for a given onset time or bending angle), as shown in **Figure 4.2c, d**. The bending angle and onset time data collected for multiple beam widths do not collapse onto respective unique master plots, however, when plotted as a function of power intensity. Visually, it appears, however, that large deviations occur in samples with narrower hinge widths while specimens with larger hinge widths tend to form universal curves in both bending angle and onset time data. We speculate that narrower beams lose a more significant amount of energy to the edges (of the irradiated region) and therefore require a higher incident intensity to achieve the same response as a wider beam.

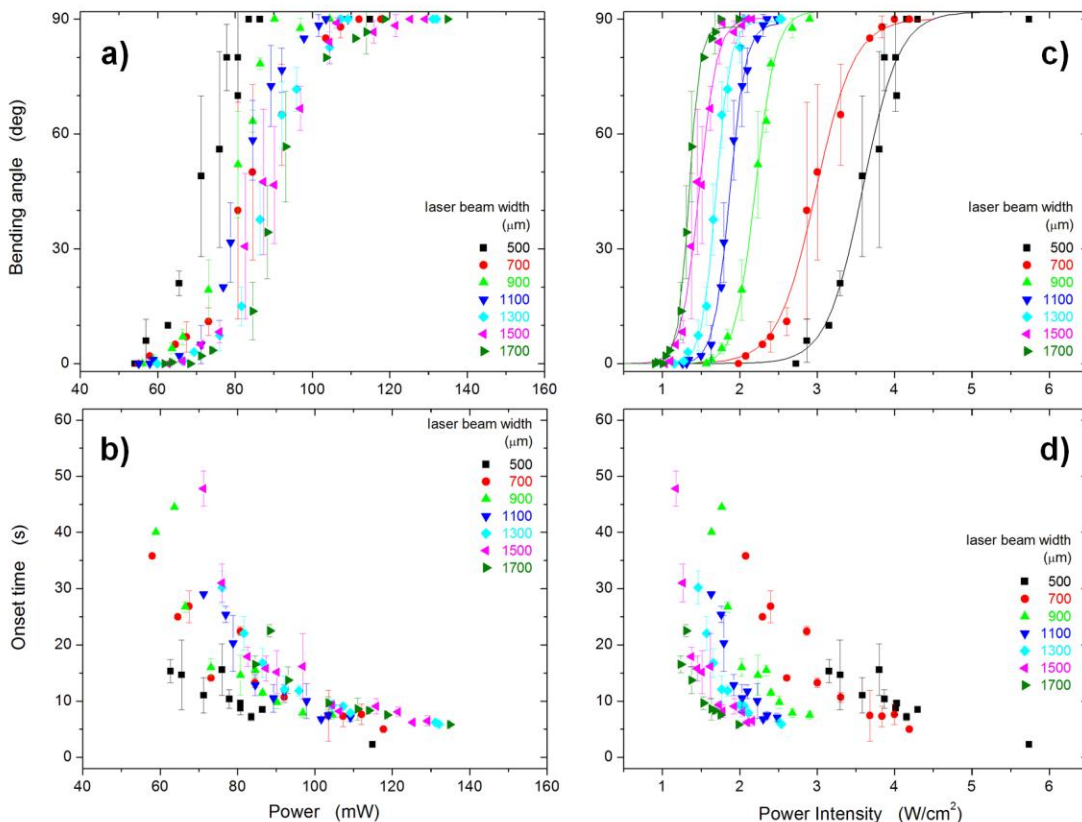


Figure 4.2. Bending angle and onset time of folding as a function of laser incident power or incident intensity when the folding is triggered by IR laser light in a static linear manner. The samples are black ink coated pre-strained polymer sheets (4 mm x 40 mm).

Folding occurs when the hinge exceeds at critical temperature (~ 120 $^{\circ}\text{C}$, which is above the glass transition temperature, T_g , of the sheet of 103°C ¹²) and a thermal gradient is established through the depth of the hinge as discussed in our previous work.¹² As demonstrated in **Figure 4.2**, folding does not occur until power reaches to a threshold value (~ 60 mW). We speculate that below this power threshold, the substrate is able to dissipate the thermal energy such that the polymer beneath the irradiated light never exceeds the T_g of

the polymer sheet. Heat is transferred in a radial direction from the ink surface to the polymer bulk (**Figure 4.3a**).¹² An estimate on the heat dissipation can be calculated by applying a scaling argument. The heat dissipates inside the edges (outlined by dash lines) on both sides of the hinges radially as illustrated in **Figure 4.3b**. This edge effect is more prominent for narrow beam widths. The heat loss on the edges can be described by a cylindrical ordinate using Equation (4.1) as:

$$\dot{Q} \cong \pi k L \frac{\Delta T}{\ln(r_2/r_1)} \quad (4.1)$$

In Equation (1), k is thermal conductivity of the polymer (0.14 W/m/K) measured by the thermal conductivity meter (TA Instruments, DTC-300); L is the width of the polymer sample (4 mm); r_1 is half of the hinge width ($r_1=W/2$); r_2 is the half of hinge width plus the film thickness ($d = 0.3$ mm) since the heat is transferred radially as shown in **Figure 3b**; and ΔT is the temperature gradient across the polymer sheet (~ 20 K) at the intensity of 1 W/cm^2 . Therefore, \dot{Q} is ≈ 45 mW for 0.5 mm hinge, or ≈ 75 mW for 1.0 mm hinge, which is consistent with the threshold power observed from the experiment shown in **Figure 4.2**. This scaling argument estimates the temperature change across the given dimensions (i.e., dT/dr) given an power intensity of $\sim 1 \text{ W/cm}^2$; ΔT can be larger at higher intensities ($>1 \text{ W/cm}^2$). This estimate of heat lost dissipated at the edges of the sample offers a rough approximation of power threshold required to compensate the energy loss before the initiation of shrinkage of the pre-strained polymer sheet so that the folding occurs. This power threshold is consistent with the slope (~ 60 mW) of onset energy for folding (i.e., power multiplies by onset time of folding) plotted as a function of onset time of folding, as shown in **Figure 4.3c**. In **Figure**

4.3c, data points for a wide range of hinge widths (symbols) and power intensities (color scheme) fall onto a universal line with the slope of ~ 61 mW, which divides the folding process into no-folding and folding regions. Moreover, the intercept in **Figure 4.3c** indicates the amount of energy required to heat up the hinge region of the sample to the transition temperature for strain relaxation, which is the heat energy needed in the case of no heat dissipation.

The result of **Figure 4.3c** is remarkable and unexpected. It suggests, counter-intuitively, that increased amounts of energy (onset energy is defined as the amount of energy absorbed at the onset time) result in increased onset times. A more intuitive interpretation of the data is that long onset time associate with increased amounts of wasted energy. Thus, the slope of this plot gives a measure of energy lost per time (~ 60 mW), which agrees remarkably well with the onset energy (**Figure 4.2**) and the scaling argument posed here by Equation 4.1.

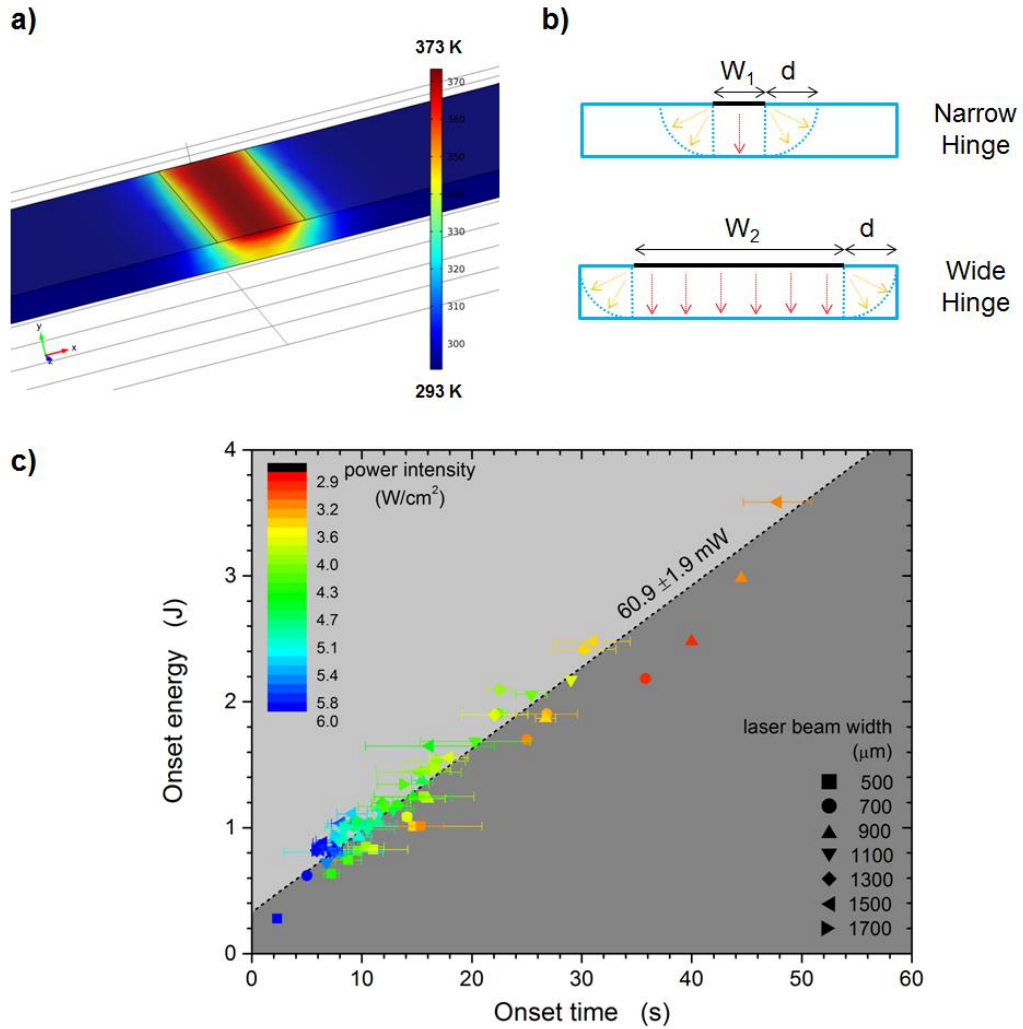


Figure 4.3. (a) Temperature profiles in 3D from the simulation of COMSOL multiphysics; (b) Cross-sectional schematics of heat loss on the edge of the hinge. W_1 and W_2 are the beam widths, and d is the dimension of the edge for heat loss (outlined by dashed line and noted by yellow arrows); and (c) Onset energy as a function of onset time of folding for various beam widths (legend) and incident intensity (color scheme).

To quantify the results of **Figure 4.2** further, we fit the bending angle with the hyperbolic tangent function (**Figure 4.2c**) as described by Equations (4.2):

$$\alpha_B = \frac{\phi}{2} \left[\tanh \left(\frac{I - I_0}{W} \right) + 1 \right] \quad (4.2)$$

In Equation (4.2), α_B is the bending angle, τ is onset time of folding, I is the incident power intensity. I_0 and W are fitting parameters. We use these best fits to identify the inflection point (I_0), which can be physically understood as approximately the transition from no folding to 90 degree folding. **Figure 4.4** plots that the dependence of the inflection point (I_0) on laser beam width. I_0 decreases with hinge width and finally asymptotes to $\sim 1 \text{ W/cm}^2$. This value represents the threshold power intensity to induce folding. As the hinge width increases, the loss of heat to the edges becomes less significant and therefore the intensity required to induce folding starts to plateau. The plateau value ($\sim 1 \text{ W/cm}^2$) represents the total rate of heat loss by the sample. Below this value, the sample dissipates heat so that the hinge never exceeds the critical value. This critical intensity would likely decrease if the sheet started at a higher initial temperature (here, room temperature), although that is outside the scope of this work.

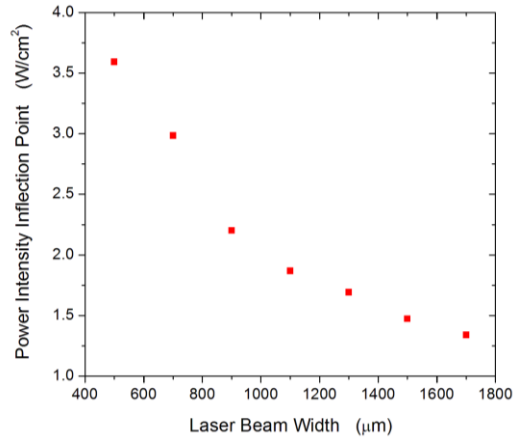


Figure 4.4. Fitting parameters for the inflection point, I_0 obtained from the bending angle vs. intensity using Equation (4.2).

4.4 Conclusion

We demonstrated a process of self-folding of uniform pre-strained polymer sheets induced by the laser writing without pre-patterning of the folding hinge. Using bending angle and onset time as folding characterization metrics, we showed that the power, power intensity, and beam width are all important in governing the folding process. Folding occurs only above a certain power threshold (~ 60 mW) required to compensate for the heat loss to the edge of the hinge. For a given hinge, a larger power increases the angle and decreases the onset time. The substrates are capable of dissipating ~ 1 W/cm² of intensity, based on our measurements.

The ability to induce folding of planar films using light without any pre-patterning represents a significant step in self-folding of polymer sheets due to the simplicity of the method and its compatibility with rapid throughput processing. While here we use a simple pattern of light from the laser to study the fundamentals of folding, the approach is broadly appealing because there are many ways to pattern light, such as photolithography and rastered lasers.

4.5 Acknowledgements

I thank Mr. Matthew Miskiewicz for his great help to set up all optics for the laser, as well as great discussion about the data analysis. I thank Dr. Michael Escuti to allow me use the laser source in his lab and provide great suggestion on data analysis. I thank Ms. Neil Demarse and Dr. Ghazal M Alipour from TA Instruments for the measurement of thermal conductivity of the polymer sheet used. I also would like to thank Dr. Orlin Velev's lab to allow me have the access to COMSOL modeling.

References

1. Cho, J. H., Hu, S. & Gracias, D. H. Self-assembly of orthogonal three-axis sensors. *Appl. Phys. Lett.* **93**, 043505 (2008).
2. Hawkes, E. *et al.* Programmable matter by folding. *Proc. Natl. Acad. Sci.* (2010).
3. Jamal, M., Zarafshar, A. M. & Gracias, D. H. Differentially photo-crosslinked polymers enable self-assembling microfluidics. *Nat. Commun.* **2**, 527 (2011).
4. Stoychev, G., Turcaud, S., Dunlop, J. W. C. & Ionov, L. Hierarchical Multi-Step Folding of Polymer Bilayers. *Adv. Funct. Mater.* **23**, 2295–2300 (2013).
5. Bassik, N., Stern, G. M. & Gracias, D. H. Microassembly based on hands free origami with bidirectional curvature. *Appl. Phys. Lett.* **95**, (2009).
6. Small, IV, W., Singhal, P., Wilson, T. S. & Maitland, D. J. Biomedical applications of thermally activated shape memory polymers. *J. Mater. Chem.* **20**, 3356 (2010).
7. Leong, T. G., Zarafshar, A. M. & Gracias, D. H. Three-Dimensional Fabrication at Small Size Scales. *Small* **6**, 792–806 (2010).
8. Guo, X. *et al.* From the Cover: Two- and three-dimensional folding of thin film single-crystalline silicon for photovoltaic power applications. *Proc. Natl. Acad. Sci.* **106**, 20149–20154 (2009).
9. Jiang, H. Y., Kelch, S. & Lendlein, A. Polymers Move in Response to Light. *Adv. Mater.* **18**, 1471–1475 (2006).
10. Lendlein, A., Jiang, H., Juenger, O. & Langer, R. Light-induced shape-memory polymers. *Nat. Lond. United Kingd.* **434**, 879–882 (2005).
11. Suzuki, K., Yamada, H., Miura, H. & Takanobu, H. Self-assembly of three dimensional micro mechanisms using thermal shrinkage of polyimide. *Microsyst. Technol.* **13**, 1047–1053 (2006).

12. Liu, Y., Boyles, J. K., Genzer, J. & Dickey, M. D. Self-folding of polymer sheets using local light absorption. *Soft Matter* **8**, 1764 (2012).
13. Laflin, K. E., Morris, C. J., Muqem, T. & Gracias, D. H. Laser triggered sequential folding of microstructures. *Appl. Phys. Lett.* **101**, 131901 (2012).
14. Piqué A., Mathews, S. A., Charipar, N. A. & Birnbaum, A. J. Laser origami: a new technique for assembling 3D microstructures. in (Bachmann, F. G. *et al.*) 82440B–82440B–7 (2012).

Supporting Information

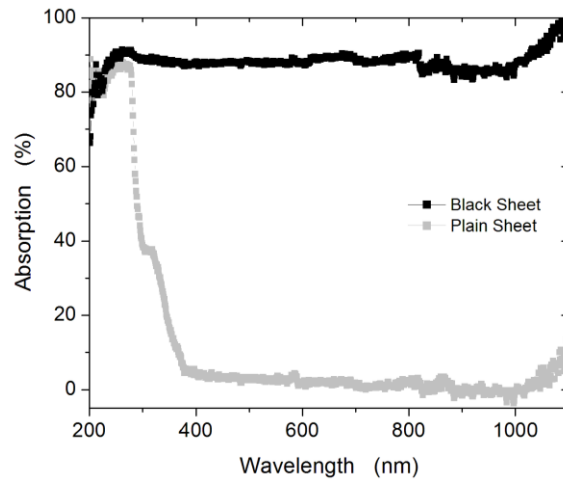


Figure S4.1. UV-Vis Spectra of plain pre-stained polymer sheets and black ink printed pre-stained polymer sheets.

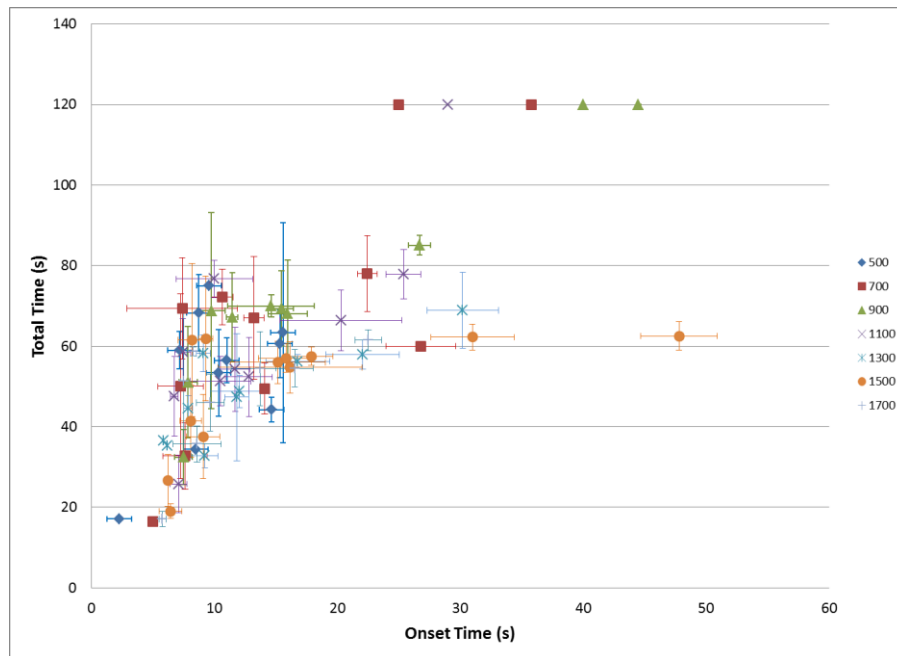


Figure S4.2. The relationship between onset time and total time of folding. (Legend: laser beam width in the unit of microns)

CHAPTER 5

Sequential Folding of Polymer Sheets *via* Color Selection

5.1 Introduction

This chapter describes a novel approach to self-folding of pre-strained polymer sheets in sequential order without complicated multistep fabrication. Folding occurs at ‘hinges’ defined by patterns of ink printed by an inkjet printer. Folding takes place when the ink absorbs light from a lamp, which causes the polymer underneath the hinge to shrink leading to sheet folding selectively at the ‘hinge’. Here, we show that the time scale (and thus, sequence) of folding can be controlled by the wavelength of light, the absorbance of the hinge (based on the color or greyscale), and the width of the hinge. An appeal of this approach is that it utilizes high-throughput two-dimensional (2D) patterning techniques (i.e., photolithography, screen printing and inkjet printing) to create three-dimensional (3D) structures by defining hinges in the 2D substrates and controlling the time sequence of hinge folding.¹⁻³ Self-folding is attractive for a number of applications such as actuators, sensors and packaging. Here, we show a remarkably simple approach for controlling the time scale, direction, and sequence of folding using parameters that can be controlled readily by a printer and the light sources.

The ability to control the folding pathway in sequence is an attractive feature for folding complex origami structures with high yield. For example, embedded Joule-heating elements has demonstrated the ability to control accurately sequential folding pathways in complex structures.^{6,7} Moreover, sequential folding of microstructures with bilayer hinges patterned with pre-strained hinges has been demonstrated using laser light as the trigger.⁸ Meanwhile, we have demonstrated previously self-folding of pre-strained polymer sheets by patterning black ink regions on the sheet that acted as folding hinges.⁹ The black ink

absorbed heat more effectively than the plain polymer when exposed to infrared (IR) light. As a result, the polymer underneath the ink heated gradually through the thickness of the sheet and relaxed the pre-strained sheet to induce folding. In this work we print hinges with different colors (greyscale or color inks) on pre-strained polymer sheets and employ light sources by various wavelengths to achieve selective initiation of folding. This approach allows us to tune the absorption of light and thus timing of folding. Sequential folding, defined simply as time-dependent and programmed folding of multiple hinges printed onto the same sheet, can thus be achieved by using: 1) hinges of different widths and/or colors that are exposed to the same light source, or 2) hinges with the same width and color exposed to different light sources, or 3) the combination of 1) and 2). Our work offers a simple approach for sequential folding of 3D structures without multistep fabrications nor complicated pre-programming.

5.2 Experimental

Clear inkjet shrink film (Grafix[®]) with the film thickness of 0.3 mm was used as the pre-strained polymer sheet. An Epson stylus C88+ inkjet printer produced 2D color ink patterns and A desktop laser printer (HP-P3005dn) produced 2D black ink patterns, which were designed in CorelDRAW[®]. The black ink ratios for different greyscales were measured using ImageJ. An infrared heat lamp (250W, Phillips), 15 watt deep-red, blue and green LEDs (LED Supply) and 50 watt red and blue LEDs (LED-Hero) were used as the heating sources. The samples (25 mm x 10 mm) feature a single black line hinge across the center of the sample. The samples were carried on a hot plate (EchoTherm[™] HS30, Torrey Pines

Scientific) at the pre-heating temperature of 90 °C. The bending angles of the samples were recorded by video camera (Cannon Vixia HF S20). The bending angles were measured by a protractor.

5.3 Results and Discussion

Sequential Folding via Applying Black Ink and Utilizing IR Heat Lamp

Sequential folding occurs when certain hinges in the sheet fold faster than others in response to a uniform or local stimulus. The temporal response of a hinge can be quantified by the ‘onset of folding’ (i.e., the duration of exposure to light prior to the initiation of folding). One way to control the onset of folding is to vary the width of black hinges, which absorbs light very efficiently based on our previous work.⁹ In which case, we utilized an IR lamp (power density $\sim 1 \text{ W/cm}^2$) to fold pre-strained polystyrene sheets resting on a hotplate (50 to 90 °C). In these experiments, folding occurs fast (1~2 s onset time) with wide hinges (1.5 to 2.0 mm), whereas folding occurs slower (10~20 s) with narrow hinges ($\leq 1.2 \text{ mm}$). **Figure 5.1** shows the bending angle (α_B , i.e., the angular displacement of the fold, which is complementary to folding angle) versus time for different hinge widths with all other parameters being constant. Given the small difference in folding times between the narrowest and widest hinge width studied here controlling hinge width alone does not offer sufficiently general approach for controlling the sequence of folding.

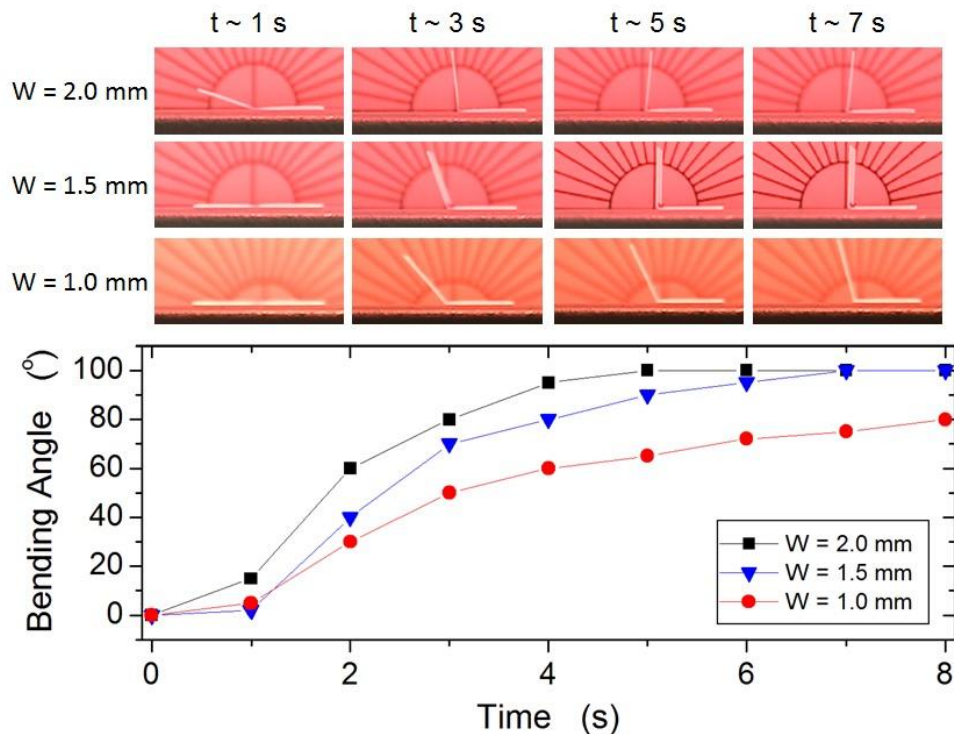


Figure 5.1. (Top) Representative photographs of the folding process with different hinge widths (2.0, 1.5 and 1.0 mm from top to bottom) when the samples are rest on the hotplate of 90 °C and under the exposure of IR heat lamp at a distance of 5 cm (power density ~ 1 W/cm²). The samples (25 mm x 10 mm) feature a single black line hinge across the center of the sample. A printed protractor image is set as the background (Bottom) Bending angles change with different hinge widths (2.0, 1.5 and 1.0 mm) as a function of time.

Utilizing the absorbance of the hinge is another strategy for controlling sequential folding. Hinges printed in greyscales can be employed as alternatives for achieving sequential folding. Hinges in greyscales produced by desktop printers comprise different densities of uniformly distributed black dots on a transparent background, as shown in **Figure 5.2a**. Here we employ “percentage of black in greyscale” as the percent of black color to represent the greyscale. Thus, hinges with lower greyscale (i.e., less intensity of black dots in white background) absorb less light per area than hinges with higher greyscale

(i.e., high intensity of black dots in white background). The optical absorption of these greyscale patterns are shown in **Figure 5.2b**. As documented in **Figure 5.2c**, increased greyscale correlates directly to the absorption of light.

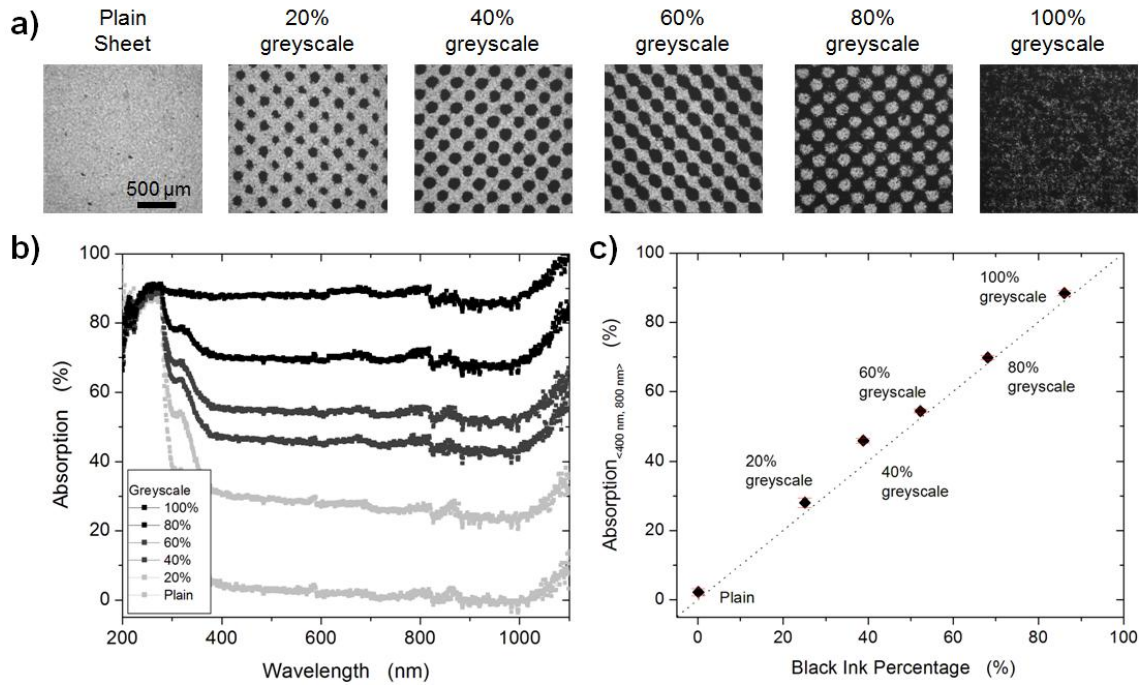


Figure 5.2. (a) Optical microscope images of plain polymer sheet and polymer sheet patterned with various greyscale levels, i.e., percentages of black ink (20%, 40%, 60%, 80%, and 100%) in grayscale. (b) Absorption spectra for the plain pre-strained polymer sheet and the black ink printed sheet with different greyscales ranging from 200 nm to 1100 nm. (c) Relationship of average optical absorption ranging from 400 to 800 nm with the percentage of black ink for the plain polymer sheet and the sheets printed with different greyscales. The dash line ($y=x$) is a guide to the eye.

Figure 5.3 shows the folding performance using hinges with different greyscales and two different widths (1 and 2 mm). The onset time decreases with increasing greyscale and/or increasing the hinge width. Concurrently, the bending angle increases with increasing

the level of greyness and/or increasing the hinge width. Hinges with <20% greyscale cannot absorb a sufficient amount of heat to induce folding. Large α_B ($\sim 90^\circ$) can be only achieved in samples with high greyscale ($\geq 60\%$). The gradual increase in the onset time of folding with increasing the greyscale can induce folding or rolling on substrates patterned with a gradient of greyscales. **Figure 5.4** demonstrates the principle of achieving sequence with greyscale and also introduces a new mode of actuation—“sequential rolling”—utilizing wide multiple hinges with a gradient of greyscales. A glass slide compresses the left side of all of the samples to the hot plate except for the sample in **Figure 5.4a**. **Figures 5.4a, b** show a continuous gradient of greyscales, in which the darkest regions fold the fastest. **Figures 5.4c, d** show discrete hinges with decreasing (or increasing) amounts of greyscale.

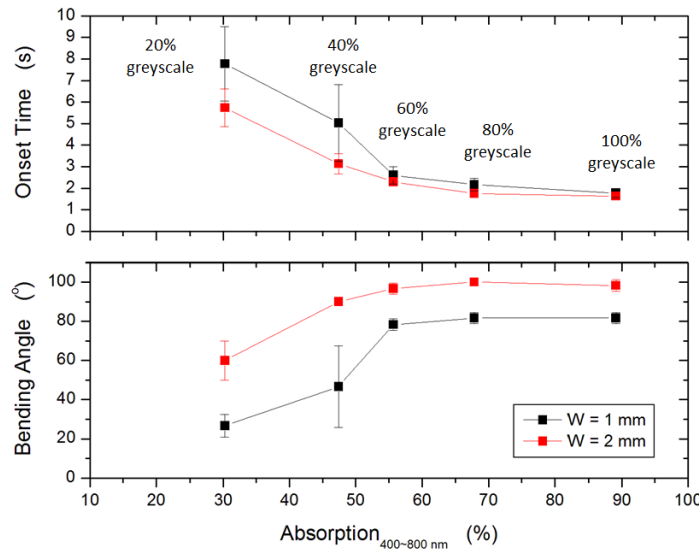


Figure 5.3. (Top) The onset of folding and (Bottom) the bending angle as a function of absorption for the ink hinges with different greyscales (20~100%) and different hinge widths ($W = 1$ mm and 2 mm). The samples (25 mm x 10 mm) feature a single black line hinge across the center of the sample. The samples are rest on the hotplate of 90°C and under the exposure of IR heat lamp at a distance of 5 cm.

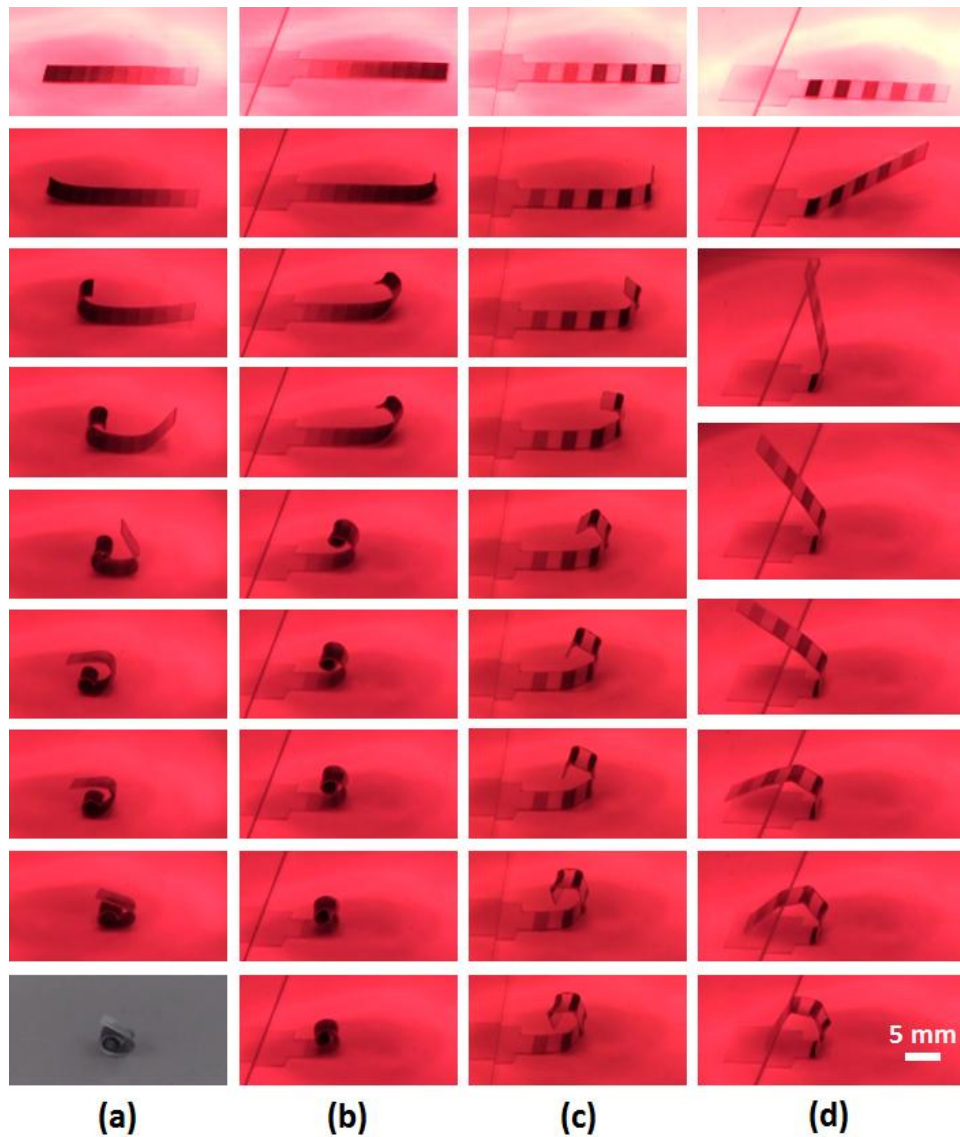


Figure 5.4. Photographs for sequential rolling process of pre-strained polymer sheets patterned with descending greyscales by 10% black from 100% black to plain sheet. The sample is 22 mm x 5 mm. Time interval for processes (a)-(c) is one second, and time interval for process (d) is one second except last picture is at 9th second. The samples are rest on the hotplate of 90 °C and under the exposure of IR heat lamp at a distance of 5cm. The samples for processes (b)-(d) were pressed by a glass slide on the left side.

Sequential Folding via Applying Color Inks and Utilizing LED Lights

Light emitting diodes (LEDs) emit light at a specific wavelength whereas an IR heat lamp emits a broad spectrum spanning the visible to the IR regime. Utilizing LEDs as the light stimulus for folding has two important advantages relative to an IR heat lamp. First, it allows for the use of colored hinges that absorb (or transmit) selectively the light from the LED. In contrast, greyscale inks absorb light indiscriminately and are thus more difficult to control. Second, although the polymer sheets are optically transparent in the visible range (i.e., the range covered by the LEDs used here), they do absorb in the IR wavelengths region. As a consequence, the ‘panels’ (i.e., regions of the sheet without ink) heat and distort in response to long exposures of light.

We utilized three different LEDs (green, blue, red with different wavelengths as shown in **Table S5.1** *cf.* Supporting Information) and printed inks using the CMYK color scheme from a desktop printer.. The printed color inks are the composite of dots of cyan, magenta, yellow and black which can be observed under the optical microscopy (**Figure S5.1** *cf.* Supporting Information). **Figure 5.5** plots the UV/Vis absorption spectra of different colors patterned on a plain, transparent polymer sheet. Images of the LED light sources placed above the figure indicate the wavelengths of interest and help identify inks with selective absorption (or transmission). For example, yellow and cyan inks are ideal because they show opposite absorption behaviors at 470 nm (blue LED) and 660 nm (deep-red LED). The differential absorption of color inks at specific wavelengths thus provides more freedom for the design of hinges with selective absorption for sequential folding.

We demonstrate sequential folding using two different color hinges (yellow and cyan inks) that respond selectively and preferentially to hand-held LED torches (15W) with two specific colors as shown in **Figure 5.6**. The yellow hinge only responds to 660 nm (deep-red LED) to cause folding and remains flat under blue LED illumination even after extended exposures (10 min); while sheets printed with cyan hinge remain flat under the same LED for 10 minutes but fold in response to 470 nm (blue LED) in just a few seconds. This simple idea can be extended to other color pairs with different LED lights. (**Figure S5.2** cf. Supporting Information). This demonstration qualitatively validates the concept that sequential folding of 2D substrates patterned with different color hinges can be achieved by utilizing specific wavelengths to trigger those color hinges selectively.

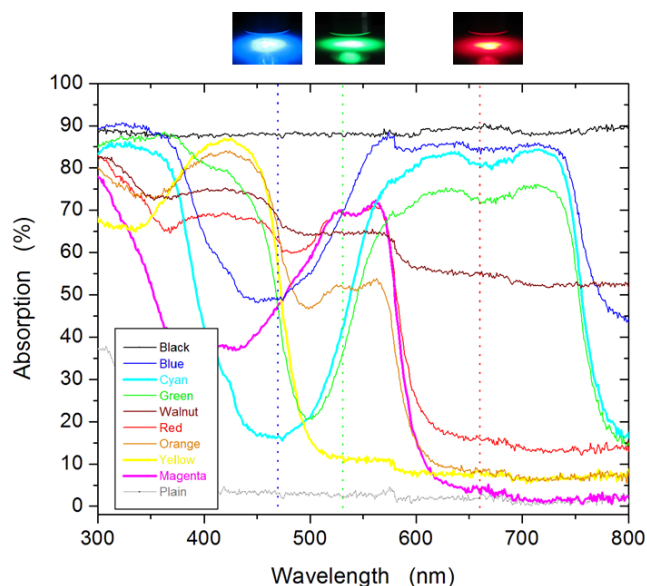


Figure 5.5. Absorption spectra of color inks printed on plain pre-strained polymer sheet and plain sheet. Dash lines represent the typical wavelengths for blue (470 nm), green (530 nm) and deep-red (660 nm) LEDs as shown in inset photos.

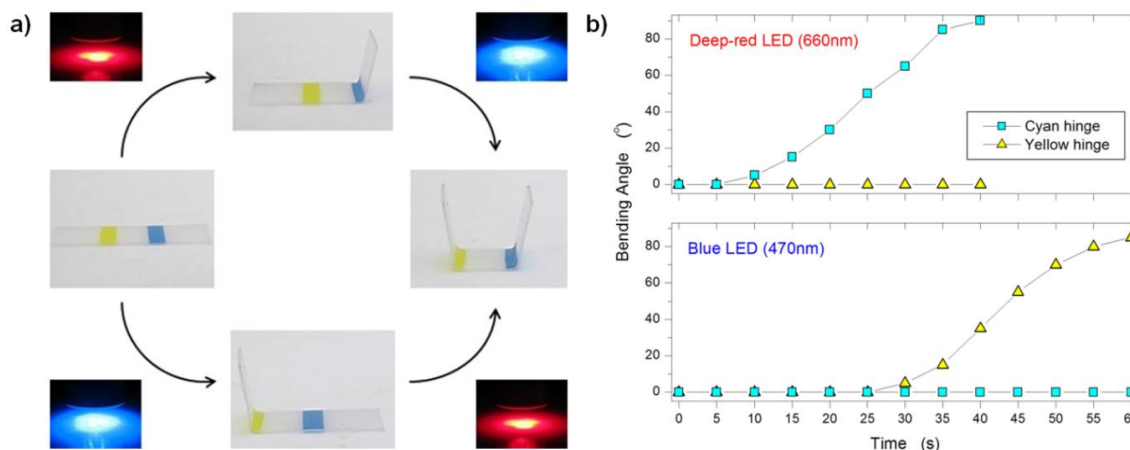


Figure 5.6. (a) Photographs for “sequential folding” by utilizing the hinges in yellow (in response to blue LED) and cyan (in response to deep-red LED). 15W LEDs were used at a distance of 1.5 cm from the sample. (b) Change of bending angle with time for yellow and cyan hinges under the exposure of deep-red and blue LEDs separately.

Besides the color of lights (i.e., wavelengths for light), light intensity and hinge width are also important to induce the folding in sequence. Intuitively, either high light intensity or wide hinge width can absorb high energy to induce folding in a fast pace. We, therefore, studied different parameters affecting the folding process. We utilized 50 W LEDs with large irradiation area (40 mm x 40 mm) to investigate the impact of those key parameters and to offer more uniform light exposure for the templates. Two wavelengths of light were used: 630 nm (Red LED) and 470 nm (Blue LED). Here, 630 nm Red LED instead of 660 nm Deep-red LED was used for the following systematic study on key parameters and demonstrations due to the product availability from the vendor.

The self-folding process (tested by single line hinge here), quantified in terms of the onset folding time and the bending angle is controlled by key parameters which are 1) the

wavelength (color) and 2) intensity of light, 3) absorption of light by the inks, and 4) the hinge width (if we consider sheets of the same thickness). The experimental approaches to vary those parameters are listed in **Table 5.1**. Here, we only uses two wavelengths of light are used: 630 nm (Red LED) and 470 nm (Blue LED) to study the first parameters (P1). In either case, folding process (onset time of folding and bending angle) is studied in response to the effects of light intensity (P2), light absorption by inks (P3), and hinge width (P4). The most prominent effects are summarized in **Table 5.1**, while the complete experimental results are plotted in **Figure S5.3** (*cf.* Supporting Information). To simplify the study, we only utilized two wavelengths (P1, 630nm and 470 nm) here. Also, wide hinges (2.0 mm) usually provide $\alpha_B \sim 90^\circ$ while narrower hinges lead to smaller α_B . Therefore, we mostly used templates featuring hinge widths of 2.0 mm to realize the 3D structures with large α_B .

Table 5.1. Key process parameters important for sequential folding.

Parameters	Method to control	Effects
P1: Wavelength (λ)	LED colors (Red, Blue LEDs tested)	Determines light absorption of different color inks
P2: Intensity of light (I)	Adjust distance from light to sample (1.0 ~ 3.0 cm tested) (Table S5.1)	Very low intensity (~ 400 mW/cm ²) cannot provide sufficient energy for folding; high intensity ($\sim 1,500$ mW/cm ²) induces folding even ink absorption $< 20\%$.
P3: Absorption of light by inks (A)	Use different CMYK color scheme (Table S5.2)	Roughly $> 40\%$ absorption of light needed for folding if using moderate light intensity
P4: Hinge width (W)	1.0; 1.5; 2.0 mm tested	Usually $\sim 90^\circ$ when $W=2.0$ mm

Besides P1 and P4, we studied the effect of P2 and P3 on the folding process as shown in **Figure 5.7a, b**. The axis labeled “absorption” combines the convolved effect of light wavelength (here red and blue LEDs) and absorption by the inks. In general, fast folding (onset time < 10 s) and large folding (bending angle close to 90°) occur with high light absorption and high light intensity. To consider the power needed for folding, **Figure 5.7c, d** plots the onset time and bending angle as a function of the power (mW) obtained by multiplying the light power areal density intensity (mW/cm²) with ink absorption (dimensionless) and hinge area (cm²). Bending angles close to 90° can be obtained when the power is > 50 mW/cm. The trends in **Figure 5.7** appear independent of LED wavelength and

instead, depend solely on absorbed light, as expected. Therefore, the folding with large bending angle (90°) or fast onset time (< 10 s) can be achieved as long as the desired power (>60 mW), while the desired power can be obtained by adjusting proper light intensity, hinge width and absorption of inks.

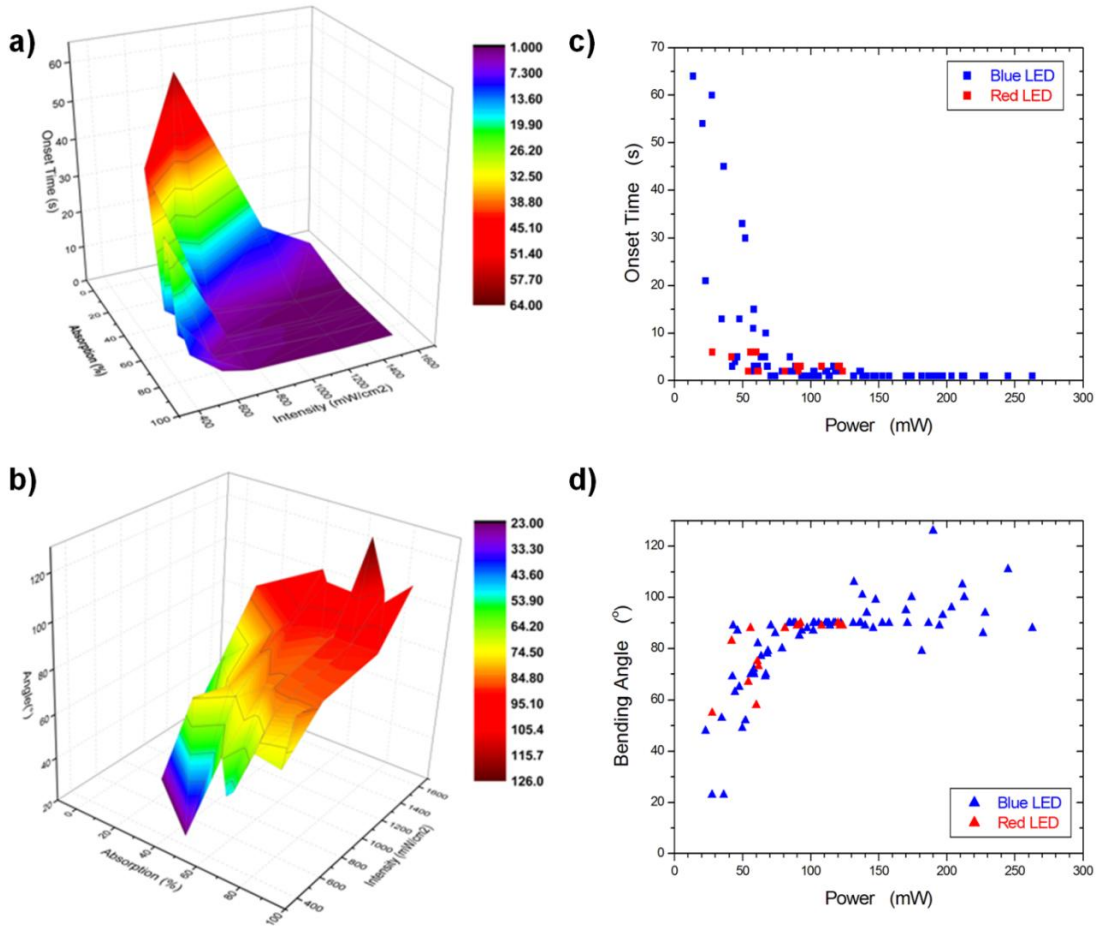


Figure 5.7. 3D plots of onset time (a) and bending angle (b) for folding with optical absorption of inks and light intensity. Data points include the test using samples with different hinges widths (1.0, 1.5, and 2.0 mm) and different LEDs (red LED and blue LED). Onset time (c) and bending angle (d) for folding as a function of power for both red and blue LEDs. Samples (25 x 12 mm) feature a single line of ink patterned across the center of the sample.

Although indispensable contribution of all these parameters (P1~P4) to the folding process, we sought to create a practical guide for sequential folding which only need relies on the color selection (i.e., LED colors and ink colors). As discussed above, we prefer to use templates featuring hinge widths of 2.0 mm to realize the 3D structures with large α_B . Moreover, we fixed the LED distance over the sample during the experiment to achieve sufficient intensity for folding ($> 400 \text{ mW/cm}^2$) but to keep relatively spacious distance to allow 3D structures formed without collision to the light. Therefore, the red LED is set at a distance of 1.5 cm from the sample with an estimated intensity of 601 mW/cm^2 and the blue LED is set at a distance of 2.0 cm from the sample with an estimated intensity 743 mW/cm^2 (the intensity ranges for different LED lights are listed in **Table S5.2** (*cf.* Supporting Information). **Figure 5.8** describes the absorption properties as a function of ink color. By assuming the fixed conditions of P1 and P4 have been applied as described above, the selection of color hinges has to satisfy the light absorption for the LED $> 40\%$ (referred to the discussion about **Table 5.1** and **Figure S5.3**). A sample selection has been listed in **Table 5.2**.

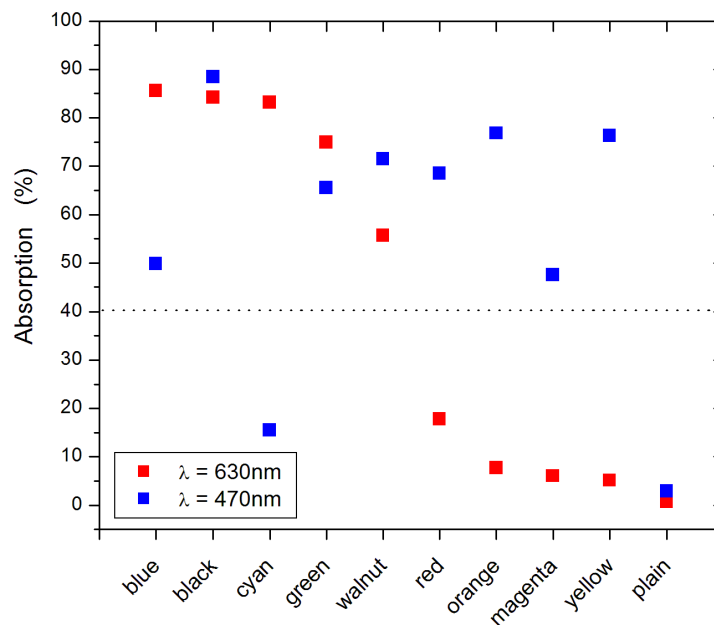


Figure 5.8. Color selection guideline for the sequential folding using color hinges. The hinge width is 2.0 mm, and 50 W red and blue LED lights are used set with moderate intensities as described above. The dash line denotes the minimum absorption (> 40%) desired to achieve a good folding.

Table 5.2. Examples of color selection for sequential folding. 1st hinge represents the hinge which folds first in that case, while 2nd hinge represents the hinge which folds following 1st hinge. Yes or No represents folding or no folding separately.

Example	LED Color	1 st Hinge	2 nd Hinge
1	Red	Cyan (Yes)	Yellow (No)
	Blue	Cyan (No)	Yellow (Yes)
2	Red	Green(Yes)	Orange (No)
	Blue	Yellow (Yes)	Cyan (Yes)

5.4 Applications of Sequential Folding

Further examples of the sequential folding utilizing color hinges and LEDs have been demonstrated here. For example, sequential folding of nested boxes represents a similar structure like “Matryoshka doll” as shown in **Figure 6.9a**. A smaller box ($5 \times 5 \times 5 \text{ mm}^3$) with green hinges folds under the exposure of red LED while larger box ($10 \times 10 \times 10 \text{ mm}^3$) with orange hinges stays flat, which is consistent with the absorption of green and orange colors in **Figure 5.8**. The larger box with orange hinges folds after switching to blue LED. This example represents the sequential folding with light control. Moreover, unfolding pathway can be realized by patterning different color hinges on both sides of the polymer sheet as shown in **Figure 6.9b**. First, the blue hinge (facing to LED) can be folded under the exposure of red LED, and then folding of the red hinge can be induced when flipping the sample and making the red hinge faces to blue LED. Therefore, unfolding can be finally achieved. More applications by employing sequential folding will be further studied.

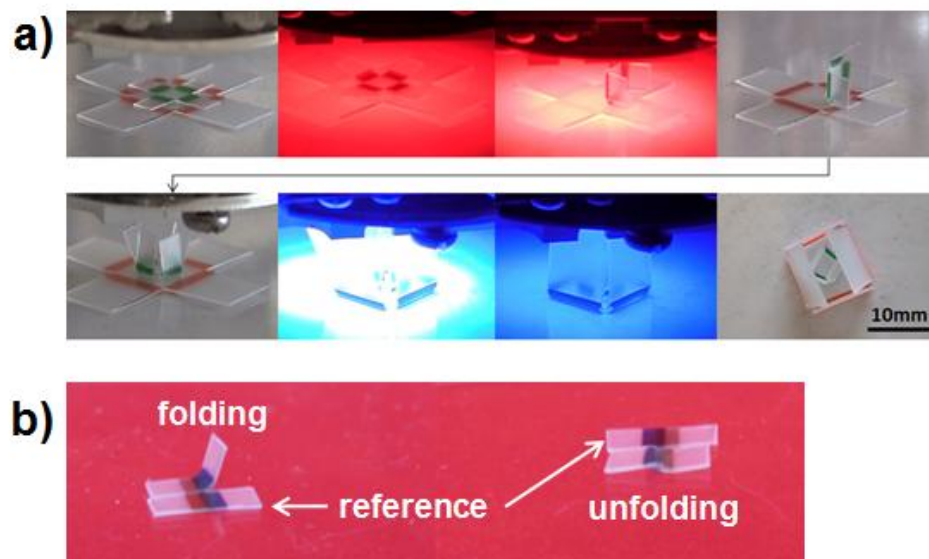


Figure 5.9. Strategy of sequential folding applied for (a) folding nested boxes with light control; and (b) realizing the unfolding pathway with color hinges patterned on both sides of the polymer sheet. All samples are rested on the hotplate at 90 °C for folding.

5.5 Conclusion

We demonstrated a novel and simple approach to realize sequential folding of 3D shapes by patterning inks of different light absorptivity (i.e., greyscale inks or color inks) as hinges on homogeneous pre-strained polymer sheets. Sequential self-folding or rolling can be realized by utilizing hinges with decreased light absorption for potential applications such as grippers or actuators. Moreover, hinges of different color printed onto the same sheet offer the ability of sequential folding upon the exposure of different light sources (i.e., light wavelengths). This approach demonstrates the realization of sequential folding tuned by: hinge width, hinge color and the type (and wavelength) of the light source. This method only requires one-step inkjet printing on a 2D substrate to create complex 3D shapes. Various demonstrations of

self-folding have been shown in this work to validate this approach, which can be further applied for origami folding, multifunctional devices and unfolding pathways.

5.6 Acknowledgements

I thank Ms. Brandi Shaw for her diligent and active work with me in the lab for this study on sequential folding using different light sources and color hinges. I thank Mr. Stephen Reece for his help to set-up the Epson printer. I thank Mr. Ching-Kit Yeung (Equipment & Facilities Support in our department) for his help to assemble the heat sink element to high power LED lights.

References

1. Leong, T. G., Zarafshar, A. M. & Gracias, D. H. Three-Dimensional Fabrication at Small Size Scales. *Small* **6**, 792–806 (2010).
2. Azam, A., Leong, T. G., Zarafshar, A. M. & Gracias, D. H. Compactness Determines the Success of Cube and Octahedron Self-Assembly. *PLoS ONE* **4**, e4451 (2009).
3. Ionov, L. Soft microorigami: self-folding polymer films. *Soft Matter* **7**, 6786 (2011).
4. Pandey, S. *et al.* Algorithmic design of self-folding polyhedra. *Proc. Natl. Acad. Sci.* **108**, 19885–19890 (2011).
5. Stoychev, G., Turcaud, S., Dunlop, J. W. C. & Ionov, L. Hierarchical Multi-Step Folding of Polymer Bilayers. *Adv. Funct. Mater.* **23**, 2295–2300 (2013).
6. Hawkes, E. *et al.* Programmable matter by folding. *Proc. Natl. Acad. Sci.* **107**, 12441–12445 (2010).
7. Felton, S. M. *et al.* Self-folding with shape memory composites. *Soft Matter* **9**, 7688 (2013).
8. Laflin, K. E., Morris, C. J., Muqem, T. & Gracias, D. H. Laser triggered sequential folding of microstructures. *Appl. Phys. Lett.* **101**, 131901 (2012).
9. Liu, Y., Boyles, J. K., Genzer, J. & Dickey, M. D. Self-folding of polymer sheets using local light absorption. *Soft Matter* **8**, 1764 (2012).

Supporting Information

Table S5.1. Measured power density for different LED lights used for the folding test.

Color	Wavelength (μm)	Nominal Power of LED (W)	Distance to Sample (cm)	Power Density (mW/cm ²)
Deep-red	660	15	1.0	580
			1.5	519
			3.0	362
Green	530	15	1.0	318
			1.5	285
			3.0	181
Blue	470	15	1.0	727
			1.5	636
			3.0	373
Red	630	50	1.0	916
			1.5	602
			2.0	513
			3.0	261
Blue	470	50	1.0	1541
			1.5	1238
			2.0	743
			3.0	421



Figure S5.1. Optical microscope images of different CMYK inks. From left to right are blue, cyan, green, 40% black, black (top row); and magenta, red, orange and yellow (bottom row). The scale bar is 500 μm.

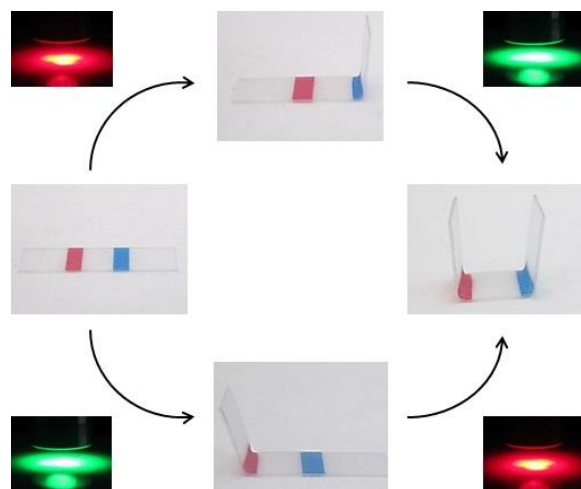


Figure S5.2. Photographs for “sequential folding” by utilizing the hinges in magenta color (in response to green LED) and cyan (in response to deep-red LED). 15W deep-red LED was used at a distance of 1.5 cm from the sample, and 15W green LED was used at a distance of 0.7 cm from the sample due to the low power density of green LED.

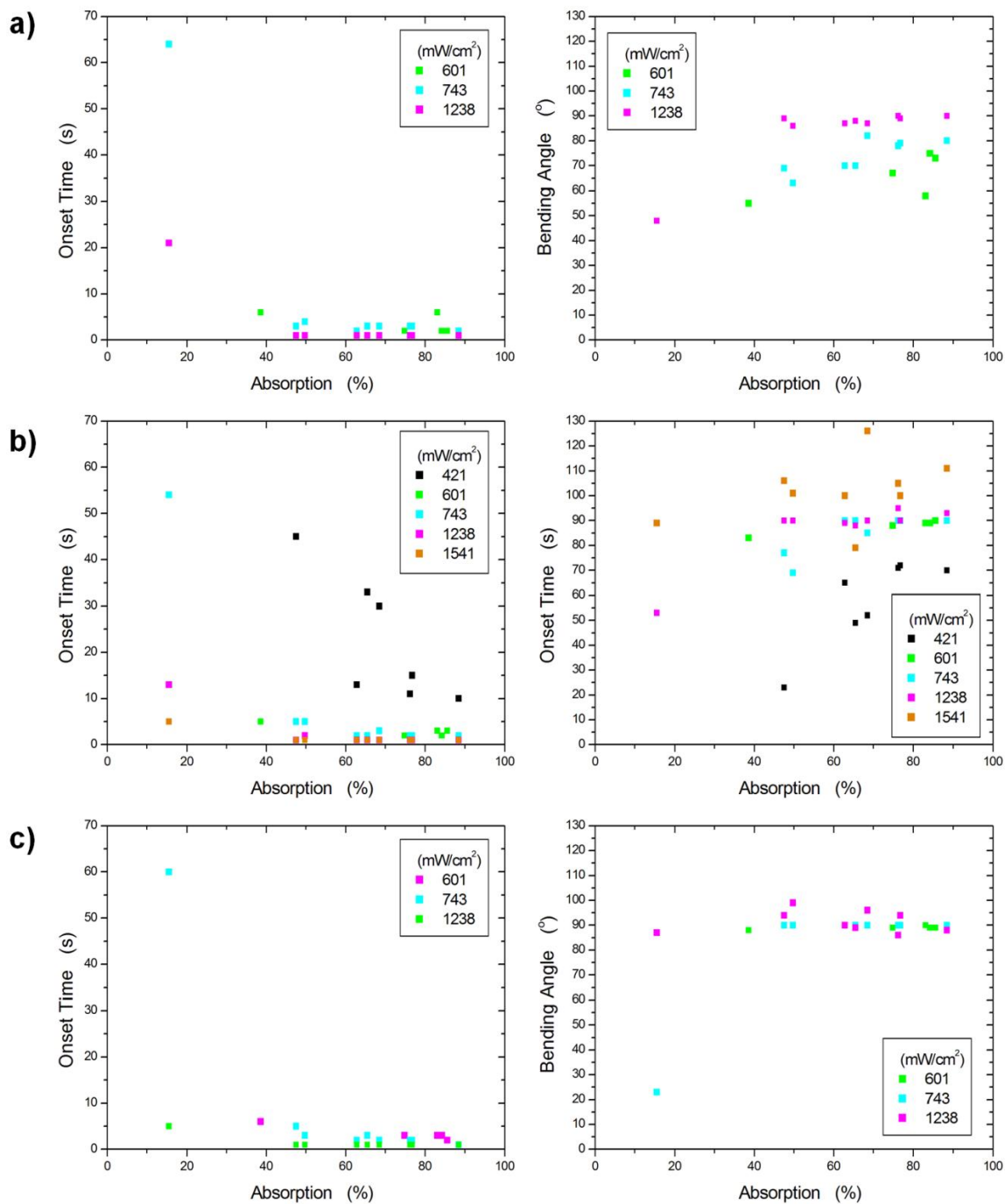


Figure S5.3. Dependence of onset time (left) and bending angle (right) for folding on the key process parameters (i.e., ink absorption and light intensity) for different hinge widths of (a) 1.0 mm (b) 1.5 mm; and (c) 2.0 mm.

CHAPTER 6

Formation of Isotropic Buckles on Polystyrene and Enhancement of its Aspect Ratio

6.1 Buckles based on Polystyrene Laminates

Poly(dimethylsiloxane) (PDMS) and its derivatives have been used widely to produce wrinkled surfaces¹⁻⁴ primarily due to their low modulus ($E \sim 1$ MPa) and high coefficient of thermal expansion (CTE) ($\approx 96 \times 10^{-5} \text{ K}^{-1}$). In addition to silicones, other materials have also been employed in generating wrinkles, albeit to a smaller extent, primarily due to higher E and lower CTE than that of PDMS. One example involves polystyrene (PS) that has a $E \approx 3.2$ GPa⁵ and $\text{CTE} \approx 7 \times 10^{-5} \text{ K}^{-1}$.⁶ Those attributes, in addition to a relative high glass transition temperature (T_g) of ~ 100 °C make PS less amenable for buckling experiments at room temperature. However, when heated above the T_g , PS can be used as a substrate for buckling, as demonstrated by multiple research groups during the past few years.⁵⁻⁸ Thin films of PS, a relatively chemically inert thermoplastic,⁹ are easy to prepare by spin-coating on solid supports from a toluene solution. The PS film can be decorated with a thin layer of metal or oxide that completes the formation of the bilayered laminate. Much research has been done on buckling of Al/PS bilayers.^{6,7,10} Buckling occurs due to the mismatch of thermal expansion between the Al capping film ($\text{CTE} = 25 \times 10^{-6} \text{ K}^{-1}$) and the PS substrate, as mentioned in Chapter 1. In addition to Al we also use indium tin oxide (ITO) film as a capping film, whose CTE ($10 \times 10^{-6} \text{ K}^{-1}$)¹¹ is on the same order of magnitude as that of Al. The mismatch of thermal expansion between the capping film (i.e., ITO) and silicon support ($3 \times 10^{-6} \text{ K}^{-1}$) can cause the formation of buckles as well. Due to its high transparency and good electrical properties, ITO is widely used in manufacturing of transparent electrodes in solar cells and flat panel displays.¹²

6.2 Experimental

Silicon substrates were cleaned in acetone and isopropanol sequentially by in 10 minute long ultrasonic treatment, followed by 10 minutes of ultraviolet ozone treatment. Polystyrene pellets ($M_w = 230$ kDa, $M_n = 140$ kDa) were dissolved in toluene to prepare polymer solutions of different concentrations. Polystyrene thin films with different thicknesses were formed by spin-coating the solutions on silicon substrates (**Table S6.1**). The spin-coated films were annealed over 110 °C for 3 hours on a hotplate to remove any residual solvent. The ITO films were deposited using RF sputtering system (power = 20W) with an ITO target. The base pressure of the chamber was $\sim 1.6 \times 10^{-6}$ Torr and process pressure was 4 mTorr. Al films were deposited using DC sputtering system (power = 30 W). The base pressure of the chamber for sputtering was $< 1 \times 10^{-5}$ Torr and the pressure during the sputtering was 6 mTorr. The real-time development of buckles was observed with optical microscope through the open hole in the hot-stage.

6.3 Results and Discussion

Figure 6.1 shows typical buckles formed in ITO/PS bilayer samples resting on top of a flat solid support (silicon wafer). AFM reveals that the surface morphology comprises isotropic buckles. In addition, buckle formation was also studied in systems involving ITO films deposited on free-standing PS sheet as shown in **Figure 6.2**. There are no buckles observed in the samples even by heating them to temperatures > 160 °C. This observation is consistent with earlier work in the literature, which discusses mechanism of buckle formation in metal/PS bilayer films resting on silicon support.⁶

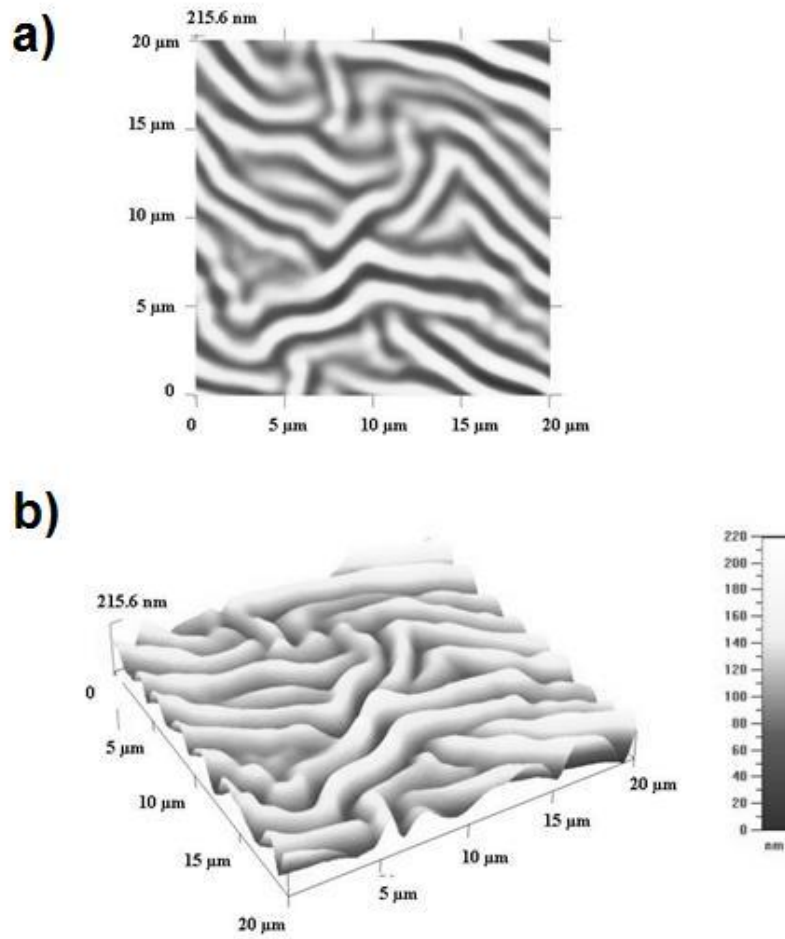


Figure 6.1. AFM images of isotropic buckles based on ITO (40 nm)/PS (200 nm) bilayer resting on top a silicon substrate. 2D top view (a) and 3D tilt view (b). The wavelength is $\approx 1.76 \mu\text{m}$ and the aspect ratio is ≈ 0.06 .

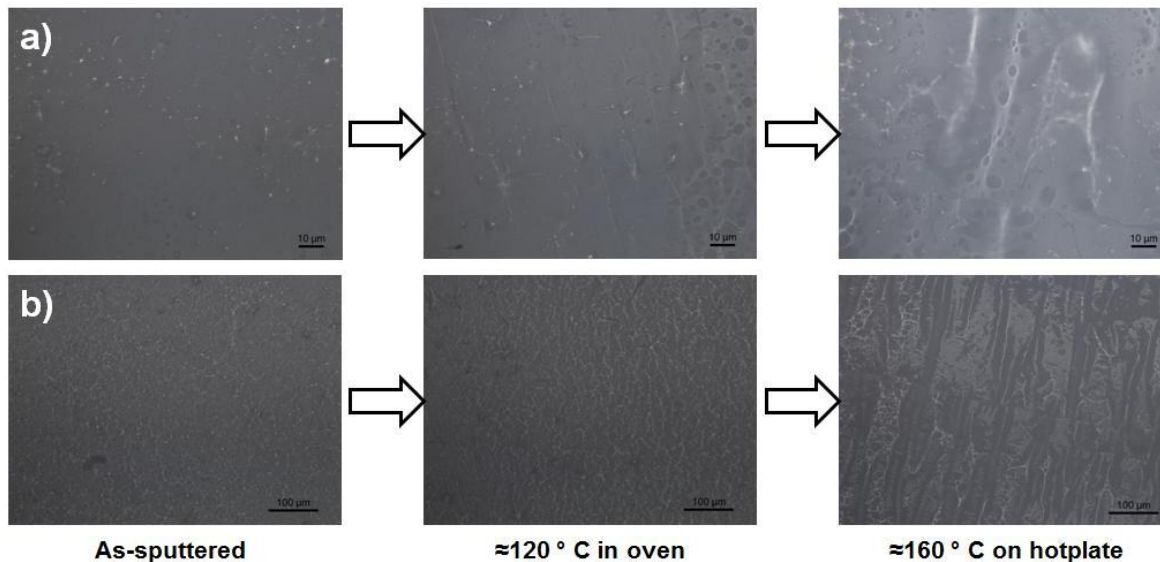


Figure 6.2. Investigation of buckle formation on ITO (thickness ~ 100 nm) coated free-standing PS sheet under optical microscope under (a) 1000X and (b) 200X magnifications.

The wavelength (λ) of those isotropic buckles can be increased by increasing the thickness of either the metal or the polymer layers.⁶ In addition, the buckle wavelength depends of the material properties of both layers, such as E, CTE, Poisson's ratio.^{6,13} We have established that the wavelength ranged from 4 to 14 μm when changing the ITO thickness from 40 to 500 nm on a 1.5 μm thick PS film, or by changing the PS thickness from 200 nm to 19 μm when the ITO thickness was 40 nm.¹⁴ The thickness of the PS films was adjusted by varying the concentration of PS stock solutions and spin-coating conditions as listed in **Figure S6.1** and **Table S6.1**. Representative buckles formed when employing thin PS film (150 ~ 650 nm) as shown in **Figure 6.3**. In thin films (~ 150 nm) we detect the presence of cracks instead of buckles; buckles developed in thicker PS films. However, the

buckled morphology was not uniform through the surface for these thin PS films (< 650 nm thick). Buckles formed on thicker PS films (> 1.5 μm) were more isotropic **Figure 6.4**.

Real-time investigation of buckle formation on ITO/PS/Si samples reveals “minimum annealing temperature” (T_{min}) ~ 105 $^{\circ}\text{C}$ at which the buckles start to form. For example, T_{min} is ≈ 106 $^{\circ}\text{C}$ for ITO (50 nm)/PS (1.5 μm)/Si sample as shown in **Figure 6.4**. Also, T_{min} is ≈ 107 $^{\circ}\text{C}$ for the ITO (50 nm)/PS (**Figure S6.2**) sample. This is consistent with the study on isotropic buckles of Al/PS on silicon substrates reported in the literature (**Figure 6.5**).⁶ T_{min} can be understood as the temperature when thermally induced stress from CTE mismatch between the two layers reaches a certain critical stress value. In addition, T_{min} depends on the molecular weight of PS (T_{min} changes more significantly with the change of PS thickness if using high molecular weight PS).⁶ Increasing the Al film thickness (from 30 to 50 nm) does not affect T_{min} . For example, a Al (30 nm)/PS (200 nm) bilayer film on silicon substrate forms buckles at $T_{\text{min}} \approx 105$ $^{\circ}\text{C}$.⁶ Similar trend was also observed in ITO/PS films. For instance, T_{min} is around 100 \sim 105 $^{\circ}\text{C}$ for ITO (40 nm)/PS bilayer films with PS thicknesses \sim 500 nm.¹⁴

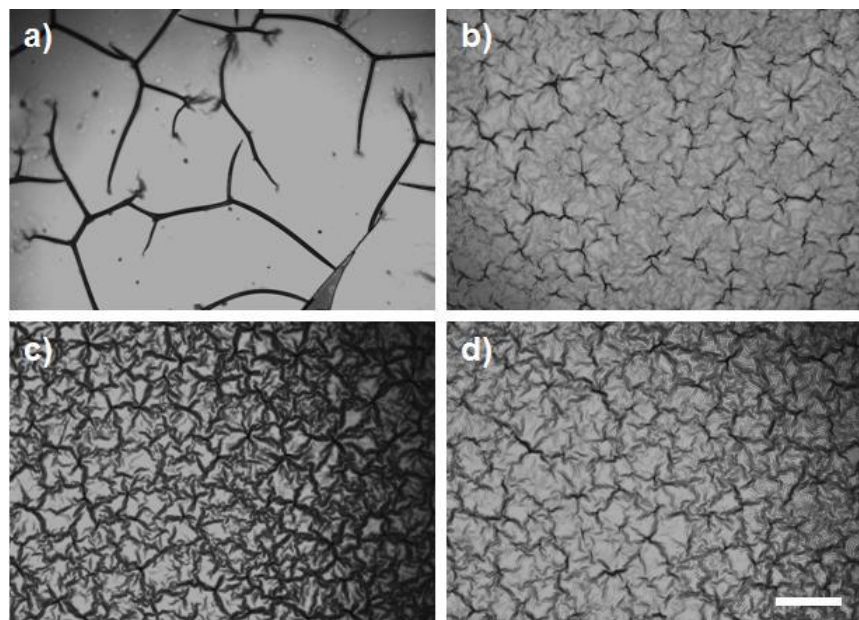


Figure 6.3. Optical microscope images of isotropic buckles based on ITO (40 nm)/PS films with different thicknesses of PS (a) 150 nm; (b) 370 nm; (c) 530 nm and (d) 650 nm on a silicon substrate. The ITO thin film was deposited by 20W RF sputtering with 4 mTorr Ar pressure. The sample was heated on the hotstage with the heating rate of 10 °C/min from room temperature to 120 °C. The scale bar is 100 μm .

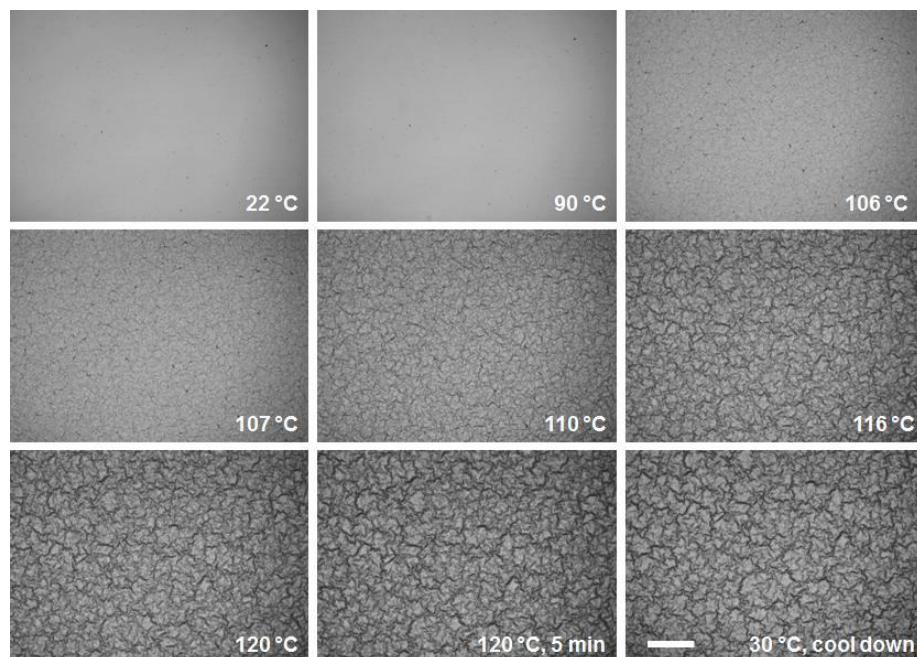


Figure 6.4. Real-time investigation of isotropic buckles based on an ITO (50 nm)/PS (1.5 μm) bilayer on a silicon substrate. The buckles start to grow around ~ 106 $^{\circ}\text{C}$, and then fully grow on the surface and remain stable the sample is cooled down. ITO thin film was deposited by 20W RF sputtering with 4 mTorr pressure. The sample was heated on the hotstage with the heating rate of 10 $^{\circ}\text{C}/\text{min}$ from room temperature to 120 $^{\circ}\text{C}$. The scale bar is 100 μm .

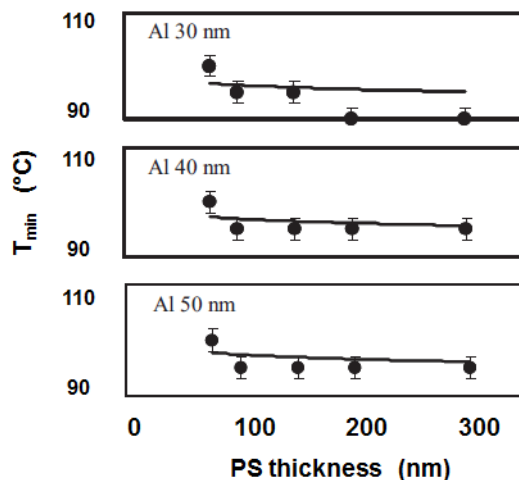


Figure 6.5. “Minimum annealing temperature” (T_{\min}) measured for buckles as a function of PS thicknesses for different Al thicknesses (30, 40 and 50 nm).⁶

Al is widely used as the top electrode in organic solar cells. Buckling in Al/PS layers has also studied and the trends observed are consistent with our findings in ITO/PS laminates. The wavelength and the amplitude (A) of isotropic buckles using different thicknesses for the capping film and the PS layer have been investigated and the corresponding aspect ratio (AR), defined as λ/A , has been evaluated. The AR of isotropic buckles by post-annealing of bilayer films is 0.04~0.06 with different capping films (ITO in our cases) and PS thicknesses (**Figure 6.6**).¹⁴

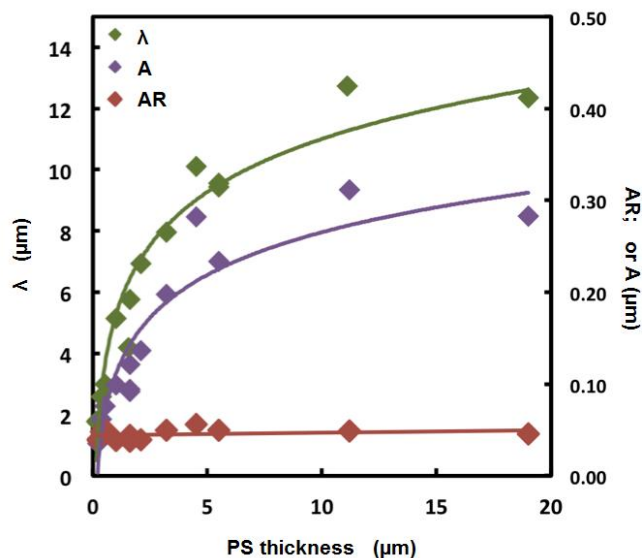


Figure 6.6. The wavelength (λ), amplitude (A) and aspect ratio (AR) as a function of PS thicknesses. The ITO capping film thickness is 40 nm.¹⁴ The solid lines are meant to guide the eye.

Two-generations of isotropic buckles have been observed in ITO/PS thin films when the PS layer was heated to 160 °C during the deposition of ITO. Small isotropic buckles are formed on as-sputtered ITO/PS samples; those form due to thermal expansion mismatch between the ITO and the heated PS substrate during the sputtering (**Figure 6.7a**). Large isotropic buckles are formed on heating ITO/PS samples after sputtering is completed (**Figure 6.7b**). In the final topography, smaller buckles are superimposed on large buckles, which can be easily observed from the zoomed image in **Figure 6.7b**.

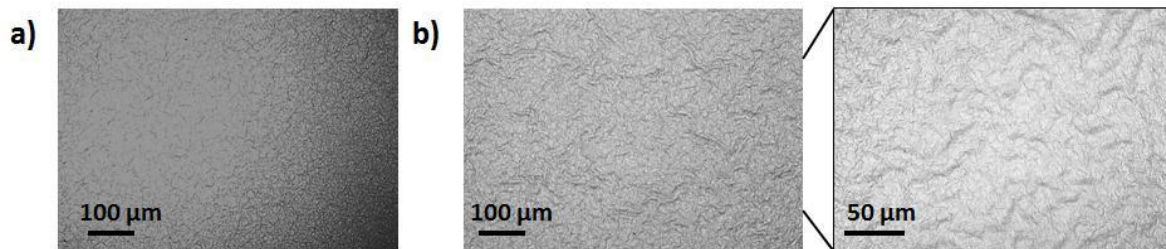


Figure 6.7. Optical microscopes images of thermal buckles of ITO (40 nm)/PS (1.5 μm) on the glass substrate: (a) as-sputtered buckles due to thermal expansion mismatch when sputtering at 160 $^{\circ}\text{C}$; and (b) two generations of buckles after annealing at 120 $^{\circ}\text{C}$ followed by sputtering.

Compared with ordered buckled morphologies prepared by mechanical stretching, isotropic buckles in metal/polymer thin films offer a simple way to achieve buckled surface topographies because the procedure to produce the latter structures only requires annealing the samples above the T_g of the polymer support and subsequent cooling, during which the buckles form spontaneously. Moreover, this buckling method on thin films is compatible with planar processing such as direct deposition (e.g., sputtering, evaporation, spin-coating) and printing techniques. Therefore, buckling represents a simple fabrication method and does not require any complex processing steps beyond those already used to produce planar layers. For example, buckles can be applied as a promising structure for light trapping in organic photovoltaics (OPV) which has been studied to fabricate OPV on buckled ITO/PS substrate. The most prominent results are summarized in **Appendix A** of this dissertation.

6.4 Effort to Enhance Limited Aspect Ratio of Isotropic Buckles

Despite the aforementioned advantages of this buckle-forming method some drawbacks exist. One that is most pertinent to applications as light-trapping devices is the

rather low AR of the buckled morphologies (AR~0.05). Although OPV devices built on buckled surfaces have demonstrated enhanced light harvesting relative to flat geometries (see **Appendix A**), buckled devices with higher efficiency are desired that could be formed by increasing the AR of the buckles. Therefore, new ways to obtain high AR of isotropic buckles need to be explored.

Recently, enhanced AR up to ~2.5 has been reported by depositing amorphous carbon films on a PDMS substrate using glancing angle deposition;¹⁵ high AR can be achieved by using deposition angle of 75 °. However, this technology employs an expensive deposition method.¹⁴

Solvent swelling can also be employed to enhance the AR of buckles since good solvent can induce large strains due to the swelling. This approach has been studied before by our co-worker using toluene and phenol in PDMS substrate to achieve AR of up to ~0.4.¹⁴ However, application of organic solvents is not always amendable for some applications and technologies.

Pre-strained polymer sheets are excellent substrates for generating buckles due to their stored strain. For example, Shrinky Dinks[®] (SD) is a commercial product commonly used as a toy for children. It constitutes a pre-strained PS sheet and shrinks in-plane by 50%~60% during heating over its T_g (e.g., 3-5 min, over 120 °C).⁹ Khine's group has recently reported on the utilization of SD in fabricating deep and rounded microfluidic channels (**Figure 6.8**).^{9,16}

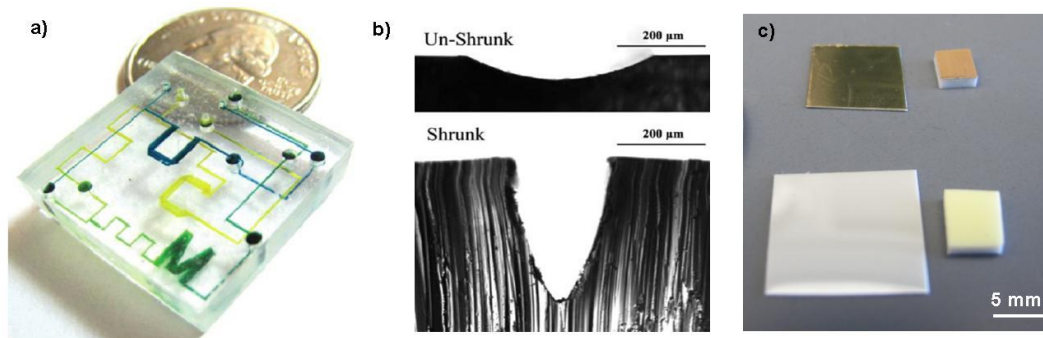


Figure 6.8. a) 3D microfluidic mixer made by Shrinky Dinks[®];⁹ b) cross-sections of the microfluidic channels before and after shrinkage⁹ and c) photograph of gold (top) and ITO (bottom) coated SD before and after annealing.

Thin films of gold (40 nm) with a thin adhesion layer of Cr (≈ 5 nm), Ag (70 nm) and ITO (40 nm) were deposited on SD films by sputtering. The bilayer samples shrunk when annealed at 120 °C for 30 min on the hotplate. To minimize warping of the samples, additional weight, such as a thick glass slide or metal sheet, was put on the top of the samples. The “crumbled” surfaces of gold and ITO-coated SD were formed and imaged by scanning electron microscopy (SEM) (**Figure 6.9**). Shrunken ITO/SD layers have demonstrated enhanced light absorption in the visible wavelength due to the “crumbled” surface (**Figure 6.10**). However, the shrinkage was very high, making SD challenging to maintain adhesion to the top layer between SD and the coated film.

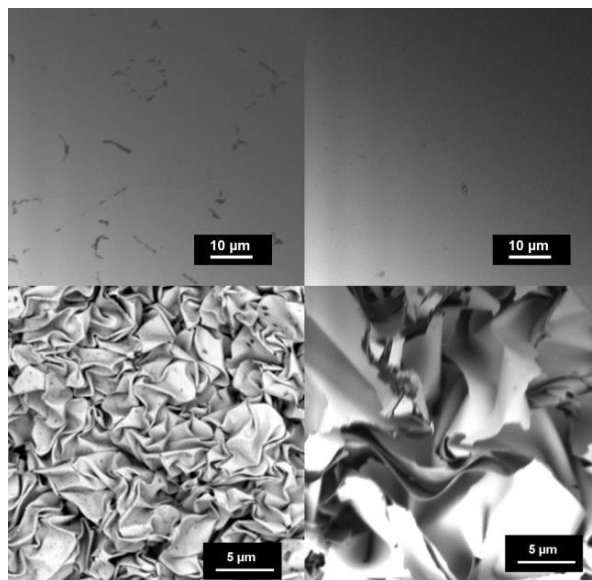


Figure 6.9. SEM images of “crumbled” surfaces of gold (thickness ~40 nm) with an underlying chromium (thickness ~5 nm) layer (left column) and ITO (thickness ~40 nm) (right column) on SD before and after annealing at 120 °C for 30 min on a hotplate.

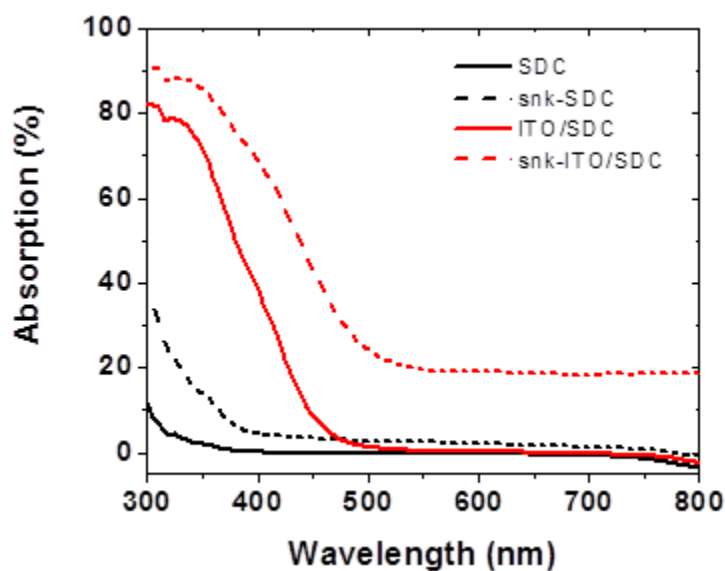


Figure 6.10. Absorption spectra of plain SD (SDC), shrunken SD (snk-SDC), ITO coated SD (ITO/SDC), and shrunken ITO coated SD (snk-ITO/SDC). The ITO film is 40 nm thick, and shrinking occurs after annealing at 120 °C for 30 min on a hotplate.

Here, we explore a promising new approach employing a different driving force (i.e., electric field) to amplify isotropic buckles due to thermal expansion mismatch between layers, which requires no solvent and amplifies the buckles formed on the original samples. This will be described in the following section

6.5 Buckles with Enhanced Aspect Ratio via Electric-field Amplification

6.5.1 Hypothesis of Electric-field Amplification

Electric field (E-field) amplification of buckles is another strategy to increase the low aspect ratio (0.04~0.06) of thermally-formed isotropic buckles. Electric field is an attractive destabilizing force that can induce thin film instability readily.¹⁷ Electrohydrodynamic patterning using electric fields has been utilized to form high aspect-ratio structures (e.g., pillars) out of molten polymer films or liquids with an air gap (or another polymer, e.g., polystyrene) sandwiched between two rigid electrodes.¹⁷⁻²³ For example, a pattern formation induced by applying an electric field on a dielectric liquid-like film, as illustrated in **Figure 6.11**. A strong electric field gradient forms across the dielectric medium to induce destabilizing electrostatic forces, which overcome the surface tension of the film to induce film undulations of a characteristic wavelength and its amplification between air and the polymer to form a 3D structure.¹⁷

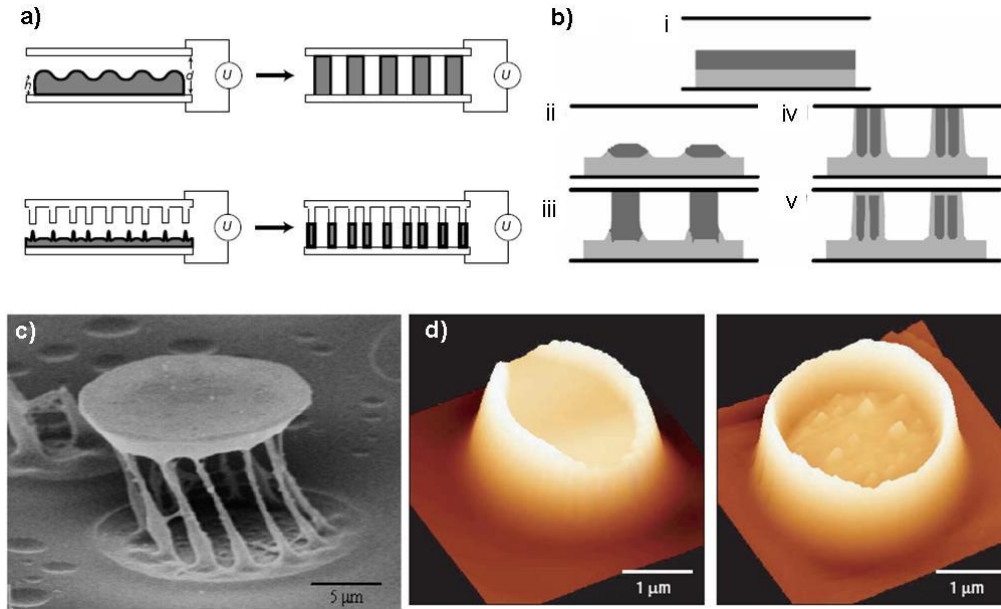


Figure 6.11. a) Schematic depicting 3D structures induced by electric field at polymer/air single layer;¹⁷ b) schematic of 3D structures induced by electric field at polymer/polymer/air trilayer¹⁸ and SEM images of c) cage-type and d) column structures made of poly(methyl methacrylate) (PMMA) while removing PS by cyclohexane with electric field on PS/PMMA/air trilayer with different electrode set-up.^{18,20}

Hierarchical surface topography on polymeric substrates can be induced by superimposing thin-film instability with two distinct buckled mechanisms and topographies. While isotropic buckles form as a result of relaxation of compressive stresses due to the mismatch in thermal expansion between the capping metal and bottom substrate during heating, as discussed above, we propose that “e-field buckles” will be formed by electrohydrodynamic flow induced by electric field. The arrangement will be such that the thermal buckles will be superimposed on top of the “e-field buckles”, which will have a larger wavelength than the thermal buckles. One would expect that the AR will increase relative to

cases involving only thermal buckles due to concurrent relaxation of thermal and electromechanical stresses in the specimen.

Electric field induced buckles have been reported earlier for gold/acrylate elastomer/ITO multilayers.^{24,25} Large wavelengths (10~30 μm) can be triggered, which depend on the thickness of the elastomer film. The critical voltage needed to initiate the buckles, which varies from 60 to 950 V, depends on the thickness of the elastomer film. Here, we propose to use electric field in conjunction with thermal annealing in Al/PS bilayers to form buckles featuring multiple wavelengths. The PS film serves as a liquid-like capacitor above T_g and the Al also functions as an electrode. The buckles start to form when the sample is heated above T_g , and the buckles are expected to be amplified under the induced electric field gradient.

6.5.2 Experimental

As described in **Figure 6.12**, thermally isotropic buckles were first induced on Al/PS thin films. P-type silicon (100) with 150 nm of thermally-grown oxide layer forms the bottom substrate. The oxide layer acts as an insulating layer and avoids the breakdown of the polymer film and the electric shortage. The substrates were cleaned in acetone and isopropanol sequentially by in 10 minute long ultrasonic treatment, followed by 10 minutes of ultraviolet ozone treatment. Polystyrene pellets ($M_w = 230$ kDa, $M_n = 140$ kDa) were dissolved in toluene to prepare polymer solutions of different concentrations. Filtered polystyrene thin films with different thicknesses were formed by spin-coating the solutions on silicon substrates (**Table S1**). The spin-coated films were annealed at 110 $^{\circ}\text{C}$ for 3 hours on a hotplate to remove any residual solvent. Patterned Al films (50 and 100 nm), acting as

the top electrode (anode), were sputtered by DC Ar sputtering system (power =30 W) by using a homemade PDMS mask. The base pressure of the chamber for sputtering was $<1 \times 10^{-5}$ Torr and the pressure during the sputtering was 6 mTorr. The back side of the oxidized silicon was scratched by a diamond scribe to remove the oxide layers and create the back electrode (cathode). Connecting wires were glued to the top and bottom electrodes by applying silver paint (Electron Microscopy Sciences). The sample was then placed on the hotstage, whose temperature and heating rate were controlled. The voltage was applied by Keithley 2400 source meter. The real-time investigation of buckling formation and amplification was observed under optical microscope through the open hole in the hot-stage.

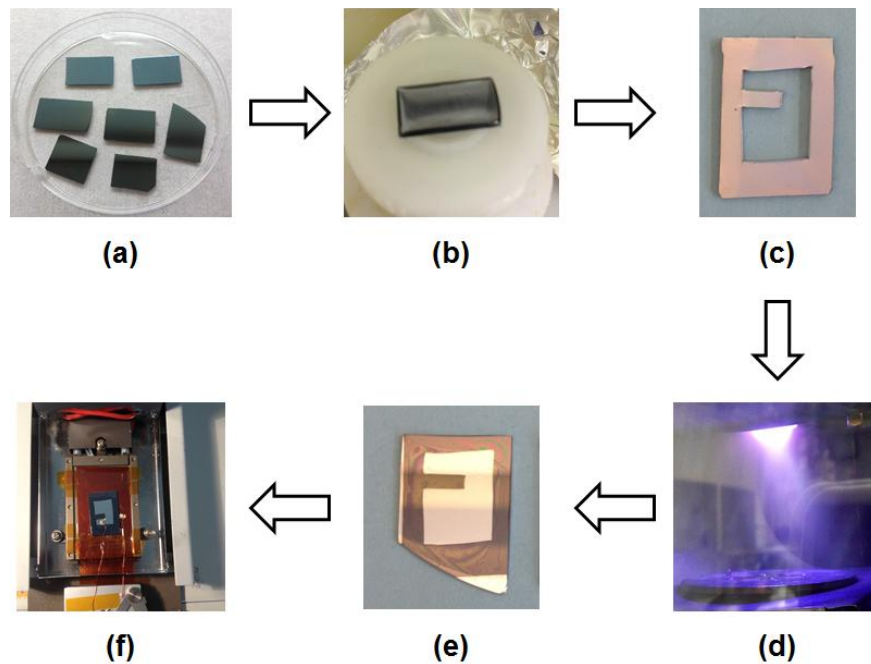


Figure 6.12. Experimental procedure leading to: (a) oxidizing and cleaning silicon substrates; (b) spin-coating PS films and annealing; (c) typical PDMS mask used for sputtering; (d) Al sputtering on masked PS films; (e) as-sputtered Al/PS/Si samples; and (f) assembling samples with the e-field connections.

6.5.3 Results and Discussion

The Al/PS sample was heated at the rate of 5 °C/min without applying electric field, and isotropic buckles occurred at about 106 °C, close to T_g of polystyrene (≈ 100 °C). Here, we call these isotropic buckles before applying e-field “thermal buckles” (**Figure 6.13b**) in order to differentiate them from buckles formed during the application of e-field (**Figure 6.13c**). After reaching 170 °C, a constant electric field was applied on the sample to investigate the time evolution of e-field buckles under optical microscope (**Figure 6.14**). E-field buckles are induced in 4 seconds under a e-field of ~ 35 V/ μm . E-field buckles quickly grow and expand to the whole observed area within the first 2 minutes of annealing and e-field treatment.

E-field buckles have been studied on PS films with different thicknesses while keeping a constant e-field. For thin PS films (thickness ~ 0.5 μm), e-field buckles have been observed only after a long annealing time (~ 7 hrs) as shown in **Figure 6.15a, b**. When using thicker PS films (thickness ~ 5 μm) the e-field buckles developed faster (~ 2 minutes). The absence of e-field buckles for thin PS film can be explained by insufficient amount of PS to induce e-field buckles. As shown by typical line scans for both thermal buckles and e-field buckles in **Figure 6.15c, d**, the wavelength of e-field buckles is about one order of magnitude larger than that of thermal buckles; and amplitude (height in the **Figure 6.15c,d**) of e-field buckles is about two orders of magnitude higher than that of thermal buckles. Therefore, enhanced AR can be achieved by applying e-field as we described.

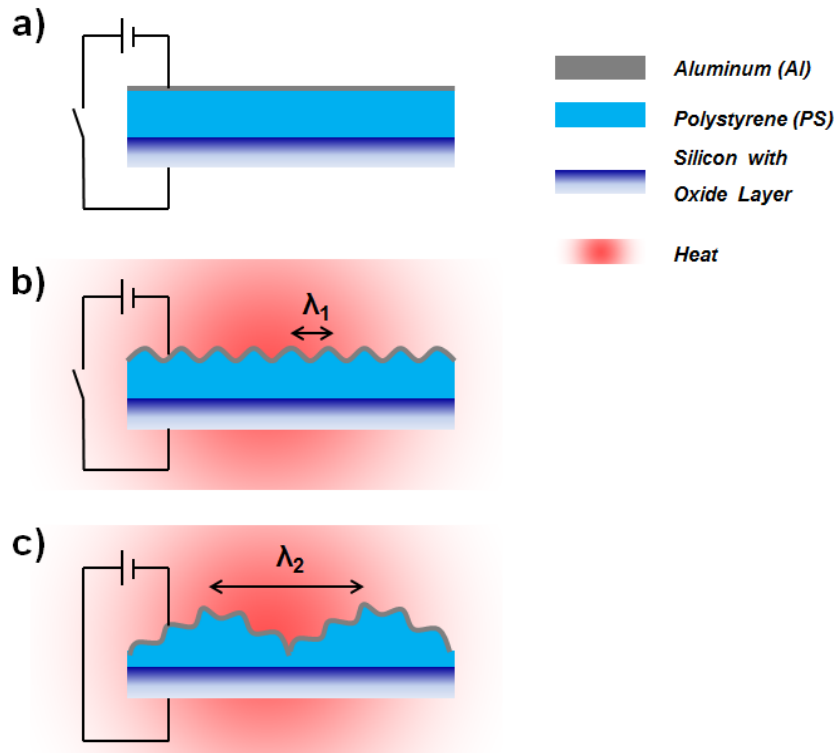


Figure 6.13. Schematic of the experimental set-up: (a) original planar Al/PS thin films on silicon substrate with thermal oxide layer; (b) thermal buckles (λ_1) formed via heating the sample on the hot-stage without e-field; and (c) e-field buckles (λ_2) formed by applying e-field.

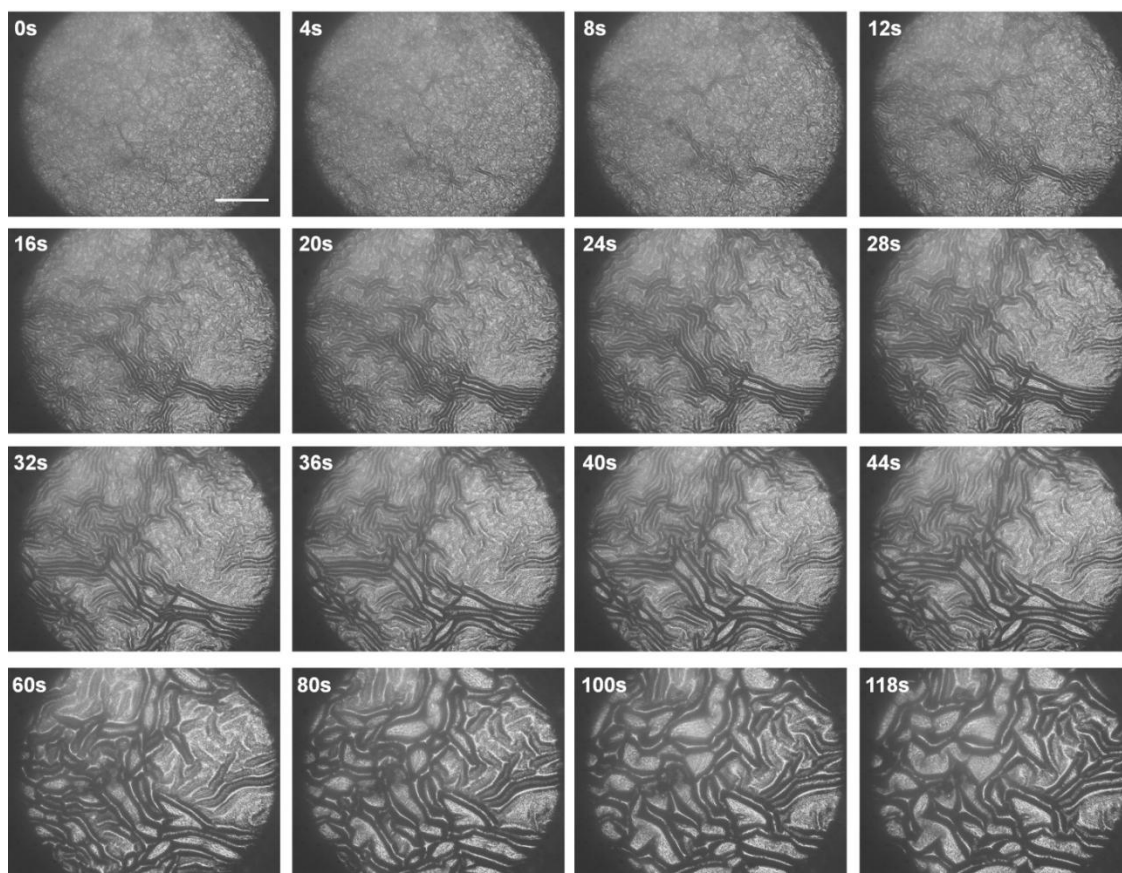


Figure 6.14. Time evolution of buckles grown under a constant voltage (175 V) for a sample of Al (50 nm)/PS (5 μm). The scale bar is 500 μm .

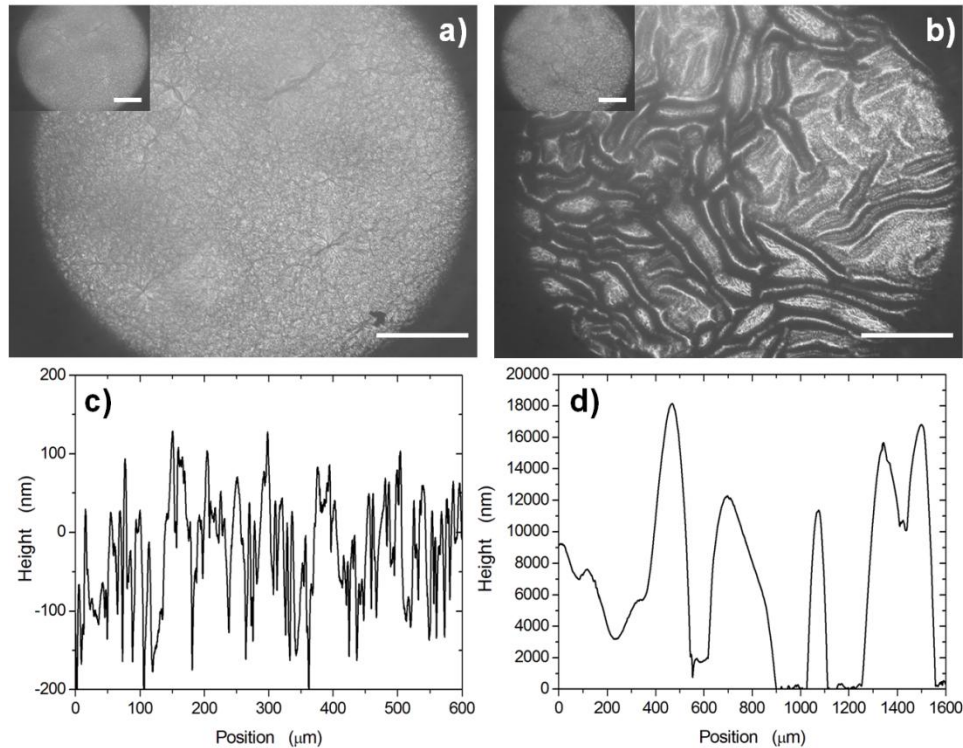


Figure 6.15. Optical microscopy images of buckle topographies from samples with different PS thicknesses by applying e-field ($\sim 35 \text{ V}/\mu\text{m}$): (a) $0.5 \mu\text{m}$ thick PS film after 7 hours and (b) $5 \mu\text{m}$ thick PS film after 1 minute. The inset images are initial thermal buckles. The Al film thickness is 50 nm . The scale bars are $500 \mu\text{m}$. Typical profilometry line scans for (c) thermal buckles on $0.5 \mu\text{m}$ thick PS film and (b) e-field buckled on $5 \mu\text{m}$ thick PS film.

6.6 Summary

We studied isotropic buckling in metal (or oxide)/PS laminates resting on flat solid substrates. We established that the wavelength and amplitude of the buckles can be controlled by varying the thicknesses of the metal (or oxide) and PS films. The major finding of this study is that complex buckles with high aspect ratios can be generated by applying electric field across the metal(or oxide)/PS laminates. Further research aiming at establishing the contribution of the thicknesses of the top and PS layers, strength of electric fields and other processing conditions to the morphology development is needed.

6.7 Acknowledgements

I thank Dr. Sharvil Desai for his contribution to the study of e-field buckles. I thank Dr. Michelle Casper for depositing ITO on PS substrates to investigate two-generation isotropic buckles. I thank Mr. Kazi Sadman, a summer REU student, for his effort in preparing the samples and conducting the e-field experiments. I also thank Dr. Jon-Paul Maria and his group for their generous help and access to the sputtering system for Al deposition, as well as Dr. Gregory Parsons's lab to allow me to use his SEM and profilometry set ups. In addition, I would like to thank Dr. Xuanhe Zhao and Qiming for the discussion about the mechanism of e-field buckling and modeling.

References

1. Genzer, J. & Groenewold, J. Soft matter with hard skin: From skin wrinkles to templating and material characterization. *Soft Matter* **2**, 310 (2006).
2. Bowden, N., Brittain, S., Evans, A. G., Hutchinson, J. W. & Whitesides, G. M. Spontaneous formation of ordered structures in thin films of metals supported on an elastomeric polymer. *Nature* **393**, 146–149 (1998).
3. Efimenko, K., Finlay, J., Callow, M. E., Callow, J. A. & Genzer, J. Development and Testing of Hierarchically Wrinkled Coatings for Marine Antifouling. *ACS Appl. Mater. Interfaces* **1**, 1031–1040 (2009).
4. Efimenko, K. *et al.* Nested self-similar wrinkling patterns in skins. *Nat. Mater.* **4**, 293–297 (2005).
5. PJ Yoo, K. S. Physical self-assembly of microstructures by anisotropic buckling. *Adv. Mater.* **14**, 1383–1387 (2002).
6. Okayasu, T., Zhang, H.-L., Bucknall, D. G. & Briggs, G. A. D. Spontaneous Formation of Ordered Lateral Patterns in Polymer Thin-Film Structures. *Adv. Funct. Mater.* **14**, 1081–1088 (2004).
7. Yoo, P. J., Park, S. Y., Kwon, S. J., Suh, K. Y. & Lee, H. H. Microshaping metal surfaces by wave-directed self-organization. *Appl. Phys. Lett.* **83**, 4444 (2003).
8. Yoo, P. J. & Lee, H. H. Complex Pattern Formation by Adhesion-Controlled Anisotropic Wrinkling. *Langmuir* **24**, 6897–6902 (2008).
9. Chen, C.-S. *et al.* Shrinky-Dink microfluidics: 3D polystyrene chips. *Lab. Chip* **8**, 622–624 (2008).
10. P. J. Yoo, H. H. L. Morphological Diagram for Metal/Polymer Bilayer Wrinkling: Influence of Thermomechanical Properties of Polymer Layer. *Macromolecules* **38**, 2820–2831 (2005).

11. Lin, J.-Y. *et al.* Thickness Effects on the Thermal Expansion Coefficient of ITO/PET Film, *Imaging Methods Nov. Mater. Challenging Appl. Vol. 3* (Jin, H., Sciammarella, C., Furlong, C. & Yoshida, S.) 353–358 (Springer New York, 2013).
12. Park, S. K., Han, J. I., Kim, W. K. & Kwak, M. G. Deposition of indium–tin-oxide films on polymer substrates for application in plastic-based flat panel displays. *Thin Solid Films* **397**, 49–55 (2001).
13. Zhang, H.-L., Okayasu, T. & Bucknall, D. G. Large area ordered lateral patterns in confined polymer thin films. *Eur. Polym. J.* **40**, 981–986 (2004).
14. Casper, M. D. *The Origins of Buckle Formation in Vapor Deposited Oxides on Polymers*. Dissertation (North Carolina State University,, 2011).
15. Ahmed, S. F., Rho, G.-H., Lee, K.-R., Vaziri, A. & Moon, M.-W. High aspect ratio wrinkles on a soft polymer. *Soft Matter* **6**, 5709 (2010).
16. Grimes, A. *et al.* Shrinky-Dink microfluidics: rapid generation of deep and rounded patterns. *Lab. Chip* **8**, 170 (2008).
17. Schäfer, E., Thurn-Albrecht, T., Russell, T. P. & Steiner, U. Electrically induced structure formation and pattern transfer. *Nature* **403**, 874–877 (2000).
18. Dickey, M. D. *et al.* Novel 3-D Structures in Polymer Films by Coupling External and Internal Fields. *Langmuir* **22**, 4315–4318 (2006).
19. Dickey, M. D. *et al.* High-aspect ratio polymeric pillar arrays formed via electrohydrodynamic patterning. *J. Mater. Sci.* **43**, 117–122 (2007).
20. Morariu, M. D. *et al.* Hierarchical structure formation and pattern replication induced by an electric field. *Nat. Mater.* **2**, 48–52 (2002).
21. Pease, L. F. & Russel, W. B. Electrostatically induced submicron patterning of thin perfect and leaky dielectric films: A generalized linear stability analysis. *J. Chem. Phys.* **118**, 3790 (2003).

22. Wu, N., Pease, L. F. & Russel, W. B. Toward Large-Scale Alignment of Electrohydrodynamic Patterning of Thin Polymer Films. *Adv. Funct. Mater.* **16**, 1992–1999 (2006).
23. Yang, M. Self Assembly of Polymer Structures Induced by Electric Field. *J. Assoc. Lab. Autom.* **8**, 86–89 (2003).
24. Huang, R. Electrically induced surface instability of a conductive thin film on a dielectric substrate. *Appl. Phys. Lett.* **87**, 151911 (2005).
25. Van den Ende, D., Kamminga, J.-D., Boersma, A., Andritsch, T. & Steeneken, P. G. Voltage-Controlled Surface Wrinkling of Elastomeric Coatings. *Adv. Mater.* **25**, 3438–3442 (2013).
26. Hall, D. B., Underhill, P. & Torkelson, J. M. Spin coating of thin and ultrathin polymer films. *Polym. Eng. Sci.* **38**, 2039–2045 (1998).

Supporting Information

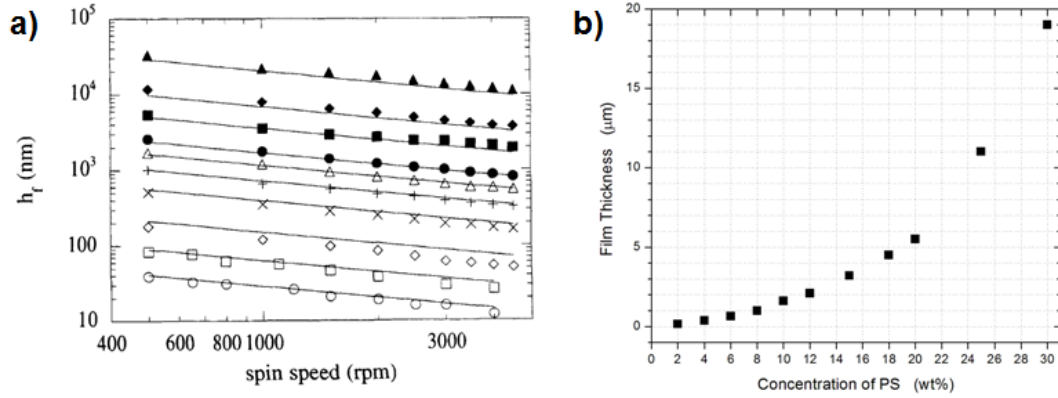


Figure S6.1. Film thickness as a function of the concentration of polystyrene stock solution (wt%) in toluene and spin speed for coating process based on (a) results from literature;²⁶ open circles represent 0.5 wt%; open square 1 wt%; open diamond 2 wt%; “X” represents 4 wt%; “+” represents 6 wt%; open triangle represents 8 wt%; solid circles represent 10 wt%; solid squares represent 15 wt%; solid diamond represent 20 wt% and solid triangles represent 30 wt%, and (b) our experimental results.¹⁴

Table S6.1. Spin conditions used to spin-coat PS films in our experiment.

PS concentration in toluene (wt%)	Film thickness (μm)	Spin speed (rpm)	Spin time (s)
2	0.15	1000	30
4	0.37	1000	30
6	0.65	1000	30
8	1	1500	60
10	1.6	1500	60
12	2.1	1500	60
15	3.2	1500	60
18	4.5	1500	60
20	5.5	1500	60
2	<i>0.2</i>	<i>500</i>	<i>30</i>
4	<i>0.53</i>	<i>500</i>	<i>30</i>

(Italic data is not included in Figure S6.1).

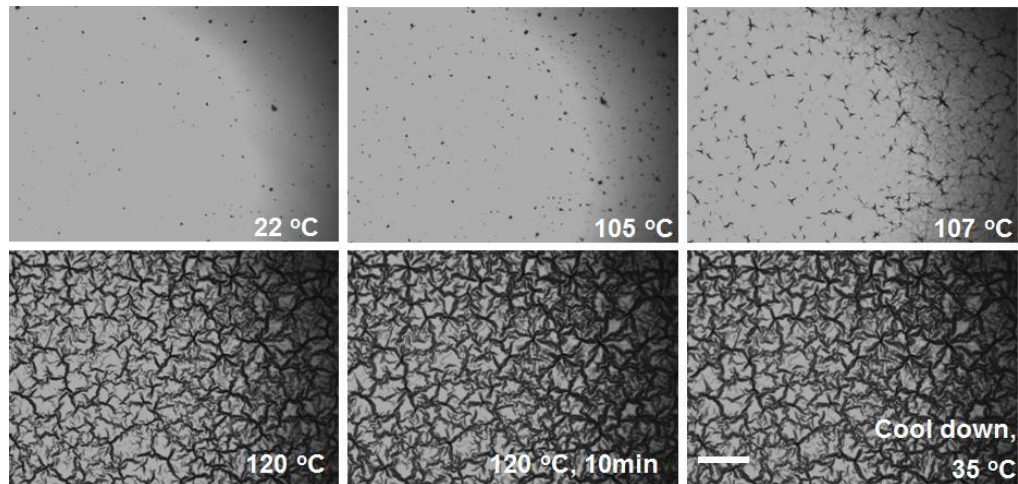


Figure S6.2. Real-time investigation of isotropic buckles based on ITO (40 nm)/PS (500 nm) bilayer on a silicon substrate. The buckles start to grow around temperature of 107 °C, and then fully grow on the show surface and remain when the sample is cooled down. ITO thin film is deposited by 20W RF sputtering with 4 mTor process pressure. The sample is heated in the hot-stage with the heating rate of 10 °C/min from room temperature to 120 °C. The scale bar is 100 μm .

CHAPTER 7

Summary and Future Outlook

7.1 Summary

This dissertation describes the shape programming of stimuli-responsive 2D polymeric materials to convert them from 2D planar forms to 3D shapes. As illustrated in Figure 1.1 in Chapter 1, the work presented here can be categorized into two broad categories: 1) using 2D planar geometries to achieve out-of-plane folding, bending, or rolling by employing “hinges” or managing strain; and 2) inducing surface topographies on 2D sheets. The general premise that shape defines the function for many materials motivates this work. In addition, 2D patterning techniques can be efficiently employed as high throughput manufacturing processes (e.g., semiconductor processing). Specifically, in this Ph.D. dissertation we discuss several self-folding strategies used to generate pre-programmed 3D structures and describe the formation of buckled surface topographies in 2D sheets.

Self-folding is a deterministic self-assembly approach that causes a 2D template with pre-defined hinges to fold into 3D shapes by employing external stimuli. There is increased interest in numerous emerging applications involving actuation, packaging, and reconfigurable devices that utilize self-folding by employing a variety of different driving forces and active materials. Compared with common design methods for self-folding, which require multistep complex fabrication procedures or pre-programming, we developed a simple, responsive approach to realize self-folding of homogeneous pre-strained polymer sheets by employing conventional 2D printing methods. Our approach uses a desktop printer to pattern ink as hinges that locally absorb light from a uniform light source and convert it to heat. This heat causes a local relaxation in the pre-strained sheets and induces folding. Various 3D structures can be manufactured with this method by choosing an appropriate

combination of inked pattern, line width, light source, and support temperature. It was demonstrated that the onset time of folding decreases and the maximum bending angle increases with increasing hinge width or support temperature. A model based on heat transfer captures effectively the time scale of the onset of folding as well as the bending angle measured experimentally.

The out-of-plane folding of pre-strained polymer sheets relies on a temperature gradient that causes the strain in the sheet to recover non-uniformly across the sheet thickness. The study of uniform shrinkage of flat pre-strained polymer sheets at constant temperatures and constant heating rates provides a simple geometric model that relates the bending angle to the uniform shrinkage and width of the hinges printed by desktop printer on the sheet. The appeal of this work is that it correlates the folding dynamics with macroscopic shrinkage behavior of these polymer sheets without the need of detailed understanding of thermo-mechanical properties of the polymer.

To extend this preliminary work on self-folding to different light sources and ink absorbers, we studied the effect of the ink type and the source of light by printing inks with different widths and colors and by utilizing various light sources (i.e., IR, halogen, and LED). The application of LED sources is novel and exciting because the light absorption (and thus the hinge response) can be tailored by utilizing hinges with different colors and widths. Moreover, unlike IR or halogen light, the LED-triggered folding does not suffer from distortion of the plain sheet during folding because the non-patterned polymer does not absorb significant light in visible wavelengths used. Selective absorption of the LED light of a given wavelength by the hinges featuring different colors facilitates sequential self-folding.

To this end, varying the color of the hinge and the wavelength of the LED light source enables sequential self-folding. The ability to program folding pathways by employing various LED sources and hinges of different colors (and width) can potentially be utilized in fabricating grippers and actuators, and can be employed in realizing complex origami structures.

In addition, we demonstrated that hinge-free folding can be accomplished by utilizing a focused laser beam that initiates the folding mechanism in planar polymer sheets. The key process parameters that govern folding in this case involve laser power, power intensity, and beam width. It was found that folding occurs only above a certain laser power threshold required to compensate for the heat loss to the material outside of the focused laser beam. This appealing approach requires no patterning of pre-defined hinges, the folding can be scalable and compatible with high throughput processing, and diverse patterns can be programmed by choosing the appropriate scanning path of the laser.

Buckling (or “wrinkling”) is a common phenomenon found in nature. Buckled surfaces typically form when a thin rigid film is placed on top of a thick elastic substrate and the bilayered laminate is exposed to an external stress (thermal expansion or mechanical stretching). Tailoring surface topography (either uni-directional or isotropic) by invoking buckling instabilities is appealing for many applications such as anti-fouling coatings, microfluidic devices, reversible adhesive surfaces, optical sensors, and many others. The formation of buckles was studied using various metal top films (e.g., Al, ITO) and support substrates (e.g., PDMS, polystyrene) to investigate the impact of thicknesses of the two films on buckle wavelengths and amplitudes. Motivated by the promising means of increasing light

trapping in “rough” surfaces and thus improving the performance of organic photovoltaic (OPV) devices based on buckled substrates, we demonstrated an increase in efficiency for OPV devices built on buckled substrates and identified challenges associated with making buckled surfaces with high aspect ratio (defined as the ratio of the buckle amplitude and buckle wavelength). We explored several strategies to enhance the aspect ratio for isotropic buckles. Preliminary results pertaining show that the application of an electric field during thermal annealing of the bilayered metal(oxide)/polymer laminates amplifies the extent of buckling instabilities (and ultimately increasing the aspect ratio) of isotropic buckles.

7.2 Future Outlook

This dissertation describes two simple approaches to convert planar sheets to 3D shapes and surface topography, self-folding and buckles formation.

Implementation of self-folding is challenged by the complexity of fabrication, and the response time for self-folding. The approach developed in Chapter 2 is distinguished by its simplicity and the ability to convert 2D templates to diverse 3D geometries in a fast manner using inexpensive homogeneous polymer sheets and a standard desktop printer.

This simple method developed for self-folding outlined in Chapter 2 can be extended to other materials or mechanism utilizing different light sources, different ink absorbers, various film thicknesses, and pre-strained polymer sheets with different chemical compositions, different degrees of pre-strain, or with different glass transition temperatures. Chapters 4 and 5 discussed the use of focused laser or LEDs possible light sources to induce self-folding. Self-folding was demonstrated using hinges with color inks and different

percentages of greyscales. To extend the usefulness of the self-folding mechanism described, future work should consider utilizing different polymer materials with different initial strain states (e.g. degree of pre-strain or strain homogeneity) and material thicknesses. For example, large bending angles can be readily achieved when using thin pre-strained sheets and high degree of pre-programmed strain. Tailoring those attributes can offer much more freedom and control in achieving self-folding. Although we focus on thermal actuation solely, various other stimuli such as Joule-heating, microwave heating, or solvent swelling can be explored for self-folding of pre-strained polymer sheets.

Another major challenge in self-folding research is associated with the control of folding/unfolding pathways which can lead to sequential/programmed folding. Chapter 5 demonstrated sequential self-folding employing various color inks or different percentage of greyscales. This feature can be further enhanced by employing alternative heat sources (e.g., LEDs with different wavelength) with sufficient power and large uniform irradiation area to generate complex geometries utilizing sequential folding.

Obtaining folded geometries in high fidelity (i.e., with few defects such as overfolding or underfolding) also presents unique challenges. Some control can be achieved by adjusting the properties of the hinges (i.e., color and width). Utilizing sequential folding can be beneficial in this respect as one could, in principle, alleviate issues associated with preferential folding at vertices that governs concurrent/simultaneous folding. By programming the times scales and degree of folding by invoking the aforementioned principle of sequential folding it should be capable of producing complex 3D patterns.

A more thorough understanding of microscopic thermo-rheological properties of polymer sheets and the impact on the folding mechanism is also needed. A model featuring finite element analysis in conjunction with detailed rheological characteristics of polymer sheets (including temperature and frequency dependence of the storage and loss moduli) will help extend this study beyond the simple (albeit quite effective) macroscopic geometric model of folding. The combination of finite element computer simulations with experimental results will thus provide a new comprehensive insight that can be employed in designing the 2D patterns that lead to desired 3D shapes.

As for the second strategy of employing buckled topographies in 2D sheets, control of the characteristics of wrinkles has been well studied in preceding work. One challenge associated with buckled surface is better control of the aspect ratios. This Ph.D. dissertation has offered one unconventional method leading to the enhancement of the aspect ratio of the buckles by employing electro-dynamic forces acting during thermal annealing of polymer sheets. It has been documented that this method results in multi-scale buckled topographies featuring thermal buckles resting on top of electro-hydrodynamically formed buckles. While the preliminary results described in this dissertation are promising, one needs to better characterize the length scales and orientations of the resulting topography and address the interplay between the two patterns by fine-tuning the processing conditions (i.e., temperature, films thicknesses, applied voltage, etc).

Selection of the ideal base polymer and corresponding processing conditions for this method presents another challenge. For example, applying PS as the base layer requires annealing temperatures around 100 °C, a temperature that may be too high for preparing

OPV devices because some organic molecules employed in the manufacturing process may degrade under those conditions. Therefore, polymer substrates with lower glass transition temperature are desired in some cases.

A thorough comprehension of the materials and stimuli strategies to convert 2D planar sheets to 3D shapes or 2D plane with surface topography is highly desired because those fundamental studies can eventually provide a practical guide to the manufacture of reconfigurable or adaptive electronic or optical devices with predictable and controllable function transformation. Although our initial efforts demonstrated the possibility of constructing self-folding origami microstrip antennas,¹ different types of functional devices utilizing self-folding or spontaneous buckling formation should be further explored as a potential future goal.

1. Hayes. G.J., Liu Y., Genzer J., Lazzi G., Dickey M.D., *IEEE Transactions on Antennas & Propagation*, submitted.

Appendices

Appendix A

Fabrication of Organic Photovoltaics (OPV) on Buckled Substrate

Introduction to OPV and Light Harvesting in OPV

The development of clean, renewable sources of energy is important for national security, economic growth, and environment protection due to increasing concern regarding energy derived from fossil fuels.¹ Photovoltaic (PV) technology, which transforms solar energy into electric power, is a particularly attractive source of clean energy because of the amount of energy provided by the sun ($\approx 1000 \text{ W/m}^2$ at the surface of the earth at the equator).²⁻⁴

E. Becquerel firstly reported the PV effect in 1839, but it was not materialized into a commercial device until the 1950s.² The principle behind the PV effect is simple: when the energy of an incident photon ($h\nu$) is larger than the band gap energy of the semiconductor, the photon can generate a positive charge (hole, h) and negative charge (electron, e) pair, called an h-e pair. To generate a photocurrent, the hole and the electron must be separated and transported to two opposite electrodes driven by an internal electric field.⁵

Organic photovoltaics (OPVs) use typically small dye molecules or semiconductor polymers.³ Photogeneration in OPVs produces excitons (mobile excited states) at the site of the electron donor (a molecular species that donates electrons),^{3,6} as shown in **Figure A.1**. Excitons can be separated into holes and electrons at a heterojunction, which is the interface between two semiconductor materials with different electron affinities and band gaps. Upon separation, free holes and electrons can be transported to opposite electrodes to generate photocurrent.²

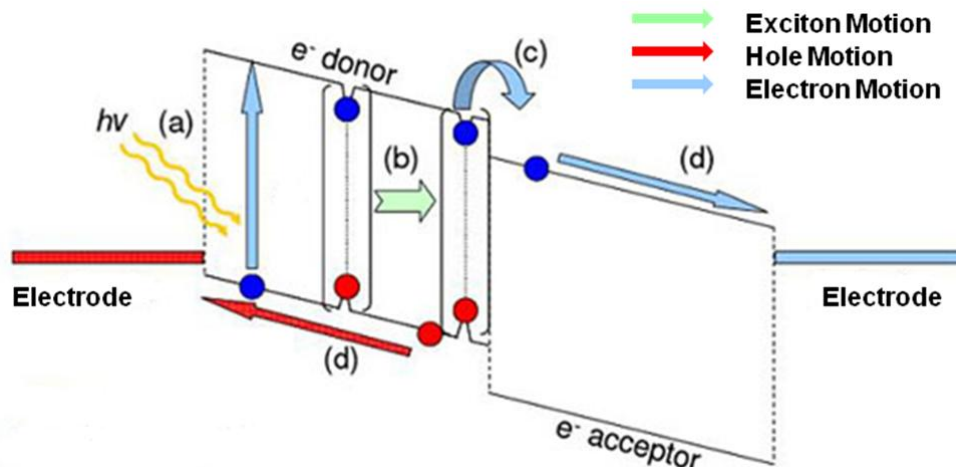


Figure A.1. Schematic of photocurrent generation in an OPV.⁸ (a) photon absorption; (b) exciton diffusion; (c) separation of an exciton at heterojunction and (d) transport of charge carriers (electrons and holes).

Compared to inorganic PVs, OPVs are attractive because they are, in principle, inexpensive, light-weight and compatible with high throughput processing on flexible plastic substrates.^{3,8,9,10} OPVs are expected to be low-cost because the organic materials can be deposited at room temperature using high throughput roll-to-roll processing.^{11,12} Because the processing temperature for the deposition methods is low, OPVs are compatible with plastic substrates for flexible devices.³ In addition, polymers typically have high optical absorption coefficients ($\sim 10^5 \text{ cm}^{-1}$) due to the strong $\pi\text{-}\pi^*$ optical transition, which makes it possible to produce thin-film PV devices (several hundred nanometers thick).^{3,8} These light-weight and flexible devices are cost-effective for installation.^{3,8}

Ideal solar cells absorb all incident light and convert that energy into two opposite and completely-separated charges. Although light absorption can be enhanced by increasing the thickness of the active layer, the efficiency will decrease. The exciton diffusion length characterizes the distance that the exciton can travel before it undergoes recombination. The

exciton diffusion length (3-10 nm) is typically smaller than the thickness of the active layer.^{8,13} Therefore, thick active layers intending to increase light absorption can have the unintended consequence of increasing exciton recombination.^{8,14} After the charge carriers (holes and electrons) separate at the heterojunction, holes and electrons transport to opposite electrodes through the electron donor and acceptor, respectively.^{3,13} Thus, the mobility of charge carriers should be sufficiently large to transport charge carriers before recombination. This mobility (10^{-7} - 10^{-3} cm²/Vs)^{3,13,15} in conjugated polymers is several orders of magnitude lower than that in inorganic materials such as silicon ($\sim 10^3$ cm²/Vs).¹⁶ The thicker active layer, therefore, increases the possibility of the recombination between electrons and holes. In addition, because the mobility of holes is lower than that of electrons, holes are removed from the device at a slower rate than electrons, which causes a build-up of a field in the device that reduces charge separation and thus efficiency.^{13,17} This so-called “space-charge limited photocurrent” is particularly problematic in thick devices.^{13,17} Therefore, while thick active layers increase light absorption, they do not increase the efficiency. The goal of this project is to increase light absorption of thin active layer.

Investigating novel architectures to enhance light trapping is a valuable and promising approach to improve the efficiency of OPVs and is the focus of this research project. Architectures for light trapping based on surface topography such as periodic texturing,^{18,19} scattering elements,^{19,20} photonic crystal geometry²¹ and stamping^{22,23} have been studied to increase optical absorption of PV devices (**Figure A.2**). For example, Tvingstedt *et al.*²⁰ investigated enhanced light trapping by a lambertian light scatterer for the OPV device and a backscattering reflector by separating the lambertian structure from the

active layer with a PDMS optical spacer. A 3-fold enhancement of the absorption in the active layer with a photonic crystal nanostructure has been reported.²¹ Increased efficiency of OPVs by forming patterns of 1D and 2D surface relief gratings on the active layer has also been found.²² However, the major limitation of all these designs is the additional cost or complexity for fabrication of this periodic or ordered structure. Structuring V-shaped (or W-shaped) thin-film OPV devices on a length scale much larger than the thickness of the active area have been investigated to obtain increase of 50% in efficiency as well.²⁴⁻²⁶ V-shape folding of the substrate, however, occupies a large volume (as opposed to a macroscopically flat substrate) and folding the devices into the V-shape is tedious relative to the approach we propose.

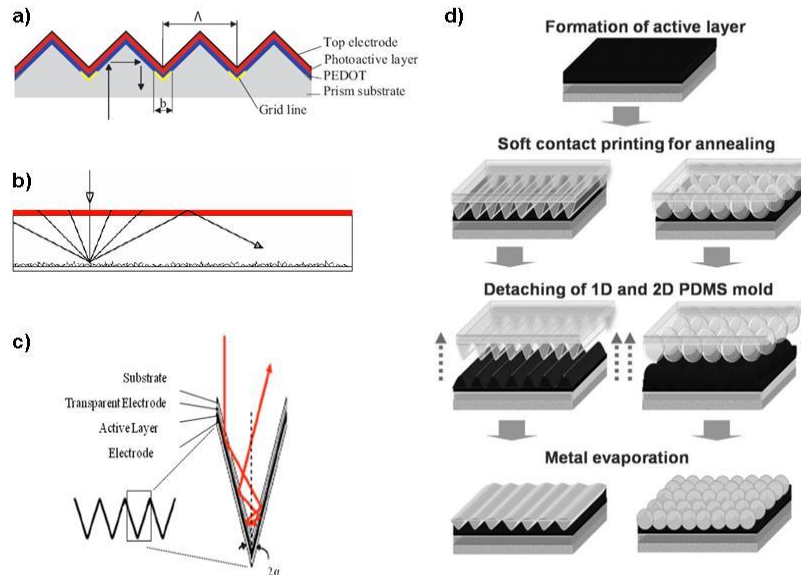


Figure A.2. Previous work on light trapping in OPVs based on a) microprism;¹⁸ b) lambertian light scatterer;²⁰ c) V-shaped/W-shaped configuration²⁴ and d) surface relief gratings pattern.²²

Here we propose to develop a simple method of forming this architecture by using topographically-buckled surfaces in response to an external trigger (heating). Our method can be distinguished by its simplicity and the fact that it is compatible with planar processing (e.g., spin coating, vapor deposition).

Fabrication of Planar Organic Photovoltaics (OPV)

We developed a process for fabricating planar OPVs on regular indium tin oxide (ITO)/glass substrates to achieve reliable efficiencies. Establishing this process is the first step toward comparing the performance of planar devices with those built on topographic structures. Most common OPV materials (P3HT and PCBM) were used for our planar device fabrication.^{27,28}

OPVs based on As-Sputtered ITO

Rather than using commercial ITO/glass as in most OPV devices, the ITO bottom electrode was deposited by radio frequency (RF) magnetron sputtering. Establishing a baseline process using deposited ITO is important since we will ultimately use unconventional substrates. We therefore cannot purchase these substrates with ITO coatings.

Commercial ITO is crystalline and has optimized optical and electrical properties.²⁹ In contrast to commercial ITO, the as-sputtered ITO is amorphous. It cannot be crystalline by annealing because the bottom electrode will be deposited on customized polymer substrates such as PS and epoxy replicas that cannot afford high-temperature annealing (300 °C)²⁹ due to thermal degradation. Therefore, the sheet resistance of amorphous ITO deposited on a

polymer substrate is usually relatively high relative to those that are annealed.²⁹⁻³¹ The properties of as-sputtered ITO were compared with commercial/annealed ITO (**Table A.1**).

Although the optical transmission (**Figure A.3**) of the as-sputtered ITO (280 nm) is slightly lower than that of commercial ITO (280 nm) (Thin Film Devices Inc.) across most wavelengths; the average transmission of as-sputtered ITO is comparable to commercial ITO between 400 nm and 650 nm, which is the absorption range for P3HT,^{28,32} and these two types of ITO have same peak transmission (**Table A.1**).

The surface of the as-sputtered ITO is smooth just like a commercial ITO. However, the sheet resistance of as-sputtered ITO is higher than of the commercial ITO, which can be attributed to the amorphous structure of the as-sputtered ITO compared to the crystalline nature of the commercial ITO.³⁰ X-ray diffraction (XRD) results also show the crystallization of commercial ITO and the amorphous ITO in as-sputtered samples (**Figure A.4**).

Table A.1. Transmission, sheet resistance and roughness of as-sputtered and commercial ITO.

ITO types	Transmission (400 - 650 nm/peak at 535 nm)	Sheet Resistance (Ω /sq)	Resistivity (Ω cm)	Roughness (RMS, nm)
As-sputtered ITO	77%/91%	30-50	$8.4-14.0 \times 10^{-4}$	0.3
Commercial ITO	83%/91%	8-10	$2.2-2.8 \times 10^{-4}$	1.5

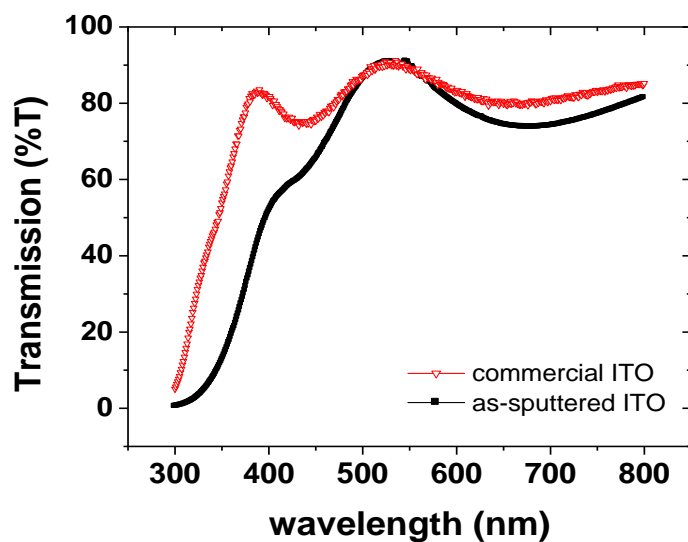


Figure A.3. Similar transmission spectra of as-sputtered ITO/glass compared with that of commercial ITO/glass in the range from 400 nm to 650 nm.

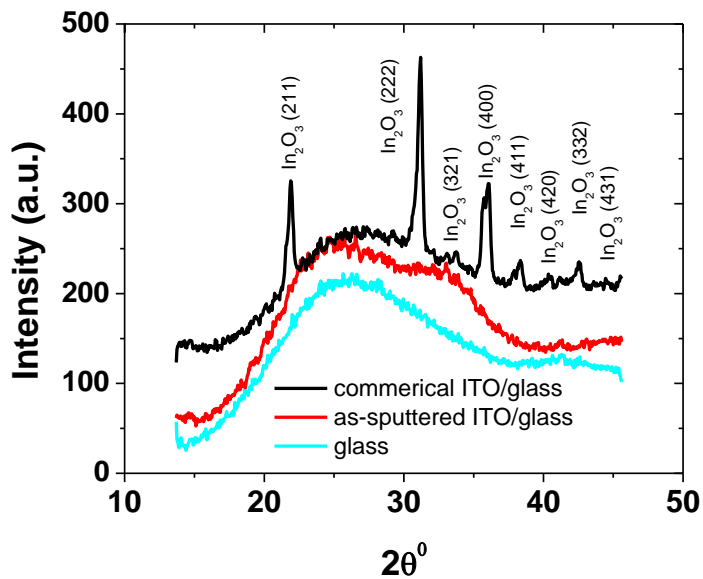


Figure A.4. Amorphous as-sputtered ITO and crystalline commercial ITO from XRD profiles.

As-sputtered ITO is of sufficient quality to fabricate devices based on its optical transmission and surface roughness (compared with the commercial ITO). The performance of the homemade device (i.e., on as-sputtered ITO) was compared with the reference device fabricated using a commercial ITO. The device layouts are shown in **Figure A.5a, b**. A representative I-V curve is plotted in **Figure A.6**. The homemade device has a higher series resistance than the reference device, as estimated from the slope of dark curves at open-circuit voltage.³³ Moreover, the fill factor for the homemade device is much lower. The resistance of ITO plays a crucial role in controlling the series resistance of the device.^{34,35} Series resistance contributes considerably to the fill factor of the solar cells and, hence, their overall efficiency.^{33,36} The fairly large active area (0.20 cm^2) used for the device is not desirable for low-conductive ITO substrate since the resistance of the ITO dominates the series resistance of a large area device with low-conductivity ITO.^{34,35} A small active area (0.01 cm^2) is desired for our homemade ITO, which has higher resistance than that of commercial ITO.³⁵

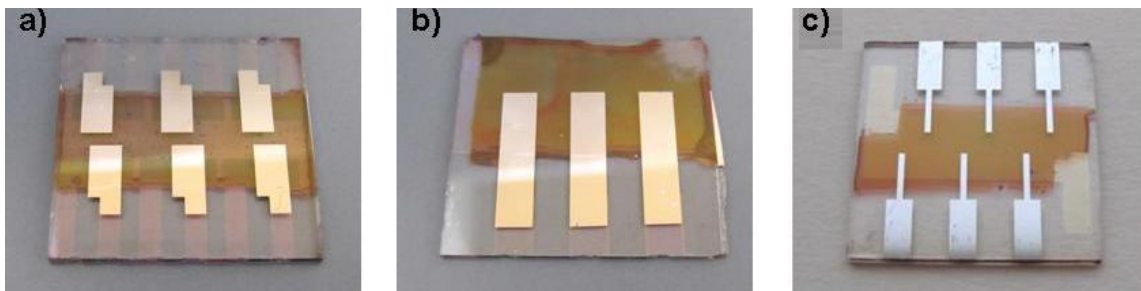


Figure A.5. Photographs of reference device layouts on a) commercial ITO; b) homemade device on as-sputtered ITO with large active area and c) homemade device on as-sputtered ITO with small active area. The substrates are $1 \times 1 \text{ inch}^2$.

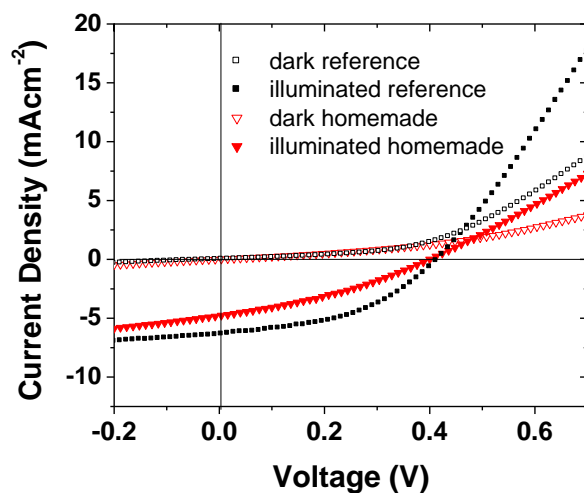


Figure A.6. Current density-voltage curves for the reference device and the homemade device. Reference device: $V_{oc}=0.42$ V; $J_{sc}=6.36$ mA/cm²; PCE=1.18%; FF=0.45. Homemade device: $V_{oc}=0.40$ V; $J_{sc}=4.80$ mA/cm²; PCE=0.65%; FF=0.34.

Effect of Small Active Area and Post-Annealing on Device Performance

The homemade device with a small active area was fabricated on as-sputtered ITO/glass substrate, and the device layout is shown in **Figure A5c**. The active area (1.5-2 mm²) of each device was measured under an optical microscope. The fill factor of device with a small active area (**Table A.2**) increased significantly compared with that of device with a large active area, which is consistent with literature report.^{33,34}

The device with a small active area still showed an efficiency <1%, which is significantly lower than the literature values (**Table A.2**). In addition, the efficiency on the same substrate varied from device to device.

Post-annealing is a critical step for improving the device efficiency. The bicontinuous inter-penetrating network of P3HT:PCBM is very sensitive to thermal annealing. Post-

annealing after top electrode deposition improves current density and the fill factor due to changes in the P3HT:PCBM interface with the top electrode.^{27,37} Kim *et al.*³⁸ reported that the efficiency of the device with post-annealing at 150 °C increases to 3.0%, compared with the efficiency (1.6%) of the device with pre-annealing at 150 °C, and the efficiency (0.5%) without any annealing. The researchers found that Al inter-diffusion increases during post-annealing and that the presence of Al during the annealing impedes the growth of P3HT crystals near the surface.³⁸

Therefore, all planar devices were post-annealed after Al electrode deposition. Homemade device with a small active area and post-annealing has almost twice the current density and efficiency of homemade device without post-annealing, as shown in **Table A.2** and in I-V curves in **Figure A.7**.

Table A.2. Short-circuit current densities (J_{sc}), fill factors (FF), open circuit voltages (V_{oc}) and efficiencies of OPV based on P3HT:PCBM blends with and without post-annealing and with different active areas.

Active area	Post-annealing	J_{sc} (mA/cm ²)	FF	V_{oc} (V)	PCE (%)
Large	N	3.54±1.30	0.26±0.02	0.47±0.11	0.46±0.21
Small	N	2.38±0.94	0.45±0.12	0.54±0.09	0.54±0.18
Small	Y	4.78±0.75	0.46±0.10	0.57±0.05	1.28±0.47

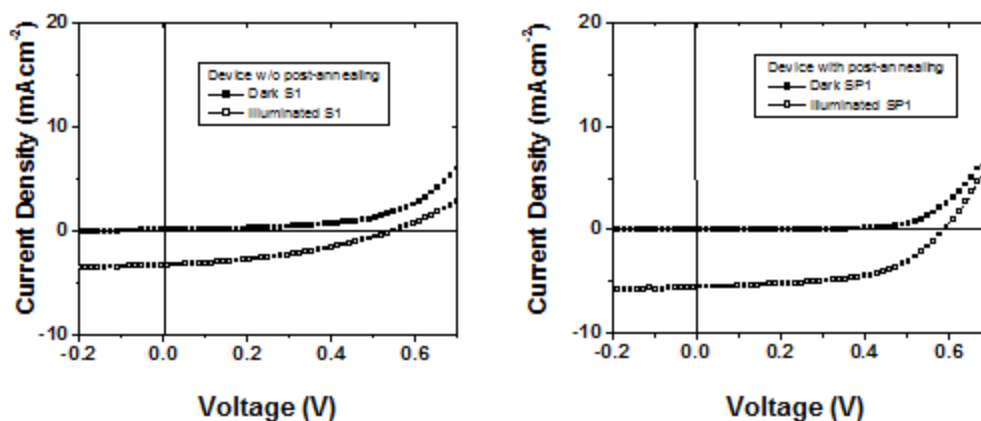


Figure A.7. Current density-voltage curves for device without post-annealing (left) and with post-annealing (right).

Device Cast from Varying Concentrations and Different Solvents

The device efficiency has been increased significantly by post-annealing. However, as shown in **Figure A.8**, the non-uniform film quality with many defects in the P3HT:PCBM film leads to inconsistent device efficiency. For example, the efficiency standard deviation for device with the small active area and post-annealing is about 37% of the average (**Table A.2**).

High concentration of mixed solution and high spin speed lead to films with much better uniformity (**Figure A.8**). Therefore, we studied devices based on different concentrations of P3HT:PCBM solutions and with approximately the same thickness of P3HT:PCBM at different spin speeds (**Table A.3**).

As for devices with a high concentration solution (20 mg/ml P3HT), the device with shorter spin-coating time shows a much higher efficiency due to a shorter spin time, hence, a slower solvent annealing.³⁹⁻⁴¹ The fact that the efficiencies of devices with a high

concentration solution were still lower than the device with a low concentration solution implies the necessary optimization of spin coating conditions for high concentration blend.

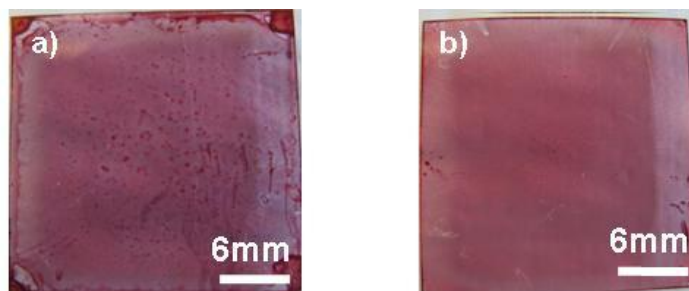


Figure A.8. Photographs of P3HT:PCBM films cast from different concentrations: a) 10:8 mg/ml P3HT:PCBM solution, spin speed is 600 rpm for 60 sec and b) 20:16 mg/ml P3HT:PCBM solution spin speed is 2000 rpm for 60 sec.

Table A.3. Short-circuit current densities (J_{sc}), fill factors (FF), open circuit voltages (V_{oc}) and efficiencies of OPV based on solutions with different concentrations.

P3HT:PCBM concentration (mg/ml)	Spin condition (rpm/sec)	J_{sc} (mA/cm ²)	FF	V_{oc} (V)	PCE (%)
10:8	600/60	7.77 ± 0.54	0.47 ± 0.02	0.61 ± 0.00	2.25 ± 0.24
20:16	2000/60	5.17 ± 0.76	0.36 ± 0.06	0.49 ± 0.01	0.92 ± 0.25
20:16	2000/20	6.64 ± 0.87	0.44 ± 0.05	0.59 ± 0.01	1.75 ± 0.34

All devices discussed above were fabricated by using 1,2-dichlorobenzene (ODCB) as the solvent for P3HT:PCBM. However, chlorobenzene (CB) is an even more popular solvent used in OPV fabrication.^{27,32,42} There is no confident conclusion that CB works better than ODCB, and based on literature work, the device performances from these two solvents are comparable.^{27,28} We found the film cast from CB to produce the P3HT:PCBM films

comparable to the films cast from high concentration in ODCB that has less defects, resulting in an efficiency that is more consistent than devices from ODCB. Current density was $7.28 \pm 0.31 \text{ mA/cm}^2$, the open-circuit voltage was $0.59 \pm 0.01 \text{ V}$, fill factor was 0.45 ± 0.02 and the efficiency was $1.93 \pm 0.11\%$. Devices with efficiencies of $\approx 2\%$ can be obtained when cast from CB with efficiency standard deviation of the average around 5%.

Effect of the Device Layout on Measurement Accuracy

Efforts focused on improving consistency of the efficiency by optimizing the fabrication conditions but also to study the device layout to assure accurate measurement.

Devices with two types of layouts were tested to examine the different current densities (**Figure A.9**). The device with crossed layout had P3HT:PCBM and PEDOT:PSS films spin-coated across the entire surface, while the device with central layout had polymer films only on the overlapping area between ITO and Al electrodes. The I-V measurement was operated in two modes: 1) the light passed through a mask that leaves only one cell exposed to the light at a time and 2) the light passed across the entire surface so all six devices were exposed to the light at the same time. The set-up is shown in **Figure A.10**.

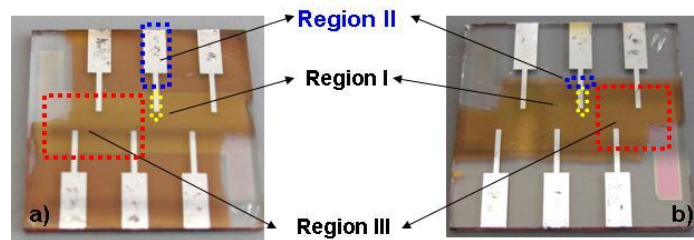


Figure A.9. Photographs of different device layouts: a) crossed layout and b) central layout.

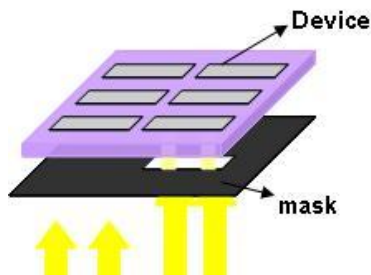


Figure A.10. Schematic of the set up for I-V measurement through a mask.

The device performance is summarized in **Table A.4**. The device with central layout shows similar current densities in both measurement modes. However, the device with crossed layout shows extra current when measurement is done without the mask. As shown in **Figure A.9**, the presence of this extra current can be explained by the pseudo active area (region II) among the unscratched PEDOT:PSS (conductive polymer performing as anode electrode), P3HT:PCBM film and Al electrode pad.⁴³ Region I is nominal active area. Region III of ITO/PEDOT:PSS/P3HT:PCBM overlap is where the extra current can be ignored due to the missing electrode.⁴³ Therefore, to fabricate the device, the PEDOT:PSS and P3HT:PCBM films should be removed under Al electrode pad as central layout rather than crossed layout to avoid extra current from region II.

Table A.4. Short-circuit current densities, open-circuit voltages, fill factors and efficiencies for devices with different device layouts.

Layout	Measure method	J_{sc} (mA/cm ²)	V_{oc} (V)	FF	PCE (%)
Crossed	Mask	6.34±2.07	0.40±0.02	0.28±0.01	0.71±0.25
Crossed	-	10.15±3.03	0.42±0.02	0.26±0.00	1.11±0.35
Central	Mask	5.38±0.60	0.47±0.02	0.32±0.03	0.80±0.14
Central	-	5.51±0.97	0.48±0.01	0.30±0.03	0.78±0.12

OPV Based on Buckles Topography

The commonly applied transparent electrode such as ITO and top electrode such as Al have been studied to demonstrate the compatibility of forming buckles on top of the PS layer. Moreover, planar OPVs following conventional and popular methods were fabricated to obtain reliable efficiencies. Devices with different active areas, annealing methods and solution preparations were made to study the important factors that influence device efficiency. Planar OPVs with small active area and post-annealing show reliable $\approx 2\%$ efficiency.

Under the cooperated work with Material Science at NC State and RTI, we used the same method to fabricate OPV on buckled PS structures. OPVs (ITO/CuPc/C₆₀/BCP/Al/Ag) on buckled PS/glass substrate were fabricated by Ethan Klem and Jay Lewis (RTI). Buckles were formed after annealing of ITO (200 nm)/PS (1.5 μm)/glass layer at the temperature of 120 °C. The total area of this device is 2" x 2". **Figure A.11a** shows a profilometry scan of a representative substrate: isotropic buckles with a characteristic wavelength ($\sim 14 \mu\text{m}$). CuPC (20 nm)/C₆₀ (40 nm)/BCP (12 nm) layers were thermally evaporated on the buckled surface. The increased light absorption based on buckled surface was tested by comparing the reflectance of buckled absorbing layer with that of the planar layer (**Figure A.11b**). The light absorption is enhanced $\sim 10\%$ between 500 nm and 550 nm, while is enhanced 2~3% between 600 nm and 700 nm. The absorbance peaks characteristic of CuPc and C60 are evident at the expected wavelengths of ~ 450 , 625, and 700 nm.⁴⁴ The built best device on buckled surface shows $\sim 20\%$ increase in efficiency and $\sim 50\%$ increase in current density, as shown in **Figure A.12**.

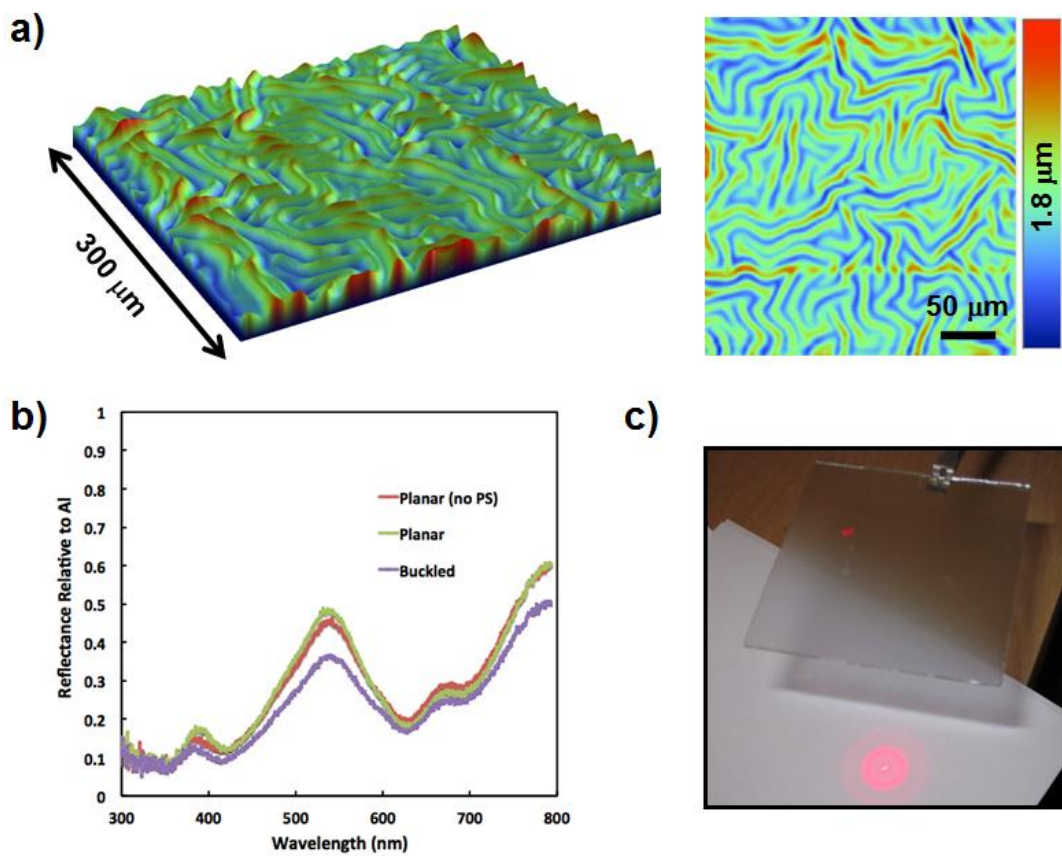


Figure A.11. (a) Profilometer scan images (3D and 2D) show the representative buckled surface of ITO/PS films; (b) Reflectances relative to Al reference for planar and buckled CuPc/C60 absorbing layer; and (c) Photograph of light scattering through buckled ITO/PS substrate from a red laser point.⁴⁵

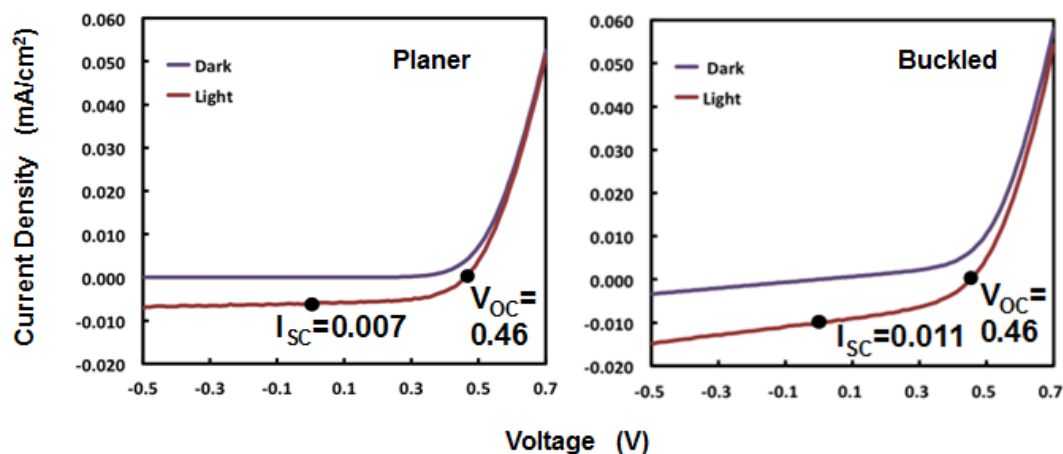


Figure A.12. Current density-voltage curves for planar and buckled devices. Planer device: $V_{oc}=0.46$ V; $J_{sc}=7$ $\mu\text{A}/\text{cm}^2$; PCE=1.89%; FF=0.569. Buckled device: $V_{oc}=0.46$ V; $J_{sc}=11$ $\mu\text{A}/\text{cm}^2$; PCE=2.2%; FF=0.425. (Credit: Ethan Klem and Jay Lewis)

References

1. N.S. Lewis, *Toward cost-effective solar energy use*. Science, 2007. **315**: p. 798-801.
2. M. Gratzel, *Photoelectrochemical cells*. Nature, 2001. **414**: p. 338-344.
3. S.E. Shaheen, D.E. Ginley, and G.E. Jabbour, *Organic-based photovoltaics: toward low-cost power generation*. MRS Bulletin, 2005. **30**: p. 10-19.
4. E. Bundgaard and F.C. Krebs, *Low band gap polymers for organic photovoltaics*. Solar Energy Materials & Solar Cells, 2007. **91**: p. 954-985.
5. A. Shah, P. Torres, R. Tscharnner, N. Wyrsh, and H. Keppner, *Photovoltaic technology: the case for thin-film solar cells*. Science, 1999. **285**: p. 692-698.
6. B.A. Gregg, *The photoconversion mechanism of excitonic solar cells*. MRS Bulletin, 2005. **30**: p. 20-22.
7. *Heterojunction organic solar cell operation*. [cited 2010 Sep 08]; Available from: <http://www2.warwick.ac.uk/fac/sci/chemistry/research/physicalchemistry/jones/jonesgroup/research/organicsemiconductors/organicpv/>.
8. A.C. Mayer, S.R. Scully, B.E. Hardin, M.W. Rowell, and M.D. McGehee, *Polymer-based solar cells*. Materials Today, 2007. **10**: p. 28-33.
9. D.J. Milliron, I. Gur, and A.P. Alivisatos, *Hybrid organic-nanocrystal solar cells*. MRS Bulletin, 2005. **30**: p. 41-44.
10. C.J. Brabes, J.A. Hauch, P. Schilinsky, and C. Waldauf, *Production aspects of organic photovoltaics and their impact on the commercialization of devices*. MRS Bulletin, 2005. **30**: p. 50-52.
11. F.C. Krebs, *Fabrication and processing of polymer solar cells: a review of printing and coating techniques*. Solar Energy Materials & Solar Cells, 2009. **93**: p. 394-412.

12. H.J. Park, M.G. Kang, H. Ahn, and L.J. Guo, *A facile route to polymersolar cells with optimum morphology readily applicable to a roll-to-roll process without sacrificing high device performances*. Adv. Mater., 2010. **22**:p.E247-E253.
13. P.W.M. Blom, V.D. Mihailetschi, L.J.A. Koster, and D.E. Markov, *Device physics of polymers: fullerene bulk heterojunction solar cells*. Adv. Mater., 2007. **19**: p. 1551-1566.
14. S.R. Forrest, *The limits to organic photovoltaic cell efficiency*. MRS Bulletin, 2005. **3**:- p. 28-32.
15. J. Nelson, *Organic photovoltaic films*. Current Opinion in Solid State and Materials Science, 2002. **6**: p. 87-95.
16. M. Grundmann, *The physics of semiconductors: an introduction including devices and nanophysics*. 2006, Verlag Berlin Heidelberg: Springer.
17. M. Lenes, L.J.A. Koster, V.D. Mihailetschi, and P.W.M. Blom, *Thickness dependence of the efficiency of polymer:fullerene bulk heterojunction solar cells*. Appl. Phys. Lett., 2006. **88**: p. 243502.
18. M. Niggemann, M. Riede, A. Gombert, and K. Leo, *Light trapping in organic solar cells*. Phys. Stat. Sol., 2008. **205**: p. 2862-2874.
19. C. Cocoyer, L. Rocha, L. Sicot, B. Geffroy, R.d. Bettignies, C. Sentein, C. Fiorini-Debuisschert, and P. Raimond, *Implementation of submicrometric periodic surface structures toward improvement of organic-solar-cell performances*. Appl. Phys. Lett., 2006. **88**: p. 133108.
20. K. Tvingstedt, M. Tormen, L. Businaro, and O. Inganas, *Light confinement in thin film organic photovoltaic cells*. Photonics for Solar Energy Systems, 2006. **6197**: p. 61970C.
21. D.H. Ko, J.R. Tumbleston, L. Zhang, S. Williams, J.M. DeSimone, R. Lopez, and E.T. Samulski, *Photonic crystal geometry for organic solar cells*. Nano Lett., 2009. **9**: p. 2742-2746.

22. S.I. Na, S.S. Kim, J. Jo, S.H. Oh, J. Kim, and D.Y. Kim, *Efficient polymer solar cells with surface relief gratings fabricated by simple soft lithography*. Adv. Funct. Mater., 2008. **18**: p. 3956-3963.
23. L.S. Roman, O. Inganäs, T. Granlund, T. Nyberg, M. Svensson, M.R. Andersson, and J.C. Hummelen, *Trapping light in polymer photodiodes with soft embossed gratings*. Adv. Mater., 2000. **12**: p. 189-195.
24. S. Rim, S. Zhao, S.R. Scully, M.D. McGehee, and P. Peumans, *An effective light trapping configuration for thin-film solar cells*. Appl. Phys. Lett., 2007. **91**(243501).
25. Y. Zhou, F. Zhang, K. Tvingstedt, and W. Tian, *Multifolded polymer solar cells on flexible substrates*. Appl. Phys. Lett., 2008. **93**: p. 033302.
26. K. Tvingstedt, V. Andersson, F. Zhang, and O. Inganäs, *Folded reflective tandem polymer solar cell doubles efficiency*. Appl. Phys. Lett., 2007. **91**: p. 123514.
27. W. Ma, C. Yang, X. Gong, K. Lee, and A.J. Heeger, *Thermally stable, efficient polymer solar cells with nanoscale control of the interpenetrating network morphology*. Adv. Funct. Mater., 2005. **15**: p. 1617-1622.
28. G. Li, V. Shrotriya, J. Huang, Y. Yao, T. Moriarty, K. Emery, and Y. Yang, *High-efficiency solution processable polymer photovoltaic cells by self-organization of polymer blends*. Nature Materials, 2005. **4**: p. 864-868.
29. Y.Z. You, Y.S. Kim, D.H. Choi, H.S.J.J.H. Lee, and D. Kim, *Electrical and optical study of ITO films on glass and polymer substrates prepared by DC magnetron sputtering type negative metal ion beam deposition*. Materials Chemistry and Physics, 2008. **107**: p. 444-448.
30. D.C. Paine, T. Whitson, D. Janiac, R. Beresford, and C.O. Yang, *A study of low temperature crystallization of amorphous thin film indium-tin-oxide*. J. Appl. Phys., 1999. **85**: p. 8445-8450.
31. M. Fahland, T. Vogt, W. Schoenberger, and N. Schiller, *Optical properties of metal based transparent electrodes on polymer films*. Thin Solid Films, 2008. **516**: p. 5777-5780.

32. R. Radbeh, E. Parbaile, J. Boucle, C.D. Bin, A. Moliton, V. Coudert, F. Rossignol, and B. Ratier, *Nanoscale control of the network morphology of high efficiency polymer fullerene solar cells by the use of high material concentration in the liquid phase*. *Nanotechnology*, 2010. **21**: p. 035201.
33. J.D. Servaites, S. Yeganeh, T.J. Marks, and M.A. Ratner, *Efficiency enhancement in organic photovoltaic cells: consequences of optimizing series resistance*. *Adv. Funct. Mater.*, 2010. **20**: p. 97-104.
34. J.W. Kang, S.P. Lee, D.G. Kim, S. Lee, G.H. Lee, J.K. Kim, S.Y. Park, J.H. Kim, H.K. Kim, and Y.S. Jeong, *Reduction of series resistance in organic photovoltaic using low sheet resistance of ITO electrode*. *Electrochemical and Solid-State Letters*, 2009. **12**: p. H64-H66.
35. P. Peumans, A. Yakimov, and S.R. Forrest, *Small molecular weight organic thin-film photodetectors and solar cells*. *J. Appl. Phys.*, 2003. **93**: p. 3693-3723.
36. H. Hoppe and N.S. Sariciftci, *Organic solar cells: an overview*. *J. Mater. Res.*, 2004. **19**: p. 1924-1945.
37. F. Padiner, R.S. Rittberger, and N.S. Sariciftci, *Effects of postproduction treatment on plastic solar cells*. *Adv. Funct. Mater.*, 2003. **13**: p. 1-4.
38. H.J. Kim, J.H. Park, H.W. Lee, D.R. Lee, and J.J. Kim, *The effect of Al electrodes on the nanostructure of poly(3-hexylthiophene): fullerene solar cell blends during thermal annealing*. *Organic Electronics*, 2009. **10**: p. 1505-1510.
39. G. Li, Y. Yao, H. Yang, V. Shrotriya, G. Yang, and Y. Yang, *“Solvent annealing” effect in polymer solar cells based on poly(3-hexylthiophene) and methanofullerenes*. *Adv. Funct. Mater.*, 2007. **17**: p. 1636-1644.
40. J.H. Park, J.S. Kim, J.H. Lee, W.H. Lee, and K. Cho, *Effect of annealing solvent solubility on the performance of poly(3-hexylthiophene)/methanofullerene solar cells*. *J. Phys. Chem. C*, 2009. **113**: p. 17579-17584.
41. B.C. Thompson and J.M. Frechet, *Polymer-fullerene composite solar cells*. *Angew. Chem. Int. Ed.*, 2008. **47**: p. 58-77.

42. M. Campoy-Quiles, T. Ferenczi, and T. Agostinelli, *Morphology evolution via self-organization and lateral and vertical diffusion in polymer: fullerene solar cell blends*. Nature Materials, 2008. **7**: p. 158-164.
43. A. Cravino, P. Schilinsky, and C.J. Brabec, *Characterization of organic solar cells: the importance of device layout*. Adv. Funct. Mater., 2007. **17**: p. 3906-3910.
44. T. Luong, T. T., Chen, Z. & Zhu, H. Flexible solar cells based on copper phthalocyanine and buckminsterfullerene. *Sol. Energy Mater. Sol. Cells* **94**, 1059–1063 (2010).
45. Casper, M. D. *The Origins of Buckle Formation in Vapor Deposited Oxides on Polymers.*, PhD dissertation (North Carolina State University,, 2011).

Appendix B

Additional Experiment Details

PDMS curing - Mixing components from a commercial two-component kit (Sylgard[®]-184) produced PDMS networks. The elastomeric base and curing agents (10:1 mass ratio) were mixed thoroughly for about 60 seconds. The mixture was degassed in a desiccator under mild vacuum until all bubbles in the mixture were completely removed. The degassed PDMS casting solution was poured into a Petri-dish and cured in an oven (60 °C) overnight. The thickness of the PDMS sheet depends on the amount of casting solution and the volume of the Petri-dish. After curing, sections of PDMS were produced by cutting the PDMS sheet with a razor blade.

ITO sputtering on pre-stretched PDMS - an ITO film was deposited onto pre-stretched PDMS sheet (1 mm, $\varepsilon \approx 10\%$) by direct current (DC) sputtering. The 2x1/4" ITO target used was 90% In₂O₃ with 10% SnO₂ (99.99% purity, Kurt J. Lesker Company). The applied DC power was 10 W during sputtering. The distance between the sample and the target was 9.8 cm. The process pressure was 4 mTorr. At these conditions, sputtering for 10 min yielded a 40 nm thick ITO film. After ITO deposition, the strain was slowly released by manually rotating the shaft of the stretcher.

ITO/PS bilayer preparation - Polystyrene (Aldrich) used in this study has a number-average molecular weight (M_n) and weight-average molecular weight (M_w) of 140 kDa and 230 kDa, respectively, and T_g of 94 °C. PS films were spin-coated on pre-cleaned and UVO treated Si wafers at 500 rpm for 30 seconds from PS solution in toluene. ITO was then deposited onto the dried PS film on Si. The ITO sputtering conditions were the same as

described above, except the process pressure was 10 mTorr. Sputtering for 10 min yielded a 40 nm ITO film. The sample was then annealed at 120 °C for 30 min in a vacuum oven.

As-sputtered ITO for planar devices - The ITO bottom electrode was deposited on 1x1 inch² boro-aluminosilicate glass (Delta's technology Limited) by radio frequency (RF) magnetron sputtering. The sputter system included a sputter chamber and a load lock chamber. The power was 30 W constantly during sputtering. The distance between the sample and the target was 8 cm. The base pressure of sputtering was 1.6×10^{-6} Torr and process pressure was 4 mTorr. Sputtering for 40min gave a 280 nm thick ITO film.

OPVs fabrication - As-sputtered ITO/glass substrates were cleaned by soaking in acetone and isopropanol (IPA) respectively for 10 min during sonication, followed by UVO treatment (10 min) immediately before spin-coating of poly(3,4-ethylenedioxythiophene)-poly(styrenesulfonate) PEDOT:PSS (high conductive grade, Sigma-Aldrich). PEDOT:PSS was diluted by deionized water at a mass ratio of 1:1.3, followed by filtering using 0.45 µm filters to remove large aggregates and impurities. PEDOT:PSS was spin-coated at 4000 rpm for 40 seconds on pre-cleaned ITO/glass substrates and was then annealed at 60 °C in a vacuum oven for 1 hour to remove the water content.

The P3HT:PCBM ratio for the mixed solution was 1:0.8 with a concentration of 10 mg/ml P3HT solution in 1,2-dichlorobenzene (ODCB). The mixed solution was stirred overnight. The solution was spin-coated onto PEDOT:PSS/ITO substrates at 600 rpm for 60 seconds. The P3HT:PCBM film thicknesses were around 100 nm. The mixing procedure described above was performed in a nitrogen-filled glove box. The devices were dried slowly for 20 min in a glass Petri-dish and were then pre-annealed on hotplate at 110 °C for 10 min.

The samples were then ready for Al deposition. Al electrodes were deposited by thermal evaporation at about 9×10^{-7} Torr base pressure. Al electrode thickness was about 40 nm after a 20 min deposition. Devices were post-annealed after Al electrode deposition at 150 °C for 15 min on the hotplate in the glove box.

The completed device was taken out of the glove box for current-voltage measurements. After calibration with a silicon reference cell, the current was measured under voltage sweeping with a Keithley 2400 source meter.

The devices cast from CB were also prepared. The P3HT:PCBM ratio for the mixed solution was 1:1 with a concentration of 10mg/ml P3HT solution in CB. The mixed solution was stirred at 60 °C overnight. The solution was coated on the PEDOT:PSS/ITO substrate at 1000 rpm for 60 seconds. The P3HT:PCBM film thicknesses were \approx 100 nm. All other operations were the same as in the fabrication of the device based on DOCB.

As for the study of measurement accuracy on different layouts, the devices were cast from CB and treated only by post-annealing (no pre-annealing).

As for the devices on flat epoxy, epoxy replica and glass, 120 °C for 20min was used instead of 150 °C for 15 min for post-annealing.